Real-time Reduced Order Modeling of High-dimensional Partial Differential Equations via Time Dependent Subspaces

by

Prerna Patil

Sc.M Fluids and Thermal Sciences, Brown University, 2017

B.Tech, Aerospace Engineering, IIT Madras, 2014

Submitted to the Graduate Faculty of

the Swandon School of Engineering in partial fulfillment

of the requirements for the degree of

Doctor of Philosophy

University of Pittsburgh

2022

UNIVERSITY OF PITTSBURGH

SWANSON SCHOOL OF ENGINEERING

This dissertation was presented

by

Prerna Patil

It was defended on

June 6, 2022

and approved by

Dr. Peyman Givi, PhD, Distinguished Professor, James T. MacLeod Professor Mechanical Engineering and Petroleum Engineering

Dr. William Layton, PhD, Professor, Department of Mathematics

Dr. Inanc Senocak, Associate Professor, Department of Mechanical Engineering and Materials Science

Dissertation Director: Dr. Hessam Babaee, Assistant Professor, Department of Mechanical Engineering and Materials Sciences

Real-time Reduced Order Modeling of High-dimensional Partial Differential Equations via Time Dependent Subspaces

Prerna Patil, PhD

University of Pittsburgh, 2022

We present a new methodology for the real-time reduced-order modeling of stochastic partial differential equations (SPDEs) called the *Dynamically/Bi-Orthonormal (DBO)* decomposition. In this method, the stochastic fields are approximated by a low-rank decomposition to spatial and stochastic subspaces. Each of these subspaces is represented by a set of orthonormal time-dependent modes. We derive exact evolution equations of these time-dependent modes and the evolution of the factorization of the reduced covariance matrix. We show that DBO is equivalent to the *Dynamically Orthogonal (DO)* [1] and *Bi-Orthogonal (BO)*[2] decompositions via linear and invertible transformation matrices that connect DBO to DO and BO. We study the convergence properties of the method and compare it to the DO and BO methods. Overall we observe improvements in the numerical accuracy of DBO compared against DO and BO.

In the second part of this work we direct our attention towards solving SPDEs with non-homogenous stochastic boundary conditions. A crucial question in this application is how do we determine the distribution of random boundary conditions among spatial bases. The DBO methodology is applied for determining the boundary conditions for time-dependent bases at no additional computational cost beyond that of solving similar SPDEs with homogeneous boundary conditions. The boundary conditions are determined by forming a variational principle whose minimization leads to the evolution of time-dependent bases at the boundary as well as the interior points. The formulation is applied for stochastic Dirichlet, Neumann and Robin boundary conditions and the performance of the method is assessed.

In the third part of this work, the focus is shifted towards application of this methodology and development of techniques to solve deterministic partial differentiation equations. A multi-dimensional variable is represented by a set of one-dimensional time-dependent or-

thonormal modes in each dimension and a core tensor. We derive evolution equations for these modes and the core tensor. Due to low rank representation of the solution at every time instant, the method also provides advantages in data storage for a large number of time steps. This advantage is notably evident in higher dimensions ($d > 2$).

Table of Contents

List of Tables

List of Figures

Acknowledgements

I would like to start by thanking my advisor Dr. Hessam Babaee for the wonderful learning experience that is my PhD. His guidance, support and the numerous discussions I had with him about reduced order models and fluid mechanics over the course of my PhD have helped me become a better researcher. His enthusiasm about these topics is infectious and I have always left his meetings with innumerable avenues to explore scientifically. I am grateful to Dr. Peyman Givi, who is not only an integral part of my committee but has also been an incredible mentor during my graduate research. I would like to thank my committee members: Dr. Inanc Senocak and Dr. William Layton for their helpful feedback about my thesis work as well as their advise about figuring out the next steps of my academic career.

I wish to thank my labmates who have provided me with stimulating discussions which has helped with my research projects. Thanks to Michael Donello, Shaghayegh Ashtiani, Alireza Amiri, Donya Ramezanian and Grishma Palkar for creating a wonderful working atmosphere in the lab. I remember the lunch time discussions and hikes that we undertook during the pre-pandemic era which were a huge respite to get through stressful semesters. I would like to specially thank Hossein Naderi for helping me out with the conversion of my codes to Python and making them ten times faster than my original codes. Due to this I was able to test a few too many cases and perform numerical experiments which I was able to include in the last part of my work, not to mention the fact that it has helped me graduate in time!

I wish to thank Emily Pinto and her family who helped me get acquainted with the way of life in Pittsburgh. I would also like to thank my friends at Moore aviation who have literally helped me fly. Special thanks to Robert Marshall for all the discussions about aviation, aircrafts and the pure joy of flying. The last five years of graduate school would not have been possible without my wonderful friends who I met a decade ago and have stayed an integral part of my life: Harsha, Sindhu, Jinita, Richa, Arjun, Vegnesh, Karthik, Chandru, Dhinesh, Harika. Thanks for helping me keep my sanity intact! Thanks to my brother and sister-in-law: Prasanna and Swamipa for always being a phone call away and chats about

anything and everything. Thanks to my cousin sister Tejali, aunt Bhavana and chirpy little Krisha who have kept my spirits up throughout these years especially during the lockdowns. Lastly, I would like to thank my parents without whose support and encouragement this thesis would not have been possible. To them I dedicate this thesis.

1.0 Introduction

The pressing need of conducting verification and validation (V&V) for realistic simulations in scientific and engineering applications requires propagating uncertainty in these systems. These systems are often subject to uncertainty that may come from imperfectly known parameters — that can be modeled as random parameters — or random initial/boundary conditions, or by systems that are characterized by inherent stochastic dynamics, such as coarse grain models of multi-scale systems, in which the effects of unresolved scales are modeled as stochastic processes [4]. Uncertainty quantification (UQ) in such systems can disentangle the effects of different uncertain sources on the quantities of interest and it can guide the decision making process and ultimately lead to more reliable predictions and designs.

One of the fundamental challenges in performing UQ in complex engineering and scientific systems is the computational cost associated with this task. These systems are often characterized by high-dimensional ordinary/partial differential equations, whose forward simulation can be computationally costly. There are a large number of techniques for performing UQ. These methods are primarily either sample based such as Monte Carlo (MC) method and its variants such as multi-level MC and quasi-MC (QMC) [5, 6, 7], or are based on polynomial chaos expansion (PCE) [8, 9, 10, 11, 12, 13, 14, 15, 16, 17, 18].

While PCE performs well for nearly elliptic problems or flow at low Reynolds numbers, solving highly transient stochastic ordinary/partial differential equations (SODE/SPDE) is particularly challenging for this method. It was shown in [19] that for the one dimensional advection equation with a uniform random transport velocity the order of polynomial chaos must increase with time to maintain the error below a given value. PCE also loses its efficiency for nonlinear systems with intermittency and positive Lyapunov exponents [20].

Reduced order modeling approaches are popular tools for state prediction and control of deterministic evolutionary dynamical systems [21, 22, 23, 24, 25, 26, 27, 28]. With the recent developments in data-fusion and specifically multi-fidelity modeling approaches [29, 30, 31], in which imperfect predictions can be effectively utilized when combined with high-fidelity

data, reduced order modeling techniques will play a crucial role as a surrogate model that generates low-fidelity data at a low computational cost. In the context of SPDEs, the dynamically orthogonal decomposition (DO) was introduced [1] as a stochastic reduced order modeling technique, in which the stochastic field $u(x,t;\omega)$ is approximated as:

$$u(x,t;\omega) = \bar{u}(x,t) + \sum_{i=1}^{r} u_i(x,t) y_i(t;\omega),$$

where $\bar{u}(x,t)$ is the mean, $u_i(x,t)$ are a set of deterministic time-dependent orthonormal modes in the spatial domain and $y_i(t;\omega)$ are zero-mean random processes in the stochastic domain and r is the reduction order. To remove the redundancy in time, the evolution of the spatial subspace, i.e. $\partial u_i(x,t)/\partial t$, is chosen to be orthogonal to $u_j(x,t)$. By enforcing the above constraints, one can derive closed-form evolution equations for $\bar{u}(x,t)$, $u_i(x,t)$ and $y_i(t;\omega)$. The imposed conditions on the above decomposition are not unique. Bi-orthogonal (BO) decomposition is one such variant, in which the spatial basis are orthogonal and the stochastic basis are orthonormal [32]. Recently, a non-intrusive DO formulation was introduced [33] and it was shown that the DO evolution equations are the optimality conditions of a variational principle that seeks to minimize the distance between the rate of change of full-dimensional dynamics and that of the DO reduction. For linear parabolic SPDEs, the difference between the approximation error of r-term DO decomposition and r-term Karhunen-Loéve (KL) decomposition can be bounded [34]. Independently and prior to the development of DO/BO, the idea of using time-dependent basis had been introduced in very different fields, namely chemistry and quantum mechanics for the approximation of the deterministic Schrödinger equations by the Multi Configuration Time Dependent Hartree (MCTDH) method [35, 36], and in deterministic settings [37].

It was shown in [3] that both DO and BO are equivalent: in both of these methods $u_i(x,t)$ and $y_i(t;\omega)$ span the same subspace and a linear invertible time-dependent matrix transforms one to the other. This matrix transformation amounts to an *in-subspace* rotation and stretching for $u_i(x,t)$ modes and $y_i(t;\omega)$ coefficients. In contrast to PCE, BO/DO decompositions allow the stochastic coefficients evolve with time as opposed to time-invariant polynomial chaos basis. This relaxation allows BO/DO decompositions to "follow" the transient dynamics. It was shown that in the limit of zero variance of $y_i(t;\omega)$, the subspace

of $u_i(x,t)$ converges exponentially fast to the most unstable subspace of the dynamical system — associated with the r most dominant eigendirections of the Cauchy–Green tensor [38]. It was shown that the reduction based on the time-dependent basis and coefficients can capture the low-dimensional structure of the intermittent dynamics [39].

Although both DO and BO are mathematically equivalent, they exhibit different numerical performance. When the eigenvalues of the reduced covariance matrix are close or cross each other, the BO formulation becomes numerically unstable. On the other hand, the DO decomposition does not have the issue of eigenvalue crossing. However, when the eigenvalues of the reduced covariance matrix are not close, BO exhibits better numerical performance than DO [3]. This is mainly attributed to the orthonormality of $y_i(t;\omega)$ coefficients in the BO formulation, which maintains a well-conditioned representation of the stochastic subspace at all times. However, in the DO decomposition, the stochastic coefficients $y_i(t;\omega)$ could be highly correlated. This has inspired a hybrid DO/BO method where BO is the dominant solver, but near the eigenvalue crossing the solver switches to DO [40].

Both DO and BO decompositions perform poorly when the covariance matrix is singular or near singular. In the case of DO, the covariance matrix is full, while in the case of BO the covariance matrix is diagonal. In DO the inverse of the covariance matrix is required for the evolution of the spatial basis and in BO the inverse of the diagonal covariance matrix are needed for the evolution of the stochastic basis. The issue of singular covariance matrix can commonly occur in DO/BO decompositions, since one has to resolve the stochastic system up to a small threshold eigenvalue. This necessitates adaptive DO/BO where modes are added and removed at the threshold eigenvalue [3]. This issue has motivated using pseudo-inverse of the covariance matrix [40], where the eigenvalue of the singular or near-singular mode below a threshold value is replaced with a minimum tolerable value. This approach trades the stability of the DO/BO systems with introducing errors in the system of the order of the minimum tolerable value.

The motivation for this work is to introduce a new decomposition that resolves the aforementioned challenges in using DO and BO. To this end, we present a new methodology in which: (i) the spatial and stochastic bases are represented by a set of time-dependent orthonormal modes; (ii) an additional equation for the evolution of a factorization of the

covariance is derived; and (iii) the condition number of the decomposition is reduced to $\sqrt{\lambda_{max}(t)/\lambda_{min}(t)}$, where $\lambda_{min}(t)$ and $\lambda_{max}(t)$ are the minimum and maximum eigenvalues of the covariance matrix, respectively. A brief comparison of the three methods and their constraints are provided in Table 1.

Table 1: The equations and constraints in vector discretized form for the three methods: DO, BO and DBO. For more details regarding the evolution equations the readers are referred to Appendix B, C and Ref. [3].

	DO	BO	DBO
Spatial Basis	$\dot{\mathbf{U}} = (\mathbf{I} - \mathbf{U}\mathbf{U}^T)\mathbf{F}\mathbf{Y}\mathbf{C}^{-1}$	$\dot{\mathbf{U}} = \mathbf{U}\mathbf{M} + \mathbf{F}\mathbf{Y}$ $\mathbf{M} = \mathbf{Y}^T\dot{\mathbf{Y}}$	$\dot{\mathbf{U}} = (\mathbf{I} - \mathbf{U}\mathbf{U}^T)\mathbf{F}\mathbf{Y}\boldsymbol{\Sigma}^{-1}$
Stochastic Basis	$\dot{\mathbf{Y}} = \mathbf{F}^T\mathbf{U}$	$\dot{\mathbf{Y}} = (\mathbf{F}^T\mathbf{U} - \mathbf{Y}\mathbf{S}^T)\boldsymbol{\Lambda}^{-1}$ $\mathbf{S} = \mathbf{U}^T\dot{\mathbf{U}}$	$\dot{\mathbf{Y}} = (\mathbf{I} - \mathbf{Y}\mathbf{Y}^T)\mathbf{F}^T\mathbf{U}\boldsymbol{\Sigma}^{-T}$
Covariance Factorization	-	-	$\dot{\boldsymbol{\Sigma}} = \mathbf{U}^T\mathbf{F}\mathbf{Y}$
Constraints	$\mathbf{U}^T\mathbf{U} = \mathbf{I}$	$\mathbf{U}^T\mathbf{U} = \boldsymbol{\Lambda}$	$\mathbf{U}^T\mathbf{U} = \mathbf{I}$
	$\mathbf{U}^T\dot{\mathbf{U}} = \mathbf{0}$	-	$\mathbf{U}^T\dot{\mathbf{U}} = \mathbf{0}$
	-	$\mathbf{Y}^T\mathbf{Y} = \mathbf{I}$	$\mathbf{Y}^T\mathbf{Y} = \mathbf{I}$
	-	-	$\dot{\mathbf{Y}}^T\mathbf{Y} = \mathbf{0}$

The structure of this thesis is as follows: In chapter 2, we review the formulation of the DBO representation, its evolution equations and prove the equivalence of this method to the DO and BO methods. We compare the performance of the presented method with DO and BO via several benchmark problems: (i) Stochastic linear advection equation (ii) Stochastic Burgers' equation; and (iii) 2D stochastic incompressible Navier-Stokes equation for flow over a bump.

In chapter 3, we explore the application of this method to solve linear and nonlinear partial differential equations imposed with stochastic boundary conditions. Specifically, we

use the variational principle to derive the evolution equations for the stochastic modes, spatial modes and the factor of the covariance matrix. The variational principle also factors in the evolution of the spatial modes at the boundary and presents evolution equations for boundary points. The evolution equations are derived for DBO and DO. The method is then applied for three different stochastic boundary types: Dirichlet, Neumann and Robin boundary conditions. We consider the following benchmark problems to evaluate the performance of the method: (i) Stochastic linear advection-diffusion equation, (ii) Stochastic Burgers' equation, (iii) 2D stochastic advection diffusion equation. The global errors and the boundary errors are compared for both DBO and DO.

In chapter 4 and 5, we shift gears and demonstrate the application of the current work for solving deterministic PDEs. We derive the evolution equations for time-dependent basis for a multi-dimensional variable. The following demonstration cases are used to illustrate the prowess of the method in chapter 5: (i) Linear advection diffusion equation, (ii) Vortex dipole (iii) 2D temporally evolving jet, and (iv) 3D temporally jet.

In chapter 7, we conclude this work with a brief summary and chapter 6 sets the future directions and applications of the presented methodology.

2.0 DBO Representation of Stochastic Fields

This chapter gives details of the notations and definitions of stochastic fields. In the first section of this chapter, we define the properties of stochastic fields like inner product, L_2-norm, expectation, covariance operator and a *quasimatrix*. The second section briefly describes the system of stochastic PDEs. We then define the DBO decomposition to derive the evolution equations of each of the components of the DBO decomposition. It is also shown that the DO, BO and DBO decompositions are equivalent and can be transformed from one form to the other using the equivalence relations. We further, show the ranking of modes in the stochastic and spatial subspace of DBO and resolve the issue of time redundancy using the approach of constraints and degrees of freedom. A few demonstration cases are used to study the numerical properties of this method. We first take a look at the stochastic linear advection diffusion equation where the stochasticity is introduced in the system through the velocity. Using the analytical solution, we can evaluate the numerical performance of this method for DO and DBO. The stochastic Burgers' equation with manufactured solution is considered as the second case. The manufactured solution approach is used to verify the numerical accuracy of codes. We use this method to control the condition number of the matrix inversion for the DO, BO and DBO methods and study the errors for each of the methods. Additionally, the DBO method is applied to Burgers' equation with stochastic forcing and to Burgers' equation with high-dimensional random initial conditions. We also consider the case of random initial conditions for a stochastic incompressible Navier-Stokes equation.

2.1 Definitions and Notation

We denote a random vector field by $u(x,t;\omega)$, where $x \in D$ is the spatial coordinate in the physical domain $D \subset \mathcal{R}^d$, where d=1,2 or 3, and $t > 0$ is time and $\omega \in \Omega$ is the random event in the sample space Ω. The inner product in the spatial domain between two random

fields $u(x,t;\omega)$ and $v(x,t;\omega)$ is then defined as:

$$\langle u(x,t;\omega), v(x,t;\omega)\rangle = \int_D u(x,t;\omega)v(x,t;\omega)dx,$$

and the L_2 norm induced by the above inner product is:

$$\left\|u(x,t;\omega)\right\|_2 = \left\langle u(x,t;\omega)\ ,\ u(x,t;\omega)\right\rangle^{1/2}.$$

The expectation of the random field is defined as:

$$\bar{u}(x,t) = \mathbb{E}[u(x,t,\omega)] = \int_\Omega u(x,t;\omega)\rho(\omega)d\omega,$$

where $\rho(\omega)$ is the probability density function. The inner product in the random space is defined as the correlation between two random fields:

$$\mathbb{E}[u(x,t;\omega)v(x,t;\omega)] = \int_\Omega u(x,t;\omega)v(x,t;\omega)\rho(\omega)d\omega.$$

The covariance operator between two random fields at time t is then obtained from:

$$C(x,x',t) = \mathbb{E}\big[(u(x,t;\omega) - \bar{u}(x,t))(v(x',t;\omega) - \bar{v}(x',t))\big].$$

We introduce the *quasimatrix* notation as defined in [41], in which one of the dimensions is discrete as usual but the other dimension is continuous:

$$U(x,t) = \Big[u_1(x,t)\ \Big|\ u_2(x,t)\ \Big|\cdots\Big|\ u_r(x,t)\Big],$$

$$Y(t;\omega) = \Big[y_1(t;\omega)\ \Big|\ y_2(t;\omega)\ \Big|\cdots\Big|\ y_r(t;\omega)\Big],$$

where $U(x,t)$ and $Y(t;\omega)$ are quasimatrices of size $\infty\times r$. The inner product for two quasimatrices $U(x,t) = \Big[u_1(x,t)\ \Big|\ u_2(x,t)\ \Big|\cdots\Big|\ u_{r_1}(x,t)\Big]$ and $V(x,t) = \Big[v_1(x,t)\ \Big|\ v_2(x,t)\ \Big|\cdots\Big|\ v_{r_2}(x,t)\Big]$ is defined by a matrix A such that,

$$A = \langle U(x,t), V(x,t)\rangle,$$

where

$$A_{ij} = \langle u_i(x,t), v_j(x,t)\rangle, \qquad i = 1,2,...,r_1, \quad j = 1,2,..,r_2. \tag{2.1}$$

A is a matrix of dimensions $r_1 \times r_2$. In general, for the case of $r_1 = r_2$, matrix A is not symmetric.

2.2 System of Stochastic PDEs

We consider the following stochastic partial differential equation (SPDE), which defines the system evolution:

$$\frac{\partial u(x,t;\omega)}{\partial t} = \mathscr{F}(u(x,t;\omega)), \qquad x \in D, \omega \in \Omega, \tag{2.2a}$$

$$u(x,t_0;\omega) = u_0(x;\omega), \qquad x \in D, \omega \in \Omega, \tag{2.2b}$$

$$\mathscr{B}(u(x,t;\omega)) = h(x,t), \qquad x \in \partial D, \tag{2.2c}$$

where $\mathscr{F}$ is, in general, a non-linear differential operator, and $\mathscr{B}$ is, in general, a linear differential operator, and ∂D denotes the boundary of the domain D. In this work we consider deterministic boundary conditions. For an algorithm to treat random boundary conditions for time-dependent subspaces, see reference [42].

2.3 Dynamically Bi-orthonormal Decomposition

We consider the following decomposition,

$$u(x,t;\omega) = \bar{u}(x,t) + \sum_{j=1}^{r}\sum_{i=1}^{r} u_i(x,t)\Sigma_{ij}(t)y_j(\omega,t) + e(x,t;\omega), \tag{2.3}$$

which is referred to as the *dynamically bi-orthonormal (DBO)* decomposition. In the above expression $u_i(x,t), i = 1,2,\ldots,r$ are a set of orthonormal spatial modes:

$$\langle u_i(x,t), u_j(x,t)\rangle = \delta_{ij},$$

and they constitute the spatial basis for the DBO decomposition, and $y_i(\omega,t), i = 1,2,\ldots,r$ are a set of orthonormal stochastic modes:

$$\mathbb{E}[y_i(t;\omega)y_j(t;\omega)] = \delta_{ij},$$

that have zero mean i.e., $\mathbb{E}[y_i(t;\omega)] = 0, i = 1,2,\ldots,r$, the $\Sigma_{ij}(t)$ represents a factorization of the covariance matrix and $e(x,t;\omega)$ is the reduction error. Moreover, both the spatial and

stochastic coefficients are dynamically orthogonal i.e., the rate of change of these subspaces is orthogonal to the space spanned by these modes:

$$\frac{\partial U(x,t)}{\partial t} \perp U(x,t) \iff \left\langle \frac{\partial u_i(x,t)}{\partial t}, u_j(x,t) \right\rangle = 0 \qquad i,j = 1,...,r, \tag{2.4}$$

$$\frac{dY(t;\omega)}{dt} \perp Y(t;\omega) \iff \mathbb{E}\left[\frac{dy_i(t;\omega)}{dt} y_j(t;\omega)\right] = 0 \qquad i,j = 1,...,r. \tag{2.5}$$

If the spatial and stochastic modes are orthonormal at $t = 0$, imposing the above constraints ensures the orthonormality of the two bases for all time since:

$$\frac{d}{dt}\langle u_i(x,t), u_j(x,t)\rangle = \left\langle \frac{\partial u_i(x,t)}{\partial t}, u_j(x,t) \right\rangle + \left\langle u_i(x,t), \frac{\partial u_j(x,t)}{\partial t} \right\rangle = 0 \qquad i,j = 1,...,r, \tag{2.6}$$

and similarly,

$$\frac{d}{dt}\mathbb{E}[y_i(t;\omega)y_j(t;\omega)] = \mathbb{E}[\frac{dy_i(t;\omega)}{dt} y_j(t;\omega)] + \mathbb{E}[y_i(t;\omega)\frac{dy_j(t;\omega)}{dt}] = 0, \qquad i,j = 1,...,r. \tag{2.7}$$

We show in Section 2.7, that imposing the above constraints leads to a unique decomposition. The covariance operator is approximated from the DBO decomposition as in the following:

$$\begin{aligned}
\mathcal{C}(x,x',t) &= \mathbb{E}[u_i(x,t)\Sigma_{ij}(t)y_j(t;\omega)u_m(x',t)\Sigma_{mn}(t)y_n(t;\omega)] \\
&= u_i(x,t)u_m(x',t)\Sigma_{ij}(t)\Sigma_{mn}(t)\mathbb{E}[y_j(t;\omega)y_n(t;\omega)] \\
&= u_i(x,t)u_m(x',t)\Sigma_{ij}(t)\Sigma_{mn}(t)\delta_{jn} \\
&= u_i(x,t)u_m(x',t)\Sigma_{ij}(t)\Sigma_{mj}(t),
\end{aligned} \tag{2.8}$$

where we have used the orthonormality condition imposed on the stochastic basis. The matrix $\Sigma(t) \in \mathbb{R}^{r\times r}$ is a factorization of the reduced covariance matrix $C(t) \in \mathbb{R}^{r\times r}$ as in the following:

$$C(t) = \Sigma(t)\Sigma(t)^T, \tag{2.9}$$

and it is related to the covariance matrix in the full-dimensional space with:

$$\mathcal{C}(x,x',t) = U(x,t)C(t)U^T(x',t). \tag{2.10}$$

2.4 DBO Field Equations

In this section, we present closed-form evolution equations for $\bar{u}(x,t)$, $\Sigma(t)$, $Y(t;\omega)$ and $U(x,t)$ for the DBO decomposition.

Theorem 2.4.1. *Let Eq.(2.3) represent the DBO decomposition of the solution of SPDE given by Eq.(2.2). Then, under the assumptions of the DBO decomposition, the closed-form evolution equations for the mean, covariance factorization, stochastic and spatial bases are expressed by:*

$$\frac{\partial \bar{u}(x,t)}{\partial t} = \mathbb{E}[\mathscr{F}(u(x,t;\omega))], \tag{2.11a}$$

$$\frac{d\Sigma_{ij}(t)}{dt} = \left\langle u_i(x,t), \mathbb{E}[\tilde{\mathscr{F}}(u(x,t;\omega))y_j(t;\omega)] \right\rangle, \tag{2.11b}$$

$$\frac{dy_i(t;\omega)}{dt} = \left[\left\langle u_j(x,t), \tilde{\mathscr{F}}(u(x,t;\omega)) \right\rangle - \left\langle u_j(x,t), \mathbb{E}[\tilde{\mathscr{F}}(u(x,t;\omega))y_k(t;\omega)] \right\rangle y_k(t;\omega) \right] \Sigma_{ji}(t)^{-1}, \tag{2.11c}$$

$$\frac{\partial u_i(x,t)}{\partial t} = \left[\mathbb{E}[\tilde{\mathscr{F}}(u(x,t;\omega))y_j(t;\omega)] - u_k(x,t) \left\langle u_k(x,t), \mathbb{E}[\tilde{\mathscr{F}}(u(x,t;\omega))y_j(t;\omega)] \right\rangle \right] \Sigma_{ij}(t)^{-1}, \tag{2.11d}$$

where $\tilde{\mathscr{F}}(x,t;\omega)$ is a mean-subtracted quantity

$$\tilde{\mathscr{F}}(u(x,t;\omega)) = \mathscr{F}(u(x,t;\omega)) - \mathbb{E}[\mathscr{F}(u(x,t;\omega))].$$

The associated boundary conditions are given by:

$$\mathscr{B}[\overline{u}(x,t)] = h(x,t), \qquad x \in \partial D, \tag{2.12a}$$

$$\mathscr{B}[u_i(x,t)] = 0, \qquad x \in \partial D. \tag{2.12b}$$

The proof for the above theorem is given in Appendix A. We note that the inverse of the factorization of the covariance matrix $\Sigma(t)$ appears in the DBO evolution equations, as opposed to the inverse covariance matrix $C(t)$ or inverse of the matrix of covariance eigenvalues that appear in the DO and BO equations, respectively. As a result the DBO systems has the condition number of $\sqrt{\lambda_{max}(t)/\lambda_{min}(t)}$ as opposed to DO and DBO that have condition numbers of $\lambda_{max}(t)/\lambda_{min}(t)$, where the minimum and maximum eigenvalues of the covariance matrix.

2.5 Equivalence of DO, BO and DBO Methods

Two decompositions are equivalent if they represent the same random fields for all times. The spatial subspaces of two equivalent decompositions are identical and therefore, one can find invertible transformation matrices that maps one subspace to the other. This amounts to an *in-subspace* rotation. The same is true for stochastic subspaces of two equivalent decompositions. The equivalence of DO and BO was first shown in [3]. In this section, we show that DBO is equivalent to DO and BO. We first show that DBO is equivalent to DO and BO and then derive the equivalence relations. In the following section, $\{U_{DO}(x,t), Y_{DO}(t;\omega)\}$, $\{U_{BO}(x,t), Y_{BO}(t;\omega)\}$ and $\{U_{DBO}(x,t), \Sigma_{DBO}(t), Y_{DBO}(t;\omega)\}$ represent the DO, BO and DBO decomposition of the SPDE in Eq.(2.2), respectively.

Lemma 2.5.1. *Let DO and DBO be equivalent via the transformations: $U_{DO} = U_{DBO}R_u$ and $Y_{DO} = Y_{DBO}W_y$, where $R_u \in \mathbb{R}^{r\times r}$ and $W_y \in \mathbb{R}^{r\times r}$. Then: (i) R_u is an orthogonal matrix (ii) $W_y = \Sigma_{DBO}^T R_u$, and (iii) $\dfrac{dR_u}{dt} = 0$.*

The proof for Lemma (2.5.1) is given in Appendix B.

Theorem 2.5.1. *Let $U_{DO}(x,t)$, $Y_{DO}(t;\omega)$ represent the DO decomposition of SPDE in Eq.(2.2) and let $U_{DBO}(x,t)$, $\Sigma_{DBO}(t)$ and $Y_{DBO}(t;\omega)$ represent its DBO decomposition. Suppose that at $t = 0$ the two bases are equivalent i.e., $U_{DO}(x,t_0) = U_{DBO}(x,t_0)R_u(t_0)$ and $Y_{DO}(t_0;\omega) = Y_{DBO}(t_0;\omega)W_y(t_0)$. Then the two subspaces remain equivalent for all $t > 0$.*

The proof for Theorem (2.5.1) is given in Appendix B.

Lemma 2.5.2. *Let DBO and BO be equivalent via the transformations: $U_{DBO} = U_{BO}W_u$ and $Y_{DBO} = Y_{BO}R_y$, where $W_u \in \mathbb{R}^{r\times r}$ and $R_y \in \mathbb{R}^{r\times r}$. Then: (i) R_y is an orthogonal matrix (ii) $\Sigma_{DBO} = W_u^{-1}R_y$(iii) $\frac{dW_u}{dt} = -(M + \Lambda^{-1}G)W_u$ (iv) $\dfrac{dR_y}{dt} = (S^T - G^T)\Lambda^{-1}R_y$; where $M = \mathbb{E}\left[Y_{BO}^T \frac{dY_{BO}}{dt}\right]$, $S = \left\langle U_{BO}, \dfrac{\partial u_{BO}}{\partial t}\right\rangle$ and $G = \left\langle U_{BO}, \mathbb{E}[\tilde{\mathscr{F}}Y_{BO}]\right\rangle$.*

The proof for Lemma (2.5.2) is given in Appendix C.

Theorem 2.5.2. *Let $U_{BO}(x,t)$, $Y_{BO}(t;\omega)$ represent the BO decomposition of SPDE in Eq.(2.2) and let $U_{DBO}(x,t)$, $\Sigma_{DBO}(t)$ and $Y_{DBO}(t;\omega)$ represent its DBO decomposition. Suppose that at $t = 0$ the two bases are equivalent i.e., $U_{DBO}(x,t_0) = U_{BO}(x,t_0)W_u(t_0)$ and*

$Y_{DBO}(t_0;\omega) = Y_{BO}(t_0;\omega)R_y(t_0)$. *Then the two subspaces remain equivalent for all* $t > 0$.

The proof for Theorem (2.5.2) is given in Appendix C.

Remark 2.5.1. *Based on the equivalence relation between BO and DBO, and that between DBO and DO; it can be easily shown that the equivalence between BO and DO obtained from [3] would be equal to* $U_{DO} = U_{BO}W_uR_u$ *and* $Y_{DO} = Y_{BO}R_yW_y$.

In Fig.(1) we summarize the equivalence relations between DBO, DO and BO. The equivalence relation between BO and DO and the definition of matrices: M, G, S and Σ are taken from [3].

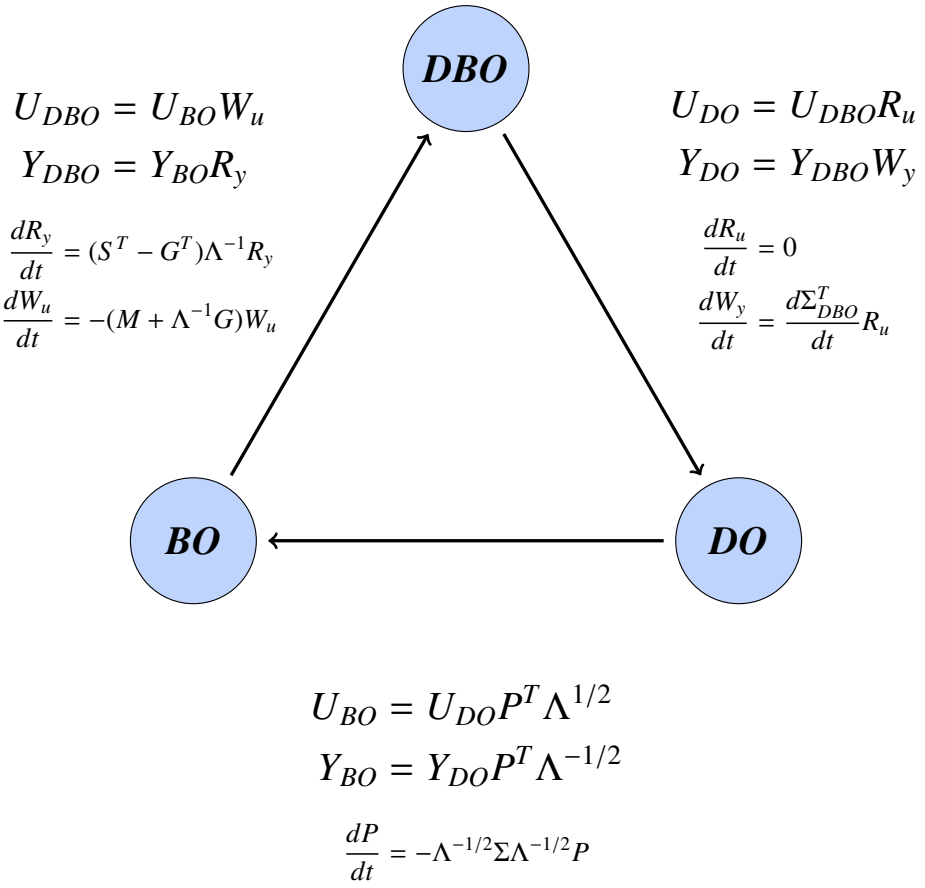

Figure 1: Equivalence relations between the three methods. The equivalence between DO and BO and the definitions of matrices S, G, M, Σ are taken from reference [3].

2.6 Mode Ranking

In this section, we determine the ranking of the modes in the stochastic and spatial subspace of DBO as performed in [43]. The spatial and stochastic DBO modes are ranked in the direction of the most energetic modes i.e., the modes are ranked based on the variance captured by each mode. To this end, we perform a singular value decomposition (SVD) of the Σ_{DBO} matrix given by:

$$\Sigma_{DBO}(t) = \Psi_U(t)\Lambda(t)^{1/2}\Psi_Y^T(t),$$

where $\Psi_U(t)$ and $\Psi_Y(t)$ are the left-singular vectors and the right-singular vectors of Σ_{DBO}, respectively. $\Lambda(t)$ is a diagonal matrix containing the eigenvalues of the covariance matrix. The eigenvalues are ranked such that $\lambda_1(t) \geq \lambda_2(t) \geq \cdots \geq \lambda_r(t)$. The ranked DBO modes based on the variance i.e., $\lambda_i(t)$, are obtained by an in-subspace rotation as in the following:

$$\widetilde{U}_{DBO}(t) = U_{DBO}(t)\Psi_U(t),$$

$$\widetilde{Y}_{DBO}(t) = Y_{DBO}(t)\Psi_Y(t).$$

2.7 Redundancy in Time

All three components of the DBO decomposition i.e., $U(x,t)$, $Y(x,t)$ and $\Sigma(t)$ are time dependent. The issue of time redundancy also exists in both BO and DO decompositions. We present a simple but insightful and unifying approach to clarify the *constraints* and *degrees of freedom* (DOF) in devising new time-dependent decompositions. For simplicity, we consider a finite-dimensional example. In particular, we consider the full-dimensional decomposition of a time-dependent matrix $A(t) \in \mathbb{R}^{n\times s}$. In this simplification $A(t)$ can be considered as a discrete representation of the mean subtracted random field, where n is the number of discrete points in spatial domain and s is the number of samples of the random field. In this section, we determine the degrees of freedom and the number of constraints imposed by a decomposition, and we show that in DBO decompositions the total number of constraints

is equal to the number of degrees of freedom — leading to a unique decomposition. In the following analysis we drop the explicit dependence on t for brevity.

We consider the DBO decomposition, which is given by: $A = U\Sigma Y^T$, where the spatial modes and stochastic modes are a set of orthonormal bases. The total DOF for DBO are given by the total number of elements in each of the matrices in the decomposition i.e., $n \times s$ entries in U matrix, $s \times s$ entries in the Σ matrix and $s \times s$ entries in the Y matrix. Thus, the total DOF is: $N_{DOF} = n \times s + s \times s + s \times s$. The constraints imposed by the DBO decomposition are as follows: (i) There are $N_{c1} = n \times s$ constraints imposed by the compatibility conditions $A_{ij} = U_{ik}\Sigma_{km}Y_{jm}$. (ii) The orthonormality of stochastic and spatial modes ($\langle u_i, u_j \rangle = \delta_{ij}$ and $\mathbb{E}[y_i y_j] = \delta_{ij}$) imposes $s(s+1)/2$ constraints each, which in total imposes $N_{c2} = s(s+1)$. Note that we only need to count the constraints for for $j < i$, because for $j > i$ the constraints are equivalent to those of $i < j$, since $\langle u_i, u_j \rangle = \langle u_j, u_i \rangle$ and $\mathbb{E}[y_i y_j] = \mathbb{E}[y_j y_i]$, and therefore they are not independent constraints and thus not counted. (iii) The dynamically orthogonal constraints for spatial and stochastic modes ($\langle \dot{u}_i, u_j \rangle = 0$ and $\mathbb{E}[\dot{y}_i y_j] = 0$) imposes $s(s-1)/2$ constraints each. Note that $\langle \dot{u}_i, u_i \rangle = 0, i = 1, 2, \ldots, s$ does not impose independent constraints as $\langle u_i, u_i \rangle = 1$ already enforces this condition. This can be seen by taking the time derivative of the orthonormality constraints:

$$\frac{d}{dt} \langle u_i, u_i \rangle = \langle \dot{u}_i, u_i \rangle + \langle u_i, \dot{u}_i \rangle = 2 \langle \dot{u}_i, u_i \rangle = 0.$$

Similarly, $\mathbb{E}[\dot{y}_i y_i] = 0, i = 1, 2, \ldots, s$ does not impose independent constraints. Thus, the total constraints from the dynamically orthogonal condition are $N_{c3} = s(s-1)$.

The total number of constraints for the DBO decomposition is $n \times s + s(s+1) + s(s-1)$, which is equal to the number of degrees of freedom, and this results in a fully determined DBO decomposition for matrix A. A similar breakdown of constraints and degrees of freedom can be performed for DO and BO and is summarized in in Table 2.

We conclude that to obtain a unique time-dependent decomposition, the number of degrees of freedom and the number of constraints need to be equal. Introducing additional degrees of freedom requires additional constraints to keep the system fully determined and thus unique. In the light of the above analysis, DBO allows for $s \times s$ additional degrees of freedom compared to DO by adding the matrix Σ to the decomposition. These additional

Table 2: Number of constraints and degrees of freedom for BO, DO and DBO decompositions. Each decomposition imposes $n \times s$ compatibility constraints, which are not listed.

Method	Matrix Decomposition	Degrees of Freedom	Constraints
BO	$A_{n\times s} = U_{n\times s} Y^T_{s\times s}$	$ns + s^2$	$\langle U, U\rangle = \Lambda$: $\frac{s(s-1)}{2}$
			Λ is diagonal matrix
			$\mathbb{E}[Y^T Y] = I$: $\frac{s(s+1)}{2}$
DO	$A_{n\times s} = U_{n\times s} Y^T_{s\times s}$	$ns + s^2$	$\langle U, U\rangle = I$: $\frac{s(s+1)}{2}$
			$\left\langle \dot{U}, U \right\rangle = 0$: $\frac{s(s-1)}{2}$
DBO	$A_{n\times s} = U_{n\times s} \Sigma_{s\times s} Y^T_{s\times s}$	$ns + s^2 + s^2$	$\langle U, U\rangle = I$: $\frac{s(s+1)}{2}$
			$\mathbb{E}[Y^T Y] = I$: $\frac{s(s+1)}{2}$
			$\left\langle \dot{U}, U \right\rangle = 0$: $\frac{s(s-1)}{2}$
			$\mathbb{E}[\dot{Y}^T Y] = 0$: $\frac{s(s-1)}{2}$

constraints are then utilized to enforce the orthonormality and dynamically orthogonal conditions on the stochastic coefficients Y. The orthonormality of Y coefficients in the DBO decomposition cannot be enforced in the DO decomposition. As we will demonstrate this loss of orthonormality of Y in the DO decomposition can lead to degradation of accuracy in highly ill-conditioned problems.

2.8 Demonstration Cases

2.8.1 1D Stochastic Linear Advection Equation

We consider linear advection governed by:

$$\frac{\partial u}{\partial t} + V(\omega)\frac{\partial u}{\partial x} = 0, \qquad x \in [0, 2\pi] \quad \text{and} \quad t \in [0, t_f], \tag{2.13a}$$

$$u(x, 0) = \sin(x), \qquad x \in [0, 2\pi], \tag{2.13b}$$

with periodic boundary condition. The randomness in the system comes from the advection velocity $V(\omega)$. The random velocity is specified by $V(\omega) = \bar{v} + \sigma\xi(\omega)$, where $\bar{v} = 1.0$, $\sigma = 1.0$ and $\xi(\omega)$ is a uniform random variable in the interval of $\xi \sim \mathcal{U}[-1, 1]$ with variance $1/3$. The physical domain is discretized using the Fourier spectral method with $N_s = 512$ Fourier modes. The random space is one dimensional and is discretized with the probabilistic collocation method (PCM) with $N_r = 256$ Legendre-Gauss points. The third-order Runge-Kutta scheme is used for the time integration with $\Delta t = 10^{-3}$. At $t = 0$, the stochastic fluctuations are zero, and therefore, the simulation is initialized at $t = \Delta t$ to avoid singularity of the covariance matrix. The system is numerically evolved till $t_f = 10$. The linear advection Eq.(2.13) has a closed-form solution as follows:

$$u(x, t; \omega) = g(x - V(\omega)t) = \sin(x - (\bar{v} + \sigma\xi(\omega))\pi t). \tag{2.14}$$

This system can be expressed exactly with KL modes and the reduction order of $r = 2$ as follows:

$$u(x, t; \omega) = \bar{u}(x, t) + \sum_{i=1}^{r} \sqrt{\lambda_i}(t) u_i(x, t) y_i(t, \omega),$$

where,

$$\bar{u}(x, t) = \sin(x - \bar{v}t\pi)\frac{\sin(\sigma\pi t)}{\sigma\pi t},$$

$$u_1(x, t) = \frac{1}{\sqrt{\pi}}\sin(x - \bar{v}\pi t), \qquad u_2(x, t) = \frac{-1}{\sqrt{\pi}}\cos(x - \bar{v}\pi t),$$

$$y_1(t; \omega) = \frac{\sqrt{\pi}}{\sqrt{\lambda_1(t)}}\left(\cos(\sigma\xi\pi t) - \frac{\sin(\sigma\pi t)}{\sigma\pi t}\right), \qquad y_2(t; \omega) = \frac{\sqrt{\pi}}{\sqrt{\lambda_2(t)}}\sin(\sigma\xi\pi t),$$

$$\lambda_1(t) = 1 - \frac{\sin(2\sigma\pi t)}{2\sigma\pi t}, \qquad \lambda_2(t) = 1 + \frac{\sin(2\sigma\pi t)}{2\sigma\pi t} - \frac{2\sin^2(\sigma\pi t)}{(\sigma\pi t)^2}.$$

The mean, spatial and stochastic bases of the DBO decomposition are initialized with KL modes given above. The covariance factorization is initialized by:

$$\Sigma(t) = \begin{bmatrix} \sqrt{\lambda_1(t)} & 0 \\ 0 & \sqrt{\lambda_2(t)} \end{bmatrix}. \tag{2.15}$$

In Fig.(2a-2b), the L_2 error of the mean and variance for both DO and DBO methods are shown, respectively. The L_2 norm of the error of the mean ($\epsilon_m(t)$) is computed as in the following:

$$\epsilon_m(t) = \left(\int_D (\bar{u}(x,t) - \bar{u}_{DBO}(x,t))^2 dx \right)^{1/2}, \tag{2.16}$$

where $\bar{u}(x,t)$ represents the mean of the analytical solution and $\bar{u}_{DBO}(x,t)$ represents the mean obtained from the DBO evolution equations.The error of the variance ($\epsilon_v(t)$) is calculated using the L_2-norm in both the spatial and stochastic dimensions:

$$E(x,t;\omega) = u(x,t;\omega) - \bar{u}(x,t) - \sum_{j=1}^{r}\sum_{i=1}^{r} u_{DBO_i}(x,t)\Sigma_{DBO_{ij}}(t)y_{DBO_j}(\omega,t), \tag{2.17a}$$

$$\epsilon_v(t) = \left(\int_D \mathbb{E}[E(x,t;\omega)^2] dx \right)^{1/2}, \tag{2.17b}$$

where $u(x,t;\omega)$ represents the analytical stochastic field, $\bar{u}(x,t)$ represents the mean of the analytical stochastic flow field, whereas $u_{DBO_i}(x,t)$, $\Sigma_{DBO_{ij}}(t)$ and $y_{DBO_j}(\omega,t)$ represent the solutions of the components of the DBO decomposition obtained from the DBO evolution equations.

Since the solution of this problem can be exactly expressed with two DBO modes, the errors in the mean and variance come from the temporal, spatial and the PCM discretization of the random space. To the end, we present mean and variance errors for two values of $\Delta t = 10^{-3}$ and 2×10^{-4}, in which the smaller Δt shows smaller errors. We also refined the resolution for spatial and random discretizations, and we did not, however, observe noticeable change in the mean and variance errors. This demonstrates that the temporal discretization is the main source of error. For long time integration, the resolution of solving Eq.(2.11c) must increase in time i.e., higher number of samples of ξ, to maintain a desired level of accuracy as increasing time increases the wave number of $y_i(t;\omega)$ modes. However, in the DBO decomposition, the computational cost of increasing resolution in the random space is

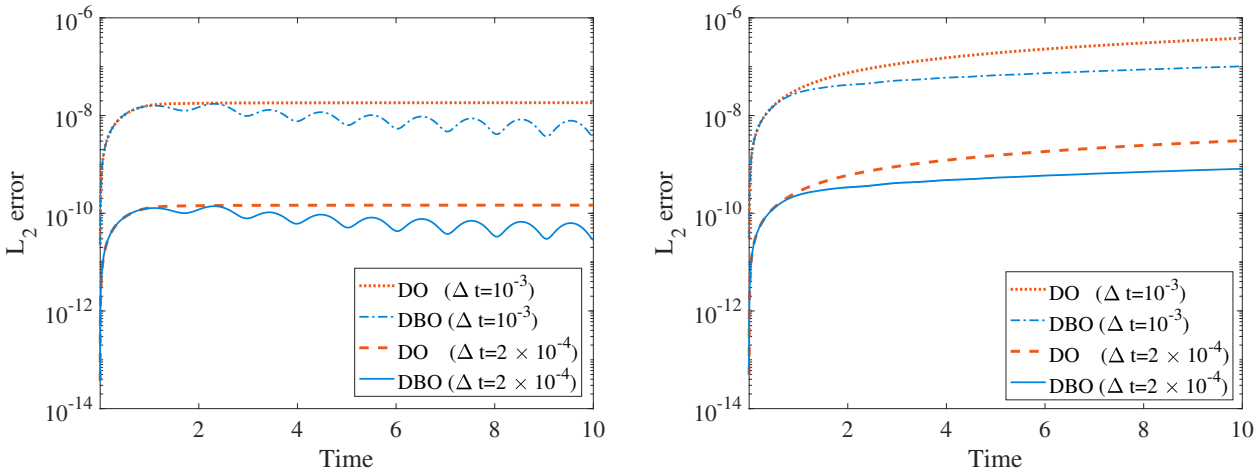

(a) Mean error

(b) Variance error

Figure 2: Stochastic linear advection equation: The L_2 errors for the mean and the variance are compared with the DO method.

insignificant, as we solve the stochastic ODE of small order (here $r = 2$) given by Eq.(2.11c). This is in contrast to the PCM method, in which to maintain the desired level of accuracy the PCE order must increase with time, which results in solving larger system of PDEs. See reference [19] for detailed error analysis of the stochastic linear advection equation using PCM. The BO method for this case would diverge because of eigenvalue crossing. It is clear that both DBO and DO show similar errors as they are equivalent. However, the DBO shows slightly smaller errors in both mean and the variance.

2.8.2 Stochastic Burgers' Equation With Manufactured Solution

We consider the stochastic Burgers' equation governed by:

$$\frac{\partial u}{\partial t} + u\frac{\partial u}{\partial x} = \nu\frac{\partial^2 u}{\partial x^2} + f(x,t;\omega), \qquad x \in [0,2\pi] \quad \text{and} \quad t \in [0,t_f]. \tag{2.18a}$$

$$u(x,0;\omega) = g(x), \qquad x \in [0,2\pi]. \tag{2.18b}$$

We consider the following manufactured solution expressed by the KL decomposition with $r = 2$ modes:

$$\bar{u}(x,t) = \sin(x-t),$$
$$u_1(x,t) = \frac{1}{\sqrt{\pi}}\cos(x-t), \qquad u_2(x,t) = \frac{1}{\sqrt{\pi}}\cos(2x-3t),$$
$$y_1(t;\omega) = \sin(\pi\xi_1(\omega)-t), \qquad y_2(t;\omega) = \cos(\pi\xi_2(\omega)-t),$$
$$\lambda_1(t) = (4.5+\sin(t))^2, \qquad \lambda_2(t) = \epsilon^2\cdot(1.5+\cos(3t))^2.$$

We initialize the DBO systems with KL modes similar to the previous example. The stochastic forcing $f(x,t;\omega)$ is calculated accordingly such that the above decomposition satisfies Eq.(2.18). In the above equation $\nu = 0.05$ and $\xi_d \sim \mathcal{U}[-1,1]$. Here, d is the dimension of the random space, which for this case is taken to be $d = 2$. The parameter ϵ scales the smaller eigenvalue i.e., $\lambda_2(t)$, which in turn controls the condition number of the covariance matrix. The physical domain is considered to be periodic. We discretize the spatial domain using the Fourier spectral method with $N_s = 128$ modes. The random space is two-dimensional and is discretized with the ME-PCM (Multi-Element Probabilistic Collocation Method) [9] with 8 elements each containing 4 points in each random direction. Thus, the total points in every random direction is 32, which results in $N_r = 1024$. The third-order Runge-Kutta method is used for the time integration with $\Delta t = 10^{-3}$. Since at $t = 0$ the stochasticity is zero, the numerical computation is started from $t_s = 0.01$. The system is numerically evolved till $t_f = 3\pi$.

The purpose of this case is to compare the performance of DO, BO and DBO methods for cases with ill-conditioned covariance matrices. We also compare the performance of DBO with pseudo-inverse DO (PI-DO) [40], where the authors proposed using pseudo inverse in the presence of singular or near-singular covariance matrices. Two values of ϵ are considered and the evolution of the system for DO, PI-DO, BO and the DBO methods are studied. We use the L_2 error for evaluation of the mean and variance errors i.e., Eq.(2.16) and Eq.(2.17) between the four methods.

In Fig.(3), the evolution of the eigenvalues, mean and variance error are shown for two values of $\epsilon = 10^{-3}$ and $\epsilon = 10^{-5}$. Fig.(3c) and Fig.(3d) show a comparison between the

mean errors for ϵ values 10^{-3} and 10^{-5}, respectively. Similarly, Fig.(3e) and Fig.(3f) show the variance error for ϵ values 10^{-3} and 10^{-5} respectively. The PI-DO case is studied only for the case with $\epsilon = 10^{-5}$, since for the case with $\epsilon = 10^{-3}$ the covariance matrix does not become singular. Two threshold values are used for the inversion of the covariance matrix in the PI-DO method: $\sigma_{th} = 10^{-9}$ and $\sigma_{th} = 10^{-10}$. See reference [40] for more details on the threshold values. As shown in [40], the choice of the threshold value can play a significant role in the performance of PI-DO. Based on the formulation of the eigenvalues, lower values of ϵ creates an ill-conditioned covariance matrix for DO, BO as well as an ill-conditioned Σ matrix for DBO. However, in both DO and BO the condition number for the inversion of the covariance matrix is $\kappa_{DO,BO} = \lambda_1(t)/\lambda_2(t)$, which scales with $1/\epsilon^2$, while the condition number for the inversion of Σ in the DBO decomposition is $\kappa_{DBO} = \sqrt{\lambda_1(t)/\lambda_2(t)}$, which scales with $1/\epsilon$. Since DO, BO and DBO are equivalent, it is expected that they all perform similarly for the well-conditioned covariance matrix, i.e., $\epsilon = 10^{-3}$. This can be seen in Fig.(3a), Fig.(3c) and Fig.(3e), where all three methods exhibit the same levels of error in mean and variance and the eigenvalues of the covariance matrix match well with the true eigenvalues. However, for the case with $\epsilon = 10^{-5}$, it is expected that DBO performs better than BO and DO and this can be seen in Fig.(3b), Fig.(3d) and Fig.(3f). For this case neither DO, BO nor PI-DO can capture the smallest eigenvalue i.e., $\lambda_2(t)$ correctly. As a result they introduce error of the order of $\sqrt{\lambda_2(t)} \sim \mathcal{O}(\epsilon)$, which can be observed in Fig.(3d) and Fig.(3f). As seen in Fig.(3d) and Fig.(3f), the threshold value of $\sigma_{th} = 10^{-9}$ for pseudo-inverse introduces higher order errors than that of the $\sigma_{th} = 10^{-10}$. The pseudo-inverse method introduces $\mathcal{O}(\sigma_{th})$ in the simulation whenever the lowest eigenvalue attains a value lower than the threshold σ_{th}.

We have also investigated the effect of the condition number of the system on the spatial and stochastic modes. In Fig.(4), the two spatial modes and the phase space i.e., $y_1(t;\omega)$ vs. $y_2(t;\omega)$, are shown for four different times: $t = 0.2, 1.2, 3.2$ and 5.2. For the purpose of comparison, the DO and DBO stochastic and spatial modes are transformed to the BO subspace using the transformation relations obtained in Section 2.5. At $t = 0.2$, the spatial modes and stochastic coefficients match well with those of the KL decomposition as shown in Fig.(4a-4c). However, as time progresses to $t = 1.2$ and $t = 3.2$ the ability of the BO,

DO, and PI-DO to retain the near-singular mode deteriorate as shown in Fig.(4e-4f) and Fig.(4h-4i). At time $t = 5.2$, BO, DO, and PI-DO completely fail to capture the lowest variance mode. Moreover, for both DO and PI-DO, the inability to accurately resolve the low-variance mode adversely affects first mode. See Fig.(4g) and Fig.(4j).

2.8.3 1D Burgers' Equation with Stochastic Forcing

In this section, we consider Burgers' equation subject to random forcing where a large number of modes are needed to resolve the system accurately due to nonlinear interaction between the modes. We investigate the effect of low eigenvalues on the accuracy of the solution and the effect of long time integration on the solution for both DO and the DBO methods. The governing equation is given by:

$$\frac{\partial u}{\partial t} + u\frac{\partial u}{\partial x} = \nu\frac{\partial^2 u}{\partial x^2} + \frac{(1+\xi)}{2}\sin(2\pi t), \qquad x \in [0, 2\pi] \quad \text{and} \quad t \in [0, t_f], \tag{2.19a}$$

$$u(x, 0; \omega) = g(x) \qquad x \in [0, 2\pi], \tag{2.19b}$$

where $\nu = 0.04$ and $\xi \sim \mathcal{U}[-1, 1]$ is a one-dimensional uniform random variable and the initial condition is taken to be:

$$g(x) = 0.5(\exp(\cos(x)) - 1.5)\sin(x + 2\pi \cdot 0.37). \tag{2.19c}$$

We use the Fourier spectral method for space discretization with $N_s = 128$ Fourier modes, and PCM is used for the discretization of the one-dimensional random space ξ. We use $N_r = 64$ Legendre-Gauss collocation points. The third-order Runge-Kutta scheme is used for evolving the discrete systems in time with $\Delta t = 10^{-3}$. At $t = 0$ the system is deterministic, hence the covariance matrix is singular. Therefore, neither DO nor DBO decompositions can be initialized at $t = 0$. To this end, we evolve the stochastic systems up to $t_s = 2$ using PCM and the KL decomposition of the solution at this time is taken as the initial condition. This is in accordance to methodology presented in [44].

This case is used to study two properties of an ill-conditioned system on the overall accuracy of the mean and variance: (i) effect of low eigenvalues resulting in an ill-conditioned covariance matrix, (ii) effect of unresolved modes on long term integration. To study the

$\epsilon = 10^{-3}$ $\epsilon = 10^{-5}$

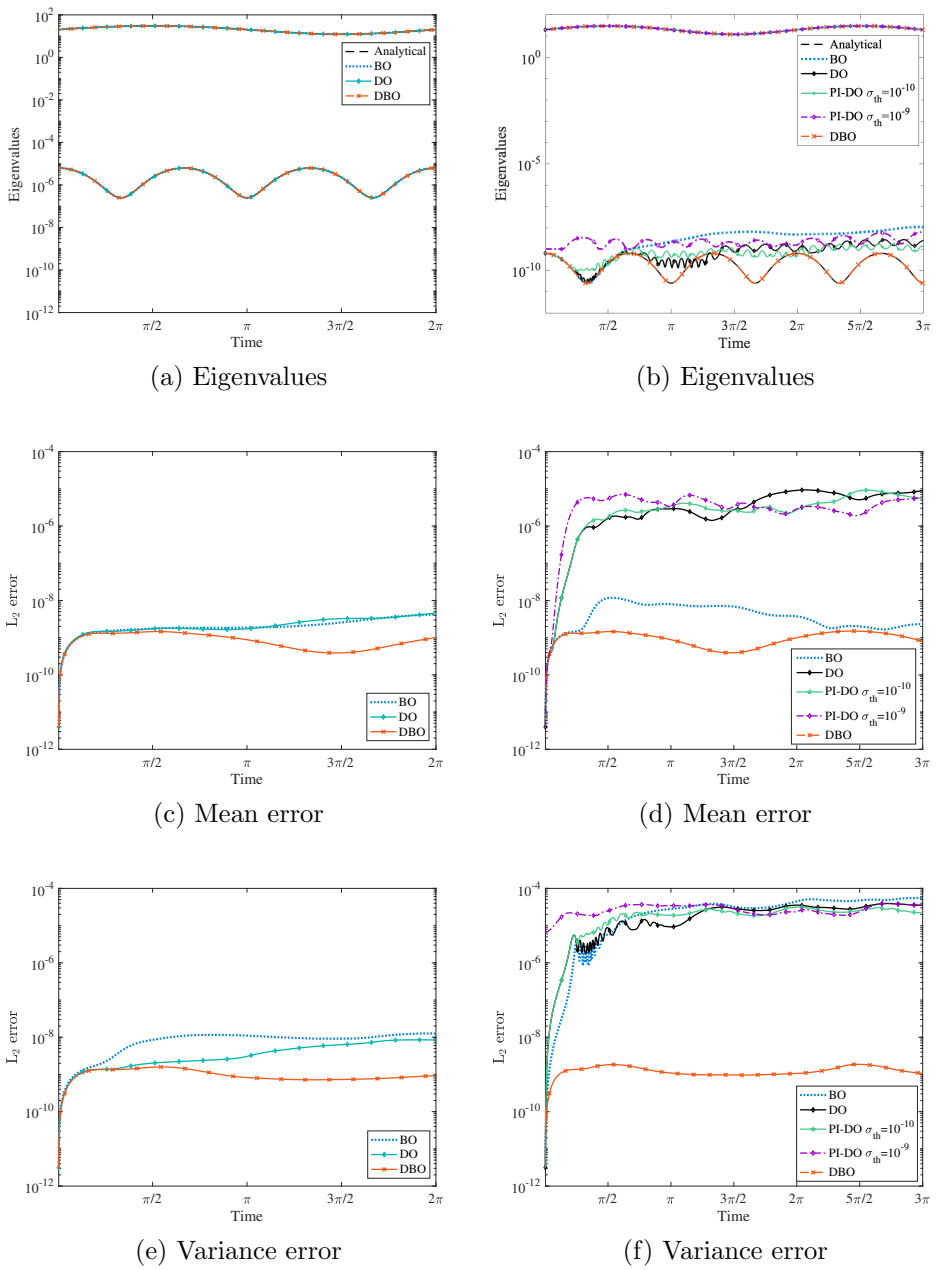

(a) Eigenvalues (b) Eigenvalues

(c) Mean error (d) Mean error

(e) Variance error (f) Variance error

Figure 3: Burgers' equation with manufactured forcing: A comparison between two values of ϵ, which controls the condition number of the system, is shown. The left column:(a),(c) and (e) correspond to the eigenvalues, mean error and variance error for the case with $\epsilon = 10^{-3}$, respectively. The right column:(b),(d) and (f) correspond to the eigenvalues, mean error and variance error for the case with $\epsilon = 10^{-3}$, respectively. It is observed that as the system becomes ill-conditioned for $\epsilon = 10^{-5}$, the errors for the DO, PI-DO and the BO method increase whereas the DBO maintains the same accuracy for both the ϵ values.

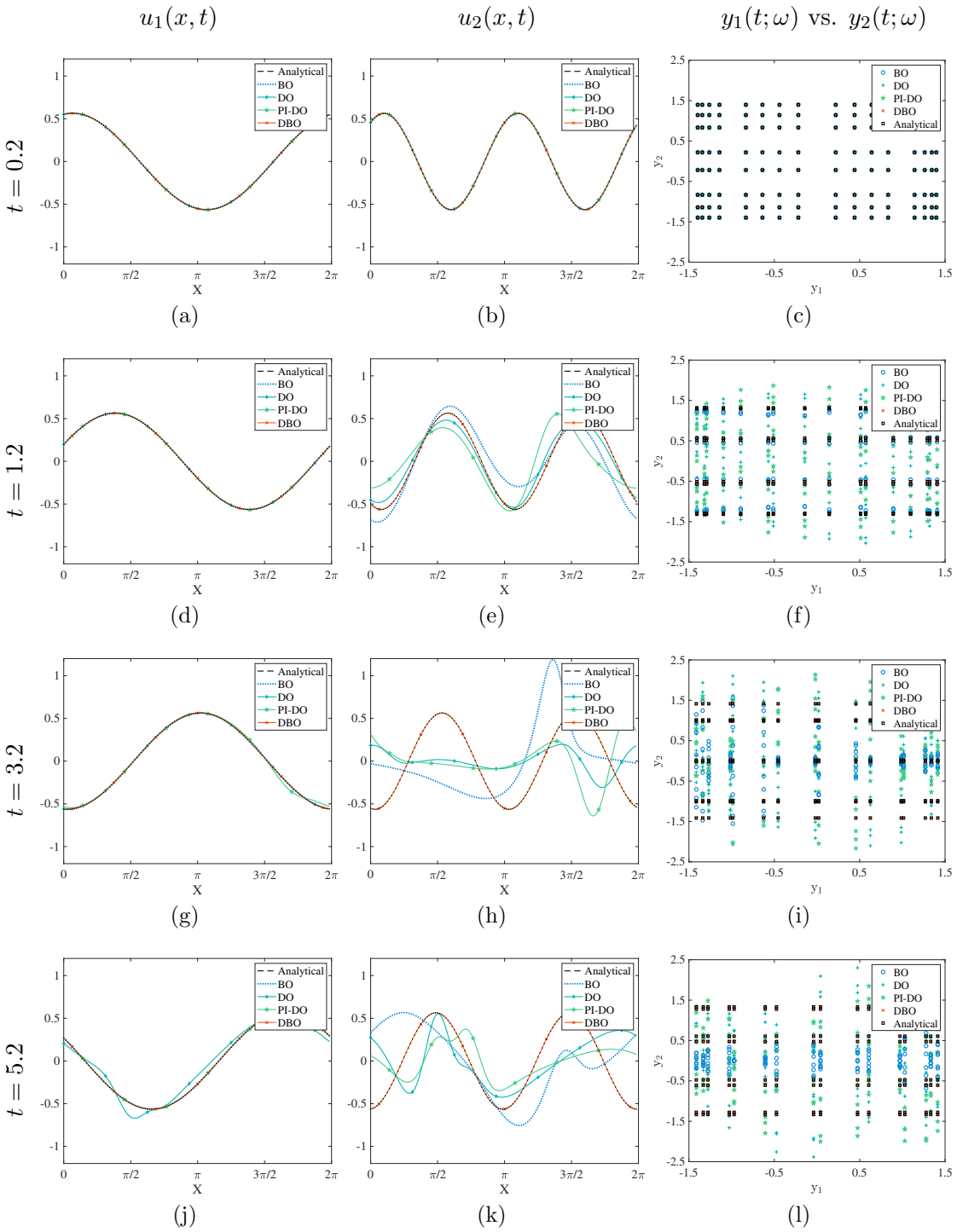

Figure 4: Burgers' equation with manufactured forcing: The two physical modes and the phase space for the stochastic basis are shown at different times as the simulations progresses. All the methods start from the same initial condition. Each row corresponds to the system at $t = 0.1, 1.2, 3.2$ and 5.2. It is observed that the low variance mode is affected first and subsequently as the evolution continues the higher variance mode loses its accuracy as well.

effect of low eigenvalues we consider two reduction sizes of $r = 7$ and $r = 9$ and the system is evolved till $t_f = 3$. Fig.(5) shows the eigenvalues for this case as extracted from the PCM solution. It is observed that modes 8 and 9 (shown in red) have eigenvalues which are the order of 10^{-15}, rendering the covariance matrix C highly ill-conditioned. The mean error for reduction sizes $r = 7$ and $r = 9$ can be seen in Fig.(6a-6b), respectively. The variance error is plotted in Fig.(6c-6d). It can be seen that the lower modes affect the accuracy of the solution for DO. The error affects the solution of the higher modes and we observe an increased error for the DO method in case of reduction order $r = 9$. The DBO method, on the other hand, resolves the lower mode accurately without affecting the accuracy of the higher modes. In fact adding additional modes, improves the accuracy of the DBO solution as seen from the variance error plots in Fig.(6d). The solutions for the long time integration

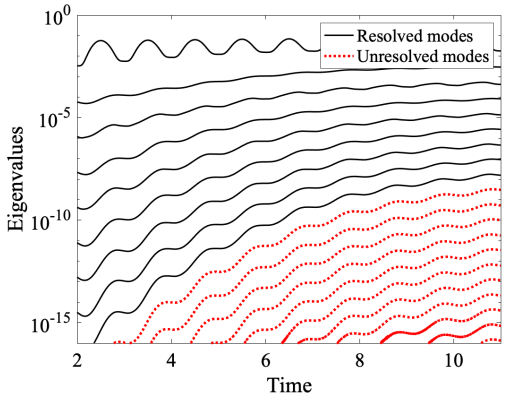

Figure 5: Burgers' equation with stochastic forcing: Growth in the eigenvalues as the system evolves. The modes shown in red dotted lines are the unresolved modes i.e., modes which are not included in the simulations. These eigenvalues are obtained by performing Karhunen-Loéve decomposition on the instantaneous samples.

case for the stochastic Burgers' equation is shown in Fig.(7). Between $t = 2$ and $t = 3$, we observe that the DO has higher error as the lower modes affect the accuracy of the higher modes. This result is same as seen from the previous case Fig.(6). As the lower modes start gaining energy, the error from the unresolved modes dominates the error of the effect of lower modes and hence, we observe that the error for both the DO and the DBO methods is the same as time progresses.

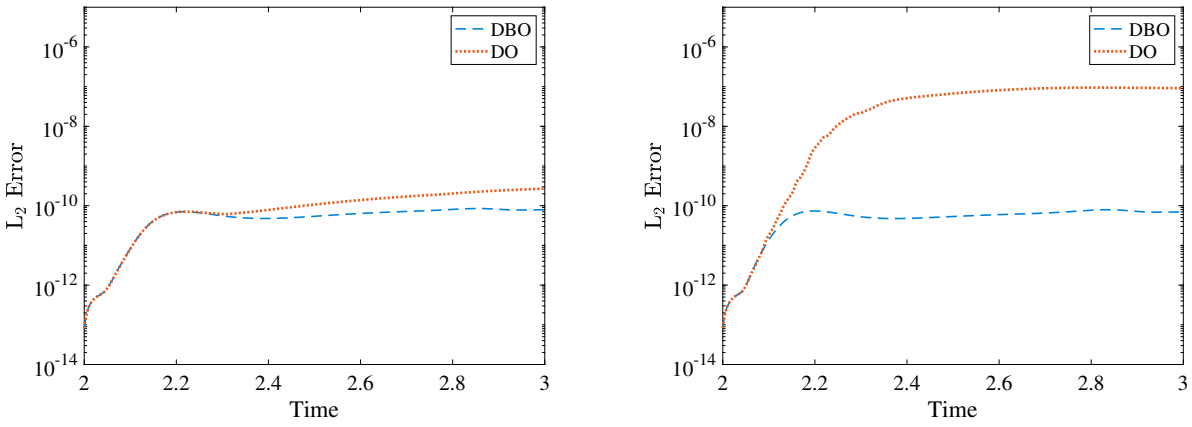

(a) Mean error for r=7

(b) Mean error for r=9

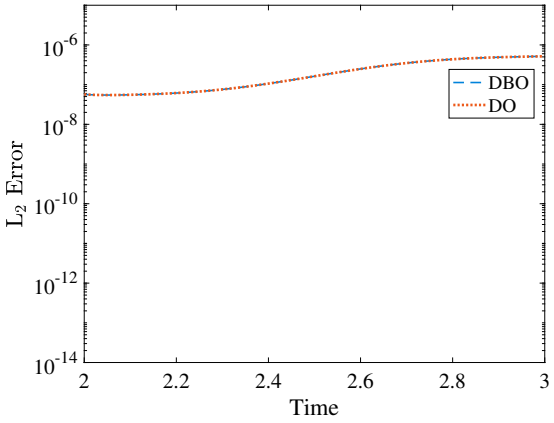

(c) Variance error for r=7

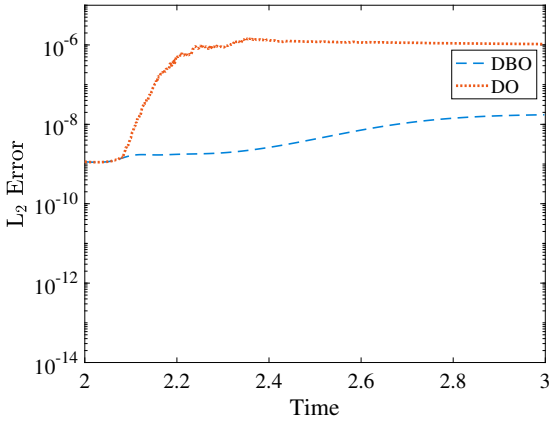

(d) Variance error for r=9

Figure 6: Burgers' equation with stochastic forcing (effect of low variance modes on the accuracy of the solution): It is observed that effectively resolving the modes with lower variance improves the numerical accuracy of the solution. The DO method fails to resolve the lower eigenvalues and hence the error for DO is higher than that of the DBO method.

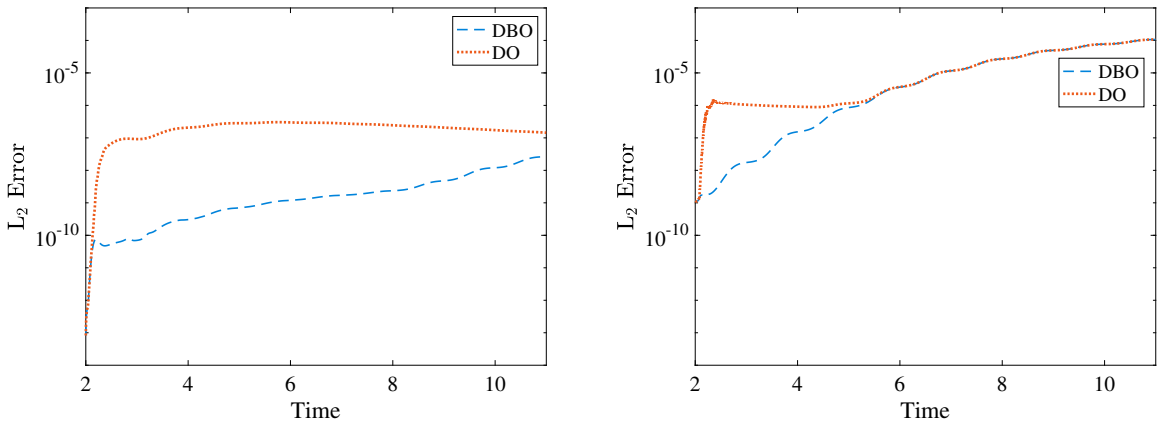

(a) Mean error (b) Variance error

Figure 7: Burgers' equation with stochastic forcing (long time integration effects): The 9 dominant modes are used to resolve the system. The mean error and variance error for DBO and DO as compared with PCM are shown in (a) and (b). It is observed that DBO performs better for short time (i.e., till 4 time units). After 4 time units the lower unresolved modes gain variance and the effect of these unresolved modes dominate the error which is equal for both DO and DBO methods.

2.8.4 1D Stochastic Burgers' Equation With 10-Dimensional Random Initial Condition

In this example, we apply the DBO decomposition to solve stochastic Burgers' equation subject to high dimensional perturbations in the initial conditions. The purpose of this example is to demonstrate that for systems that are low-dimensional when expressed in time-dependent basis, the DBO decomposition does not suffer from the curse of dimensionality. To this end we consider:

$$\frac{\partial u}{\partial t} + u\frac{\partial u}{\partial x} = \nu\frac{\partial^2 u}{\partial x^2}, \qquad x \in [0, 2\pi] \quad \text{and} \quad t \in [0, t_f],$$

where, $\nu = 0.05$. The mean for the initial condition is taken to be:

$$g(x) = 0.5(\exp(\cos(x)) - 1.5)\sin(x + 2\pi \cdot 0.37). \tag{2.20}$$

The velocity field at $t = 0$ is given by;

$$u(x, 0; \omega) = g(x) + \sum_{n=1}^{d} \sigma \frac{\sin(nx)}{n\sqrt{\pi}}\xi_n, \tag{2.21}$$

where $\sigma = 0.5$ and $\xi_n \sim \mathcal{U}[-1, 1]$ is a uniform random variable in each direction in the random space. The total dimension of the random space is given by $d = 10$. The random samples are obtained from the ME-PCM code for high dimensional anchored ANOVA [16, 11, 12]. These samples are used to solve the SODE for the evolution of the stochastic coefficients. We use the Fourier spectral method to discretize the space with $N_s = 128$. The third-order Runge-Kutta scheme is used for evolving the discrete system in time with $\Delta t = 10^{-3}$. This case is used to study the effect of high dimensional random space on the solution of the system. We also study the convergence properties of the solution as the number of modes is increased as well as the convergence properties of the solution with the increase in the number of samples in the random space.

We investigate the convergence of the DBO low-rank approximation by increasing the size of the reduction. In Fig.(8a), the eigenvalues for reduction sizes $r = 5, 7$ and 9 and a sample size of $N_r = 2880$ are shown. However, the most dominant modes, i.e. modes with largest eigenvalues, are accurately resolved. We observe that the accuracy of the lower

energy modes improves as the number of modes is increased. We also increase the sample size to $N_r = 11520$ and the values of the eigenvalues for the two samples sizes are compared in Fig(8b). It is clear that increasing the sample size improves the accuracy of the lower modes. In all cases considered, i.e. cases with different r and different Nr, the three most dominant modes with highest variance are captured correctly. These three modes capture more than 99% of the total variance of the system. This example demonstrates that the first three DBO modes can capture the *intrinsic dimensionality* of this problem in the presence of a 10-dimensional random input space.

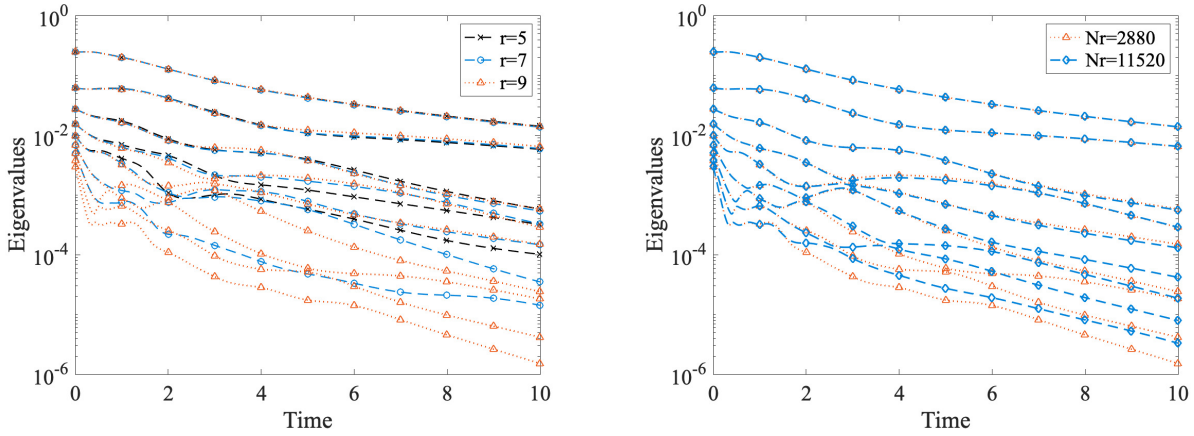

(a) Convergence for increased modes

(b) Convergence for increased samples

Figure 8: Burgers' equation with high dimensional stochastic forcing: (a) Convergence of the eigenvalues as the number of modes is increased keeping the sample size ($N_r = 2880$) same. (b) Convergence of eigenvalues for $N_r = 2880$ and $N_r = 11520$ keeping the number of modes ($r = 9$) same.

2.8.5 2D Stochastic Incompressible Navier-Stokes: Flow Over a Bump

In this example, we apply the DO and DBO decompositions to solve stochastic incompressible Navier-Stokes equations. The governing equations are given by:

$$\frac{\partial \mathbf{u}}{\partial t} + (\mathbf{u} \cdot \nabla)\,\mathbf{u} = -\frac{1}{\rho}\nabla p + \nu \nabla^2 \mathbf{u} + \mathbf{f}, \tag{2.22a}$$

$$\nabla \cdot \mathbf{u} = 0. \tag{2.22b}$$

where: $\mathbf{u} = (u_x, u_y)$ is the velocity vector field, $\mathbf{f} = (f_x, f_y) = (1, 0)$ is the forcing and p is the pressure field. We solve the flow over a bump in a channel as shown in Fig.(9a), where flow is from left to right. Periodic boundary condition is imposed in the streamwise direction and no-slip boundary condition is imposed at the bottom and top walls. We consider $\nu = 0.04$ and $\rho = 1$ and the Reynolds number is based on the channel height and time-averaged centerline horizontal velocity which is roughly equal to $Re = 1500$. For these parameters the flow is not chaotic, but it is time dependent due to constant shedding of separated region behind the bump. The stochasticity is introduced in the flow via random initial conditions given by the following equation:

$$\mathbf{u}(x, y, 0; \omega) = \mathbf{u}_0(x, y) + \sum_{i=1}^{d} \sigma \xi_i(\omega) \mathbf{\Phi}_i(x, y), \tag{2.23}$$

where $\mathbf{u}_0(x, y)$ is the solution of a deterministic simulation at $t = 50$. The deterministic solution at this time has reached the statistically steady state. The spectral element solver Nektar is used for the simulations. In the above initial condition $\mathbf{\Phi}_i = (\Phi_{x_i}, \Phi_{y_i})$ are the proper orthogonal decomposition (POD) modes obtained from the deterministic simulation of the flow over a bump at $Re = 1500$. We consider $d = 2$ and the Φ_y component of the two corresponding POD modes are shown in Fig.(9b-9c). For the spatial discretization of the mean flow and the spatial basis, we use spectral/hp element solver method with quadrilateral elements for $N_e = 1451$ and polynomial order 5. The spectral element mesh is shown in Fig.(9a). A first-order time-splitting scheme is used for the evolution of mean and the spatial basis, in which the nonlinear terms are treated explicitly and the diffusion terms are treated implicitly. The time-integration step of $\Delta t = 10^{-4}$ is used. The random space is two-dimensional and discretization of the stochastic coefficients in the random space is performed using ME-PCM with 4 elements in each random direction and 4 quadrature points in each element. Therefore, the total number of quadrature points in every direction of the random space is 16 and hence, the total number of quadrature points in the two dimensional random space is $N_r = 16^2 = 256$. We solved both DO and DBO systems with

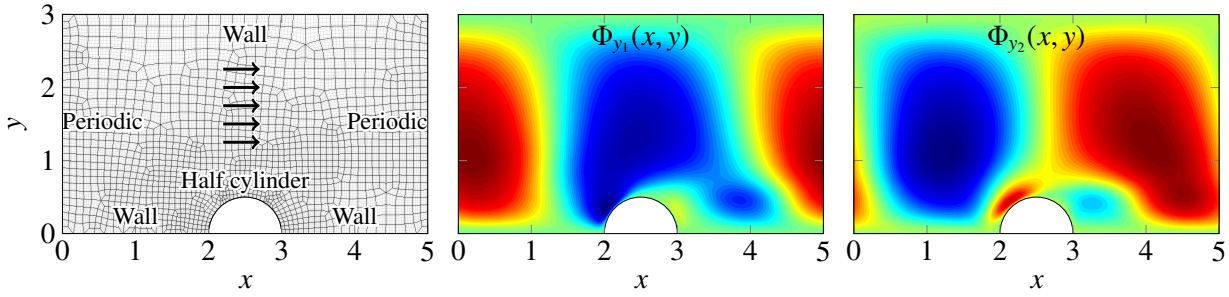

(a) Schematic of the flow (b) First POD mode: $\Phi_{y_1}(x,y)$ (c) First POD mode: $\Phi_{y_2}(x,y)$

Figure 9: Flow over a bump in a channel flow: (a) The schematic of the problem and the mesh for the spectral/hp element. (b) and (c) The y-velocity component of the two dominant POD modes.

identical discretization schemes as described above till $t_f = 5$, which amounts to 20 flow through periods.

To compare the performance of DO and DBO we performed simulations for two reduction sizes: $r = 2$ and $r = 3$. For the reference solution, we performed 256 non-intrusive direct numerical simulation (DNS) at the same ME-PCM quadrature points. We then performed KL decomposition of the 256 sample at each time step. The eigenvalues of the covariance matrix of DO, DBO for the case of $r = 2$ and the two largest KL eigenvalues are shown in Fig.(10a). It is clear that both methods perform well and match the two most energetic KL modes, although the eigenvalues of DBO are more accurate than that of the DO.

In the case of $r = 3$, the eigenvalue associated with the third mode has very small values. In fact at $t = 0$ the third eigenvalue is zero. This eigenvalue gradually grows due to nonlinearity of Navier-Stokes equations. To avoid an exact singularity, the DO and DBO simulations for $r = 3$ are initialized at $t = 1$ from the solution of the corresponding KL decomposition. The system is ill-conditioned for $r = 3$ due to the low variance of the third mode. At $t = 1$, the third eigenvalue is roughly equal to 10^{-10} as shown in Fig.(10b). The third eigenvalue of the DO decomposition deviates from the truth due to the near singularity and it eventually leads to the divergence of the DO system, while DBO performs accurately

and all three eigenvalues match those of the KL.

Fig.(11) shows evolution of the u_y of the mean and three dominant spatial modes of the DBO and KL system at $t = 1, 2$ and 3. By visual comparison we can observe that the KL and DBO modes are similar at every time step. Mode 1 and 2 of the system are the POD modes we have used as an initialization for the stochastic random conditions, convected through the channel by the mean velocity, $\bar{u}_x(x, y, t)$ of the flow. It is necessary to consider the lower eigenvalues into the flow field as we observe that overtime the lower eigenvalues can gain energy and alter the system dynamics.

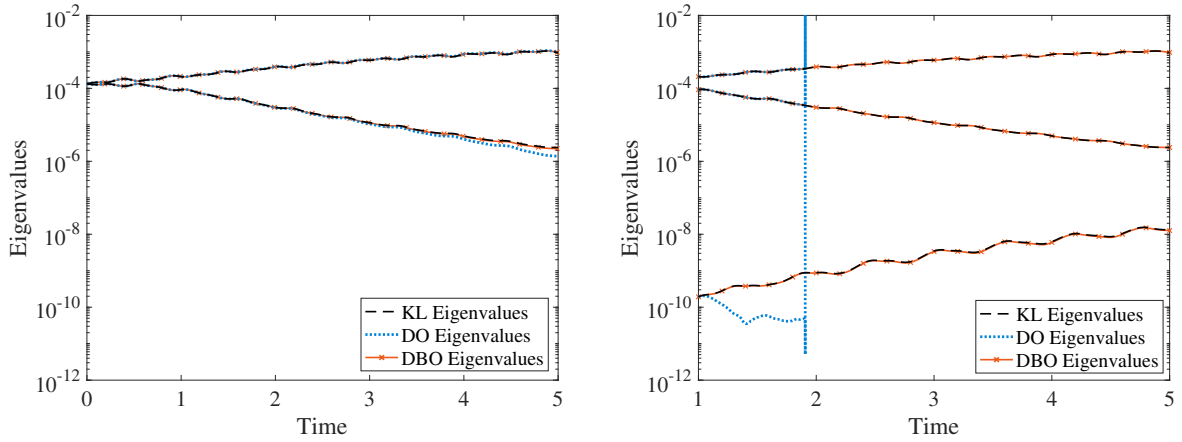

(a) Reduction size $r = 2$

(b) Reduction size $r = 3$

Figure 10: Flow over a bump in a channel: A comparison between eigenvalues for two reduction orders $r = 2, 3$ between KL, DO and DBO. For $r = 3$, it is observed that the DO method is not able to resolve lower modes when the condition number for inverting the covariance matrix is high and it eventually diverges, whereas the DBO does not have the aforementioned issue due to a better condition number for Σ inversion hence can resolve low variance modes with better accuracy.

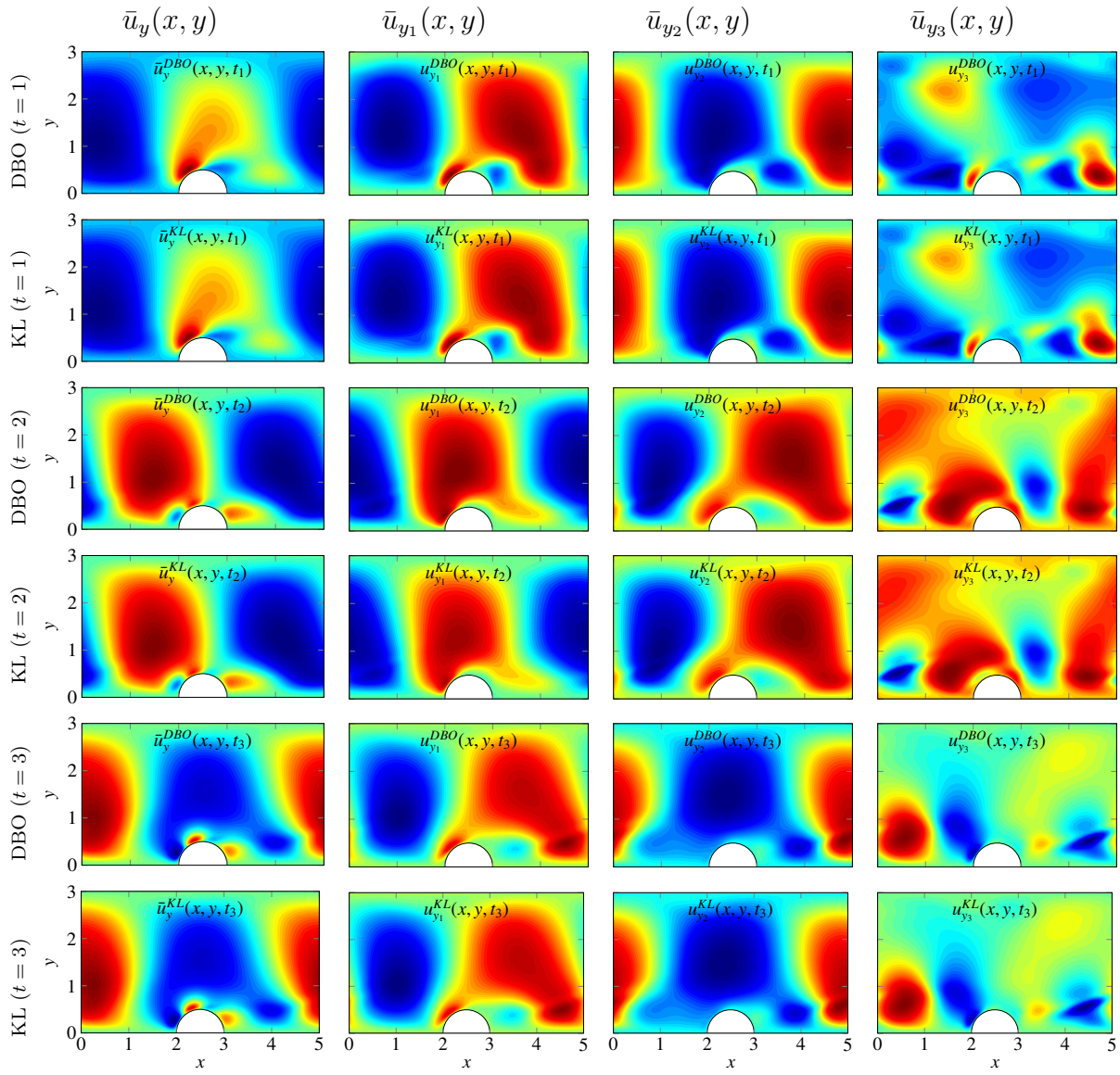

Figure 11: Flow over a bump in a channel flow: The spatial modes of DBO and KL for the stochastic flow in a channel with bump are visualized for comparison in the figure above. Column 1: The $\bar{u}_y(x,t)$ for different time instants. Column 2, 3 & 4: The three dominant spatial modes for the DBO and KL simulation. Rows 1 and 2 correspond to the DBO and KL spatial modes for $t = 1$ respectively. Rows 3 and 4 correspond to the DBO and KL spatial modes at $t = 2$ respectively. Finally, rows 5 and 6 correspond to the DBO and KL spatial modes at $t = 3$ respectively.

3.0 DBO Formulation for Random Boundary Conditions

The focus of this chapter is to formulate a method to solve linear and nonlinear partial differential equations imposed with stochastic boundary conditions. The main challenge in solving problems with stochastic boundaries lies in the determining how the value of the stochastic function at the boundary will be distributed across spatial modes whilst maintaining orthonormality condition of the spatial modes. The DO method [1] introduced equations to solve for stochastic boundary equations given by:

$$\mathcal{B}[u_i(\xi,t)]|_{\xi\in\partial D} = \mathbb{E}\left[Y_j(t;\omega)h(\xi,t;\omega)\right] C^{-1}_{Y_i(t;\omega)Y_j(t;\omega)},$$

where C represents the covariance matrix. The boundary modes consist of projecting the Dirichlet boundary condition on the stochastic modes at each time step. Another method called the dual Dynamically Orthogonal (or dual-DO) [45] was recently introduced for the imposition of the stochastic Dirichlet boundary conditions using the dynamical low rank (DLR) variational principle.

In this chapter, we look at the variational principle approach to derive the evolution equations for the stochastic and spatial modes for the DBO method.A few demonstration cases are considered to evaluate the numerical performance of the method. We first apply the DBO equations for the stochastic linear advection-diffusion equation. For this case, we apply three different boundary conditions: Dirichlet, Neumann and Robin. We further apply stochastic boundary to the Burgers' equation. The evolution of the singular values, boundary errors and global errors are evaluated. We then consider a two dimensional domain with a jet impingement. The stochastic boundary is considered for the temperature equation. The propagation of uncertainty in the domain is studied for this problem for two cases: a) constant Prandtl number b) temperature dependent Prandtl number.

3.1 Variational Principle

Let the Dynamically Bi-Orthonormal decomposition defined in [46] to denote a random field be written as:

$$\Phi(x,t;\omega) = \sum_{i=1}^{r}\sum_{j=1}^{r} u_i(x,t)\Sigma_{ij}(t)y_j(t;\omega) + e(x,t;\omega), \tag{3.1}$$

where $u_i(x,t), i = 1,2,\cdots,r$ are the spatial modes, $y_j(t;\omega), j = 1,2,\cdots,r$ are the stochastic modes and $\Sigma_{ij}(t)$ is the factorization of the covariance matrix.

Note: The decomposition considered here is different from the decomposition in [46], in the sense that the mean is not subtracted from the solution.

We consider the following stochastic partial differential equation (SPDE), which defines the system evolution:

$$\frac{\partial u(x,t;\omega)}{\partial t} = \mathcal{N}(u(x,t;\omega)) \qquad x \in D, \omega \in \Omega, \tag{3.2}$$

$$au(x,t;\omega) + b\frac{\partial u(x,t;\omega)}{\partial n} = g(u(x,t;\omega)) \qquad x \in \partial D, \omega \in \Omega, \tag{3.3}$$

$$u(x,t_0;\omega) = u_0(x;\omega) \qquad x \in D, \omega \in \Omega, \tag{3.4}$$

where $\mathcal{N}$ is in general, a nonlinear differential operator, D denotes the interior domain and ∂D denotes the boundary and $\overline{D} = D \cup \partial D$. Our strategy to determine the boundary conditions for the spatial modes is based on the realization that the DBO evolution equations are the optimality conditions of a variational principle. An analogous variational principle was recently introduced in [47] for the reduced order modeling of deterministic reactive species transport equation. Our approach is to define a *unified* evolutionary differential operator that encompasses both the interior domain as well as the boundary as shown below:

$$\mathcal{M}(u(x,t;\omega)) = \begin{cases} \mathcal{N}(u(x,t;\omega)), & \text{if } x \in D, \quad \omega \in \Omega, \\ \mathcal{B}(u(x,t;\omega)), & \text{if } x \in \partial D, \quad \omega \in \Omega. \end{cases}$$

where $\mathcal{B}(u(x,t;\omega)) = \dfrac{\partial}{\partial t}\left[\dfrac{g(u)}{a} - \dfrac{b}{a}\dfrac{\partial u}{\partial n}\right]$. Here, we consider the Dirichlet and Robin boundary conditions, i.e., $b = 0, a \neq 0$ and $b \neq 0, a \neq 0$ respectively. For the special case of

Neumann boundary condition see Remark 3.1.3. The variational principle for stochastic DBO seeks to minimize the following functional:

$$\mathcal{F}(\dot{U}(x,t),\dot{\Sigma}(t),\dot{Y}(t)) = \left\| \frac{\partial}{\partial t}(u_i(x,t)\Sigma_{ij}(t)y_j^T(t)) - \mathcal{M}(u) \right\|_{\mathcal{F}}^2, \quad x \in \overline{D}, \tag{3.5}$$

subject to the orthonormality of the spatial and stochastic bases i.e., $\langle u_i(x,t), u_j(x,t)\rangle = \delta_{ij}$ and $\mathbb{E}[y_i(t)y_j(t)] = \delta_{ij}$. For the sake of brevity, in the rest of this section $u_i(x,t)$ is denoted as u_i, $y_i(t)$ is denoted as y_i, $\Sigma_{ij}(t)$ is denoted as Σ_{ij} and $\mathcal{M}(u)$ is denoted as $\mathcal{M}$. Here, $\mathcal{M} \in \mathbb{R}^{\infty \times s}$ is a quasimatrix, where s represents the number of discrete samples in the random space. Taking time derivative of these constraints, we obtain the dynamic orthogonality of the modes given by,

$$\langle \dot{u}_i, u_j \rangle = \Phi_{ij},$$
$$\mathbb{E}[\dot{y}_i y_j] = \Psi_{ij},$$

where Φ and Ψ are skew-symmetric matrices i.e., $\Phi_{ij} = -\Phi_{ji}$ and $\Psi_{ij} = -\Psi_{ji}$. Incorporating the orthonormality constraints using Lagrange multipliers in the functional (3.5) results in:

$$\mathcal{G}(\dot{U},\dot{\Sigma},\dot{Y}) \;=\; \left\| \frac{\partial}{\partial t}(u_i\Sigma_{ij}y_j^T) - \mathcal{M} \right\|_{\mathcal{F}}^2 + \lambda_{1_{ij}}\left(\langle \dot{u}_i, u_j\rangle - \Phi_{ij}\right) + \lambda_{2_{ij}}\left(\mathbb{E}[\dot{y}_i y_j] - \Psi_{ij}\right), \tag{3.6}$$

where $\lambda_{1_{ij}}(t)$, $\lambda_{2_{ij}}(t)$,$i,j = 1,\ldots,r$ are Lagrangian multipliers. It is shown in [47], that any choice of the skew-symmetric matrices Φ and Ψ lead to equivalent decompositions which correspond to an in-subspace rotation. The equations for the subsequent theorem, are derived by taking $\Phi = \Psi = 0$

Theorem 3.1.1. *Let Eq.(3.1) represent the DBO decomposition of the solution of SPDEs given in Eq.(3.2-3.4). Then using the variational principle in Eq.(3.6) and first order optimality conditions the evolution equations of spatial modes, stochastic modes and the factorization of the variance for DBO are given by:*

$$\frac{\partial u_i}{\partial t} = \left[\mathbb{E}[\mathcal{N}y_j] - u_k\langle u_k, \mathbb{E}[\mathcal{M}y_j]\rangle\right]\Sigma_{ij}^{-1}, \quad x \in D, \tag{3.7}$$
$$\frac{\partial u_i}{\partial t} = \left[\mathbb{E}[\mathcal{B}y_j] - u_k\langle u_k, \mathbb{E}[\mathcal{M}y_j]\rangle\right]\Sigma_{ij}^{-1}, \quad x \in \partial D, \tag{3.8}$$
$$\frac{dy_i}{dt} = \left[\langle \mathcal{M}, u_j\rangle - y_k\mathbb{E}[y_k\langle \mathcal{M}, u_j\rangle]\right]\Sigma_{ji}^{-1}, \tag{3.9}$$
$$\frac{d\Sigma_{ij}}{dt} = \langle u_i, \mathbb{E}[\mathcal{M}y_j]\rangle\,. \tag{3.10}$$

The proof of the above theorem is given in Appendix D.

Remark 3.1.1. *Although the evolution equations in Theorem 3.1.1 have been derived without subtracting the mean from the stochastic field, the variational principle can be easily extended to mean subtracted form of equations.*

Remark 3.1.2. *Similar variational principles for the DO and BO modes can be obtained by changing the constraints on the spatial and stochastic modes in the variational principle. The variational principle for DO formulation as given in [33], leads to the following equations for evolution of spatial and stochastic modes:*

$$\frac{\partial u_i}{\partial t} = \left[\mathbb{E}[\mathcal{N} y_j] - u_k \left\langle u_k, \mathbb{E}[\mathcal{M} y_j] \right\rangle\right] C_{ij}^{-1}, \quad x \in D, \tag{3.11}$$

$$\frac{\partial u_i}{\partial t} = \left[\mathbb{E}[\mathcal{B} y_j] - u_k \left\langle u_k, \mathbb{E}[\mathcal{M} y_j] \right\rangle\right] C_{ij}^{-1}, \quad x \in \partial D, \tag{3.12}$$

$$\frac{dy_i}{dt} = \left\langle \mathcal{M}, u_i \right\rangle. \tag{3.13}$$

Remark 3.1.3. *For the Neumann boundary condition, i.e., when $a = 0$, we get $\dfrac{\partial g(u)}{\partial t} = b\dfrac{\partial}{\partial t}\left[\dfrac{\partial u}{\partial n}\right]$. This boundary condition is enforced by obtaining a discrete equivalent form of the derivative at the boundary and using this discrete nodal equation to determine the value at the boundary point.*

3.2 Demonstration cases

3.2.1 Linear Advection-Diffusion Equation

As the first demonstration, we consider a linear advection-diffusion equation governed by:

$$\frac{\partial u}{\partial t} + c\frac{\partial u}{\partial x} = \nu \frac{\partial^2 u}{\partial x^2}, \qquad x \in [0,5] \text{ and } t \in [0, t_f], \tag{3.14}$$

$$u(x,0;\omega) = \cos(2\pi x) + \sum_{i=1}^{d} \sigma_x \sqrt{\lambda_{x_i}} u_i(x) \xi_i, \qquad x \in [0,5], \xi_i \sim \mathcal{U}[-1,1], \tag{3.15}$$

$$au + b\frac{\partial u}{\partial n} = g(u), \qquad x = 0, \tag{3.16}$$

$$\frac{\partial u}{\partial x} = 0, \qquad x = 5. \tag{3.17}$$

Here, ν is taken to be 0.05 and $c = 1$. Neumann boundary condition is imposed at $x = 5$. The randomness in the system comes from the stochastic left boundary ($x = 0$) and random initial conditions. We consider three types of stochastic boundaries at $x = 0$: (i) Dirichlet boundary, ($b = 0, a \neq 0$) (ii) Neumann boundary ($a = 0, b \neq 0$) and (iii) Robin boundary ($a \neq 0, b \neq 0$). The results for these cases are presented in the subsequent sections.

The SPDE given by Eq.(3.14-3.17) is solved using two methods: (i) DBO method according to Eq.(3.7-3.10), (ii) DO method according to Eq.(3.11-3.13) and (iii) KL decomposition obtained from the solutions of all samples. For spatial discretization of the domain, the spectral/hp element method is used with $N_e = 101$ and polynomial order 4. Uniform distribution is taken in all directions of the random space and the space is discretized using Multi-Element Probabilistic Collocation Method (ME-PCM). The sparse grid construction [10, 13] is used for obtaining all the samples for random space. We use $d = 8$, $level(k) = 3$ and 1 element per random dimension which gives the total samples $s = 333$. The same samples are used for all the three cases of boundaries in the linear advection-diffusion equation. The Karhunen Loéve (KL) decomposition is used to obtain the spatial, stochastic modes and eigenvalues from the solution of all samples obtained from ME-PCM. The DBO and DO solutions are compared with the KL solution and the global error between the two fields is defined as,

$$e_g(x,t;\omega) = u_{DBO}(x,t;\omega) - u_{KL}(x,t;\omega), \tag{3.18}$$

$$\mathcal{E}_g = \mathbb{E}\left[\langle e_g(x,t;\omega), e_g(x,t;\omega)\rangle\right]. \tag{3.19}$$

Similarly, the boundary error is computed as,

$$e_b(x|_{\partial D}, t;\omega) = u_{DBO}(x|_{\partial D}, t;\omega) - \left[\frac{g(u(x,t;\omega))}{a} - \frac{b}{a}\frac{\partial u(x,t;\omega)}{\partial n}\right], \tag{3.20}$$

$$\mathcal{E}_b = \mathbb{E}\left[\langle e_b(x|_{\partial D}, t;\omega),\, e_b(x|_{\partial D}, t;\omega)\rangle\right]. \tag{3.21}$$

3.2.2 Stochastic Dirichlet Boundary Condition

Dirichlet boundary condition is imposed at $x = 0$ as,

$$u(0, t; \omega) = g_1(t; \omega).$$

where $g_1(t; \omega)$ is assumed to be a random process with a squared exponential temporal kernel given by:

$$K(t, t') = \exp\left(\frac{-(t - t')^2}{2l_t^2}\right),$$

where, l_t is the temporal correlation length, which is taken to be 1.0. The eigen-decomposition of the above kernel results in:

$$\int_0^{t_f} K(t, t')\varphi_i(t')dt' = \lambda_{t_i}\varphi_i(t),$$

where $\varphi_i(t)$ and λ_{t_i} are the eigenfunctions and eigenvalues of the temporal kernel respectively. The boundary condition is approximated with a a truncated Karhunen-Loéve decomposition as given in the following equation:

$$g_1(t; \omega) = 0.5\cos(2\pi t) + \sigma_t \sum_{i=1}^{d} \sqrt{\lambda_{t_i}}\varphi_i(t)\xi_i.$$

Here, ξ_i are the discrete points in a d-dimensional random space obtained by using ME-PCM sparse grid construction. For this case, $d = 8$ is taken as this approximation captures 99.99% of the random process. σ_t is taken to be 1.0. Similarly to initialize the stochastic initial conditions, we take a squared exponential kernel in the spatial domain,

$$K(x, x') = \exp\left(\frac{-(x - x')^2}{2l_x^2}\right),$$

where, l_x is the spatial correlation length which is taken to be 1.0.

$$\int_{x_l}^{x_r} K(x, x')\psi_i(x')dx' = \lambda_{x_i}\psi_i(x),$$

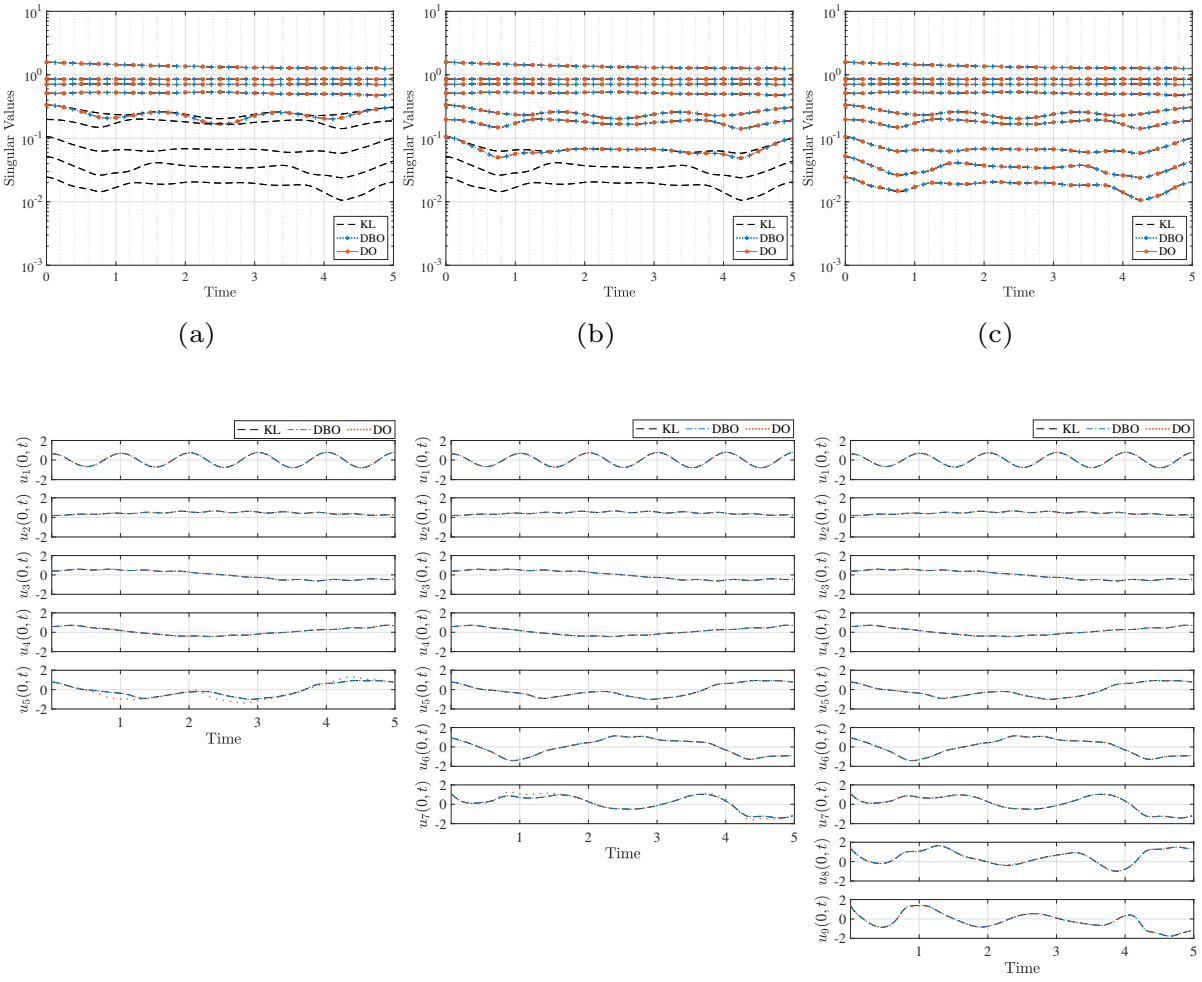

Figure 12: Linear advection-diffusion equation (i) Dirichlet boundary condition: The first row shows the singular value comparison for KL, DBO and DO methods. The values are compared for three model reduction orders, $r = 5, 7$ & 9. The evolution of the values of the modes at the stochastic left boundary are compared in the second row for the three aforementioned methods.

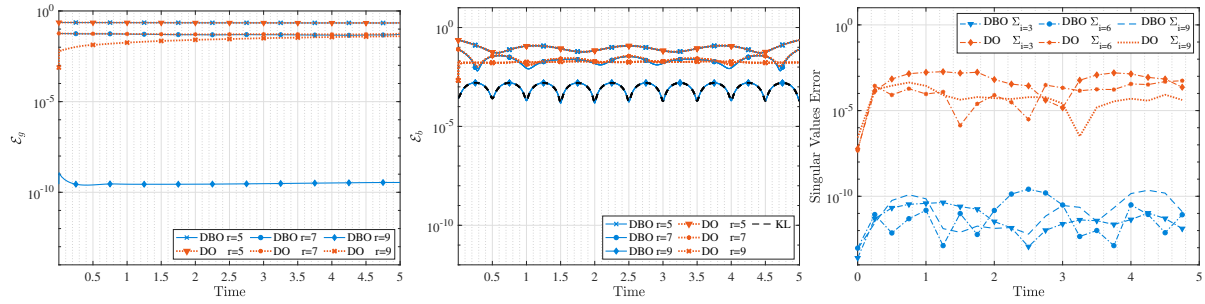

(a) Global Error (b) Boundary Error (c) Singular Values Error

Figure 13: Linear advection-diffusion equation (i) Dirichlet boundary condition: The global and boundary error comparison is shown in (a) and (b) respectively. The lowest error is obtained using DBO method for $r = 9$. The singular values obtained from DO method for $r = 9$ are riddled with errors. The L_2-error for the third, sixth and ninth singular values is compared in (c) for DO and DBO.

where $\psi_i(t)$ and λ_{x_i} are the eigenfunctions and eigenvalues of the spatial kernel and $x_l = 0, x_r = 5$ are the left and right boundaries of the spatial domain respectively. The initial conditions are taken to be,

$$u(x, 0; \omega) = 0.5 \cos(2\pi x) + \sigma_x \sum_{i=1}^{d} \sqrt{\lambda_{x_i}} \psi_i(x) \xi_i.$$

We take $\sigma_x = 1.0$. The fourth-order Runge-Kutta method is used for time integration with $\Delta t = 5 \times 10^{-4}$. The system is numerically evolved till $t_f = 5$ using the three methods: (i) DBO, (ii) DO and (iii) KL. The obtained results are compared and presented in Fig.(12-13). The first row of Fig.(12) shows the comparison of singular values for three different orders of model reduction, $r = 5, 7$ & 9 for DBO, DO and KL. We observe that the singular values improve in comparison as the order of model reduction is improved. The second row shows the comparison of the value of the modes at the stochastic Dirichlet boundary i.e., $x = 0$. The solution is exactly represented by $r = 9$. Hence, for the lower model reduction orders i.e., $r = 5$ and 7, the last mode of DBO and DO solution shows noticeable differences from the KL

both in the singular values and the evolution of the modes at the boundary. The error in the solution for $r = 5, 7$ can be attributed to the unresolved modes. The error comparison for the two methods as compared to KL is shown in Fig.(13). The global error in the representation of the solution i.e., $\mathcal{E}_g$ is shown in Fig.(13a). The error at the stochastic boundary i.e., $\mathcal{E}_b$ is shown in Fig.(13b). For $r = 9$, when the solution is represented exactly, DBO and DO show the lowest errors of all model reduction order. However, between DBO and DO, DBO shows the highest accuracy for $r = 9$ whereas the DO error for the same reduction order is a few orders of magnitude higher than the DBO error. The DBO boundary error for $r = 9$ shows the same value as the KL error. We observe high error in DO for $r = 9$ despite the seemingly equal singular value comparison. The source of the error can be traced back to the error in the singular values as shown in the Fig.(13c). The errors in third, sixth and ninth singular values for the case $r = 9$ are shown. The L_2-errors are computed by comparing the DBO and DO singular values with KL values. We observe that the DO solution is riddled with error, which makes the error in solution for $r = 9$ higher than that of DBO. This can be attributed to the better condition number for matrix inversion in DBO leading to lower errors. The DO method has a condition number $\lambda_{max}/\lambda_{min}$ (where λ_{min} and λ_{max} represent the smallest and largest eigenvalues of the covariance matrix), whereas the DBO method has a condition number $\sqrt{\lambda_{max}/\lambda_{min}}$ since the factorization of the covariance matrix i.e., Σ is inverted.

3.2.3 Stochastic Neumann Boundary Condition

The stochastic Neumann boundary condition is imposed on the left boundary, $x = 0$ as,

$$\frac{\partial u(0,t;\omega)}{\partial x} = g_2(t;\omega).$$

To enforce this condition, we construct the discretized form of the boundary condition, given by:

$$\mathcal{D}_{11}u_1 + \mathcal{D}_{12}u_2 + \cdots + \mathcal{D}_{1p}u_p = g_2(t;\omega),$$
$$u_1 = \frac{g_2(t;\omega) - [\mathcal{D}_{12}u_2 + \cdots + \mathcal{D}_{1p}u_p]}{\mathcal{D}_{11}}.$$

Here, $\mathcal{D}$ represents the differentiation matrix, p represents the number of points in the element used to evaluate the derivative. Similar discretized equations can be derived for finite difference method as well. Similar to the problem setup as the Dirichlet boundary case, the function $g_2(t;\omega)$ is taken as a function of eigenvectors and singular values of the squared exponential kernel and the initial conditions are taken as a function of eigenvectors and singular values of the spatial squared exponential kernel. The temporal correlation length, l_t is taken to be 1.0 and the spatial correlation length l_x is taken to be 1.0. The boundary conditions are taken to be,

$$g_2(t;\omega) = 2\pi \sin(2\pi t) + \sigma_t \sum_{i=1}^{d} \sqrt{\lambda_{t_i}} \varphi_i(t) \xi_i,$$

and the initial conditions are taken to be,

$$u(x,0;\omega) = \cos(2\pi x) + \sigma_x \sum_{i=1}^{d} \sqrt{\lambda_{x_i}} \psi_i(x) \xi_i.$$

Here, $\sigma_t = 0.1$ and $\sigma_x = 0.5$. Similar to the Dirichlet boundary condition case, $\xi_i \in \mathcal{U}[-1,1]$ are discrete points in a 8-dimensional random space obtained by using ME-PCM. The fourth-order Runge-Kutta method is used for time integration with $\Delta t = 5 \times 10^{-4}$. The system is numerically evolved till $t_f = 5$ using the KL, DBO and DO methods. The results for the three methods are compared in Fig.(14-15). The first row in Fig.(14), shows comparison between singular values for model reduction orders, $r = 5, 7$ & 9. The singular values improve in comparison as the model reduction order is improved. The second row, shows the comparison of the value of modes at the stochastic Neumann boundary at $x = 0$. Fig.(15a-b) show the global error and boundary error comparison for the three reduction orders. Similar to the previous case, when the solution is exactly represented by $r = 9$, DBO and DO show the lowest errors of all reduction orders. Between DBO and DO, DBO shows higher accuracy for $r = 9$. This can be seen in the errors for $r = 9$ for DBO and DO in Fig.(15a-b). DBO boundary error for $r = 9$ shows the same value as the KL error. The error comparison between individual singular values is shown in Fig.(15c) for third, sixth and ninth singular values. This error in the DO solution causes the global and boundary error for $r = 9$ to be higher that of DBO error. This lower error for DBO method, can be attributed to the fact

that the DBO method has a better condition number for inversion of Σ matrix than DO method which inverts the covariance matrix.

3.2.4 Stochastic Robin Boundary Condition

The stochastic Robin boundary condition is imposed on the left boundary at $x = 0$ as,

$$au(0,t;\omega) + b\frac{\partial u(0,t;\omega)}{\partial x} = g_3(t;\omega).$$

To enforce this condition, we construct the discretized form of the boundary condition, given by:

$$au_1 + b\left[\mathcal{D}_{11}u_1 + \mathcal{D}_{12}u_2 + \cdots + \mathcal{D}_{1p}u_p\right] = g_3(t;\omega),$$
$$u_1 = \frac{g_3(t;\omega) - b\left[\mathcal{D}_{12}u_2 + \cdots + \mathcal{D}_{1p}u_p\right]}{a + bD_{11}}.$$

Here, $\mathcal{D}$ represents the differentiation matrix and p represents the number of points in the element used to compute the derivative. Similar equation can be derived for the finite difference method as well. Similar to the problem setup as the previous cases, the function $g_3(t;\omega)$ is taken as a function of eigenvectors and singular values of the squared exponential kernel and $a = 0.1, b = 1$. The temporal correlation length, l_t is taken to be 1 and the spatial correlation length l_x is taken to be 1. The boundary conditions are taken to be,

$$g_3(t;\omega) = -\cos(2\pi t) + 2\pi\sin(2\pi t) + \sigma_t\sum_{i=1}^{d}\sqrt{\lambda_{t_i}}\varphi_i(t)\xi_i,$$

and the initial conditions are taken to be,

$$u(x,0;\omega) = \cos(2\pi x) + \sigma_x\sum_{i=1}^{d}\sqrt{\lambda_{x_i}}\psi_i(x)\xi_i.$$

Similar to the Dirichlet boundary condition case, $\xi_i \in \mathcal{U}[-1,1]$ are discrete points in a 8-dimensional random space obtained by using ME-PCM. The samples are drawn from a uniform distribution. Here, $\sigma_t = -0.1$ and $\sigma_x = 0.01$. The fourth-order Runge-Kutta method is used for time integration with $\Delta t = 5\times10^{-4}$. The system is numerically evolved till $t_f = 5$ using the KL, DBO and the DO methods. The singular value evolution, evolution of modes at the boundary and error comparison for this case are shown in Fig.(16-17). The first

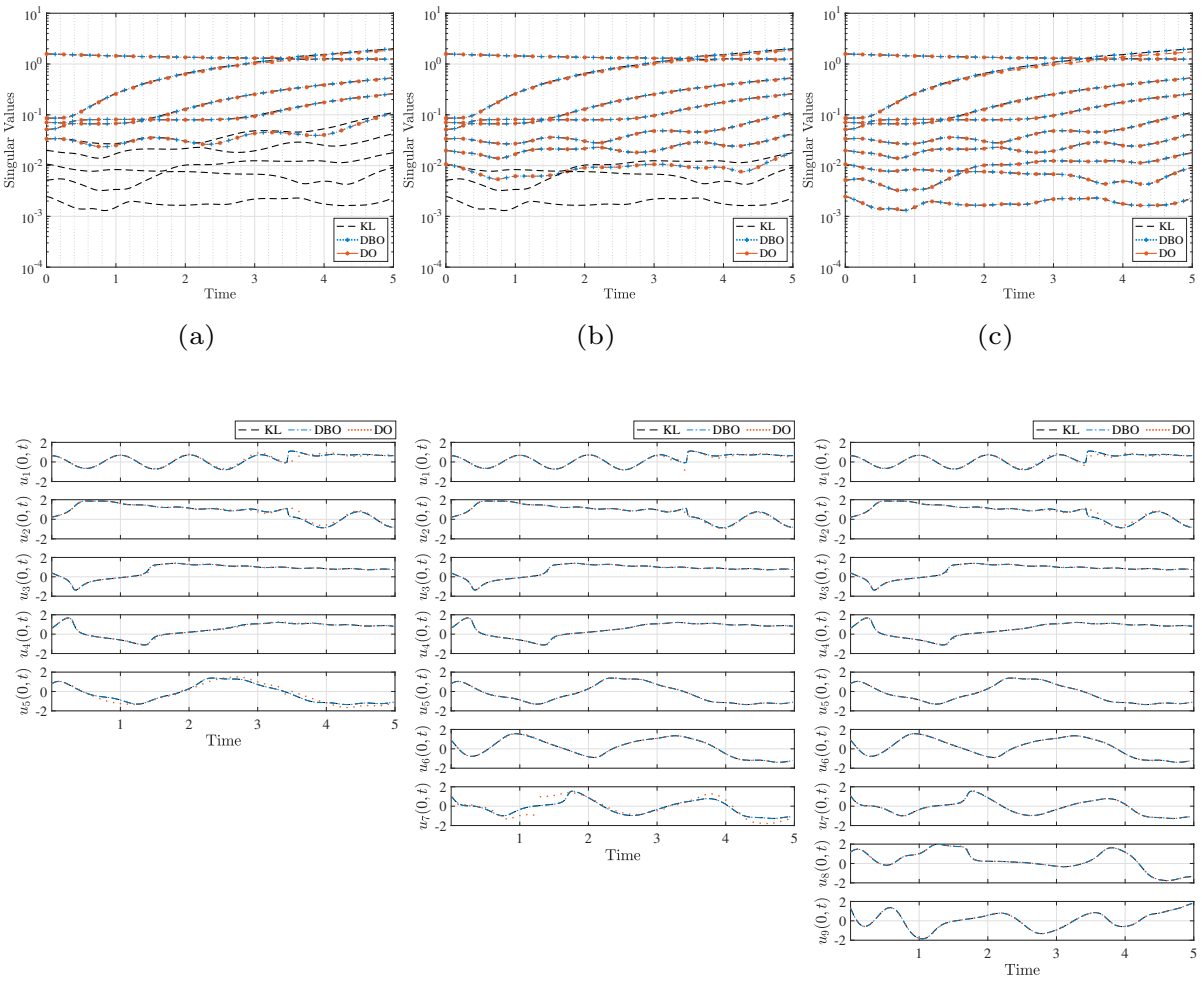

Figure 14: Linear advection-diffusion equation (ii) Neumann boundary condition: The first row shows the singular value comparison for KL, DBO and DO methods, The values are compared for three reduction orders, $r = 5, 7$ and 9. The evolution of the values of the modes at the left stochastic boundary are compared in the second row for the three methods.

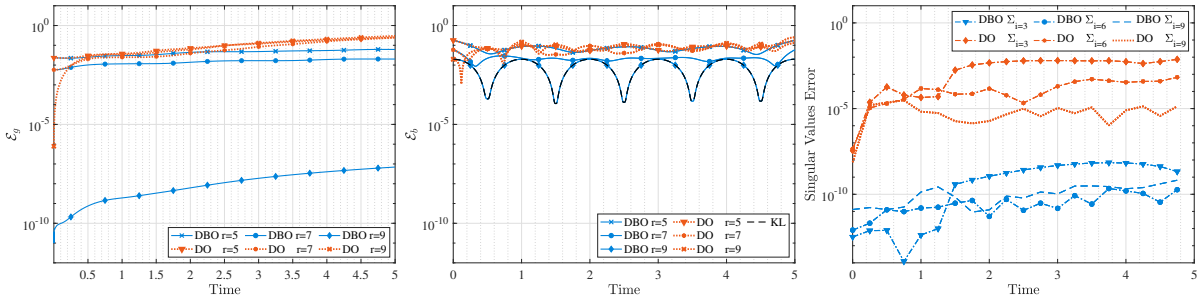

(a) Global Error (b) Boundary Error (c) Singular Values Error

Figure 15: Linear advection-diffusion equation (ii) Neumann boundary condition: Error comparison for DBO and DO as compared with the KL solution. The global error, $\mathcal{E}_g$ and the boundary error, $\mathcal{E}_b$ are shown in (a) and (b) respectively. The lowest error is obtained using DBO method for $r = 9$. The L_2-error in the third, sixth and ninth singular value is compared in (c) for DO and DBO.

row in Fig.(16), shows comparison between singular values for the model reduction orders, $r = 5, 7\& \ 9$. The singular values improve in comparison as the model reduction order is improved. The second row, shows the comparison of the modes at the stochastic boundary $x = 0$. Fig.(17a-b) show the global and boundary error comparison for the three reduction orders. Similar to the previous case, when the solution is exactly represented by $r = 9$ for DBO and DO, show the lowest errors of all reduction orders. Between DBO and DO, DBO shows higher accuracy for $r = 9$. This can be seen in the errors for $r = 9$ for DBO and DO in Fig.(17a-b). The boundary error for $r = 9$ for DBO shows the same error as the KL. The error comparison between individual singular values is shown in Fig.(17c) for third, sixth and ninth singular values for the case $r = 9$. This error in the individual singular values in the DO solution causes the global and boundary error for $r = 9$ to be higher than that of DBO error.

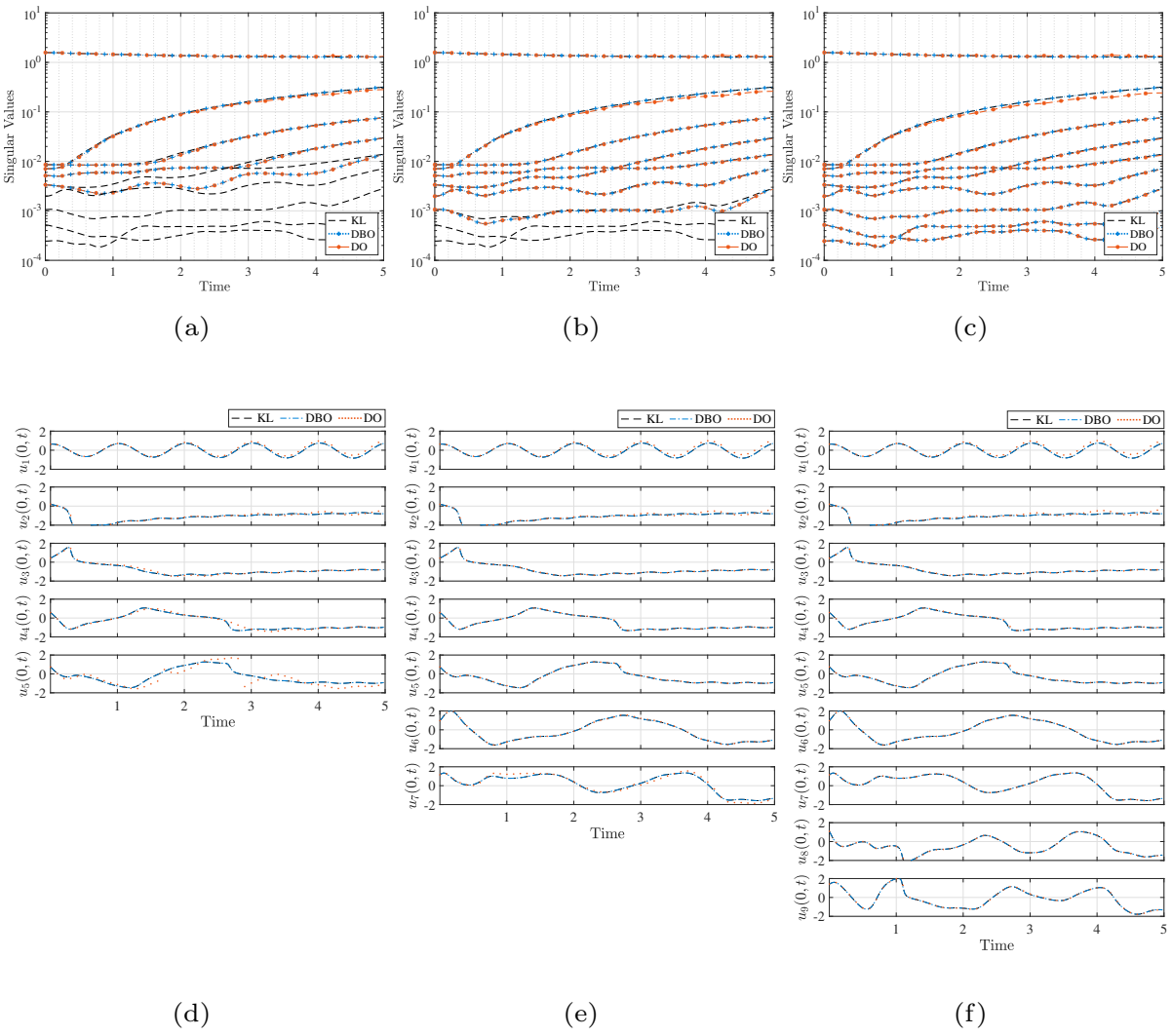

Figure 16: Linear advection-diffusion equation (iii) Robin boundary condition: The first row shows the singular value comparison for KL, DBO and DO methods. The values are compared for three reduction orders, $r = 5, 7$ & 9. The evolution of the values of the modes at the left stochastic boundary are compared in the second row for the three methods.

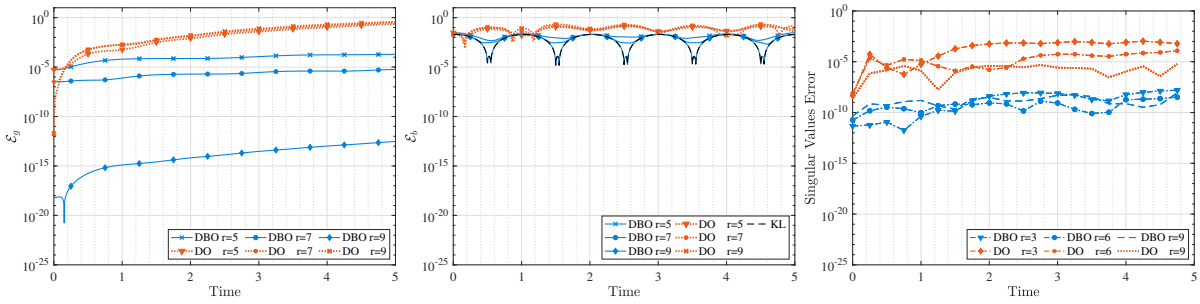

(a) Global Error (b) Boundary Error (c) Singular Values Error

Figure 17: Linear advection-diffusion equation (iii) Robin boundary condition: Error comparison for DBO and DO as compared with the KL solution. The global and boundary error comparison are shown in (a) and (b) respectively. Lowest error is obtained using DBO method for $r = 9$. L_2-error in the third, sixth and ninth singular value is compared in (c) for DO and DBO.

3.2.5 Burgers' Equation

As a demonstration for the nonlinear one-dimensional equation, we consider the Burgers' equation governed by:

$$\frac{\partial u}{\partial t} + u\frac{\partial u}{\partial x} = \nu\frac{\partial^2 u}{\partial x^2}, \qquad x \in [0,1] \text{ and } t \in [0, t_f], \tag{3.22}$$

$$u(x,0;\omega) = \sin(2\pi x) + \sigma_x \sum_{i=1}^{d} \sqrt{\lambda_{x_i}}\psi_i(x)\xi_i, \qquad x \in [0,1], \tag{3.23}$$

with Dirichlet boundary condition at $x = 0$ and Neumann boundary condition at $x = 1$. Here, ν is taken to be 0.05. We impose random Dirichlet stochastic boundary at $x = 0$ given by,

$$u(0,t;\omega) = g_4(t;\omega).$$

Similar to the problem setup as the previous cases, the random process $g_4(t;\omega)$ is taken as a function of the eigenvectors and singular values of the squared exponential kernel. The

temporal correlation length is taken to be 3. The boundary conditions are taken to be,

$$g_4(t;\omega) = -\sin(2\pi t) + \sigma_t \sum_{i=1}^{d} \sqrt{\lambda_{t_i}} \varphi_i(t) \xi_i.$$

Here, $\sigma_t = 0.01$. The eigenvectors and eigenvalues of the spatial squared exponential kernel are used to determine the random initial conditions. The spatial correlation length, l_x is taken to be 3. The initial conditions are given by,

$$u(x,0;\omega) = \sin(2\pi x) + \sigma_x \sum_{i=1}^{d} \sqrt{\lambda_{x_i}} \psi_i(x) \xi_i.$$

The random space is taken to be $d = 4$ dimensional and $\sigma_x = 0.005$. For spatial discretization of the domain, the spectral/hp element method is used with $N_e = 101$ and polynomial order 4. The 4 dimensional random space is discretized with the ME-PCM tensor product rule [12, 48] with 1 element each containing 4 points in each random direction which give the total samples to be $s = 4^4 = 256$. The fourth-order Runge-Kutta method is used for time integration with $\Delta t = 2.5 \times 10^{-4}$. We use the technique of switching time at $t_s = 0.3$ to initialize the spatial and stochastic modes. Although the switching time is used in cases where the initial conditions are deterministic, in this case for $r = 8$, the singular values for $r > 6$ have negligible values and give rise to computational issues for inversion of the Σ matrix. The system is evolved till $t_s = 0.3$ using PCM method to let the lower eigenvalues gain energy. The computed KL modes and eigenvalues are used to initialize the DBO and DO spatial and stochastic modes at this time step. The system is then numerically evolved till $t_f = 5$ using the KL, DBO and DO methods. The results for three reduction orders $r = 4, 6$ & 8 are shown in Fig.(18-19). The comparison of singular values is shown in first row of Fig.(18). The evolution of the modes at the stochastic boundary is shown in the second row of Fig.(18). For lower reduction orders, i.e., $r = 4, 6$, the singular values and the evolution of the boundary modes show deviation from the KL solution. This error can be attributed to the unresolved modes in the solution. Although the random dimension is 4, the system cannot be exactly represented by 5 modes, due to the non-linearity of the equation. The global and boundary error in the solution are shown in Fig.(19a-b). We observe that as the model reduction order is increased the error reduces for both DO and DBO. Since the

solution cannot be represented exactly for $r = 8$, the KL and DBO show discrepancy in the boundary error as seen in Fig.(19b).

3.2.6 2D Linear Advection-Diffusion Equation

The effect of stochastic boundary conditions is further demonstrated on a two dimensional physical domain. We consider the linear advection-diffusion equation governed by:

$$\frac{\partial T}{\partial t} + (\mathbf{v} \cdot \nabla)T = \frac{1}{RePr}\nabla^2 T. \tag{3.24}$$

The velocity field $\mathbf{v} = (u, v)$ is obtained by solving the 2D incompressible Navier-Stokes equation:

$$\frac{\partial \mathbf{v}}{\partial t} + (\mathbf{v} \cdot \nabla)\mathbf{v} = -\nabla p + \frac{1}{Re}\nabla^2 \mathbf{v}, \tag{3.25}$$

where p is the pressure field, Re is the Reynolds number of the incompressible flow and Pr is the Prandtl number. For this case, the value of the Reynolds number and Prandtl number are taken to be $Re = 3000$ and $Pr = 1/300$ respectively. The schematic of the domain for this problem is shown in Fig.(20). The length of the bottom boundary is $L = 10$. The height of the domain is $H = 5$. The left and right boundary at $x = -5$ and $x = 5$ are taken to be outflow boundaries, i.e., $\dfrac{\partial T}{\partial x} = 0$. The velocity at the top inflow boundary is taken to be $(u, v) = (0, -(1 - x^2/0.0625)\exp(-x^4/0.175^4) + 0.01\sin(\pi x))$. The incompressible flow is solved using spectral/hp method with $N_e = 4080$ and polynomial order 5. The (u, v) data from the incompressible solver is used for the solving Eq.(3.24). A stochastic Dirichlet boundary is introduced at the bottom wall with the temperature profile given by,

$$T(x, y = 0, t; \omega) = g_5(x, t; \omega).$$

The random boundary condition is taken as;

$$g_5(x, t; \omega) = 1 + \sigma_x \sum_{n=1}^{d} \frac{1}{n^3}\frac{1}{\sqrt{L_x}} \cos\left(\frac{n\pi x}{L_x}\right) \sin\left(\frac{n\pi t}{L_t}\right) \xi_n,$$

here, L_x and L_t are taken to be 5 and $\sigma_x = 0.05$. The choice of the spatial modes depends on the boundary at $(x, y) = (-5, 0)$ and $(5, 0)$. The spatial function $\cos\left(\frac{n\pi x}{L_x}\right)$ ensures that the boundary at those points satisfy the Neumann boundary conditions imposed at the

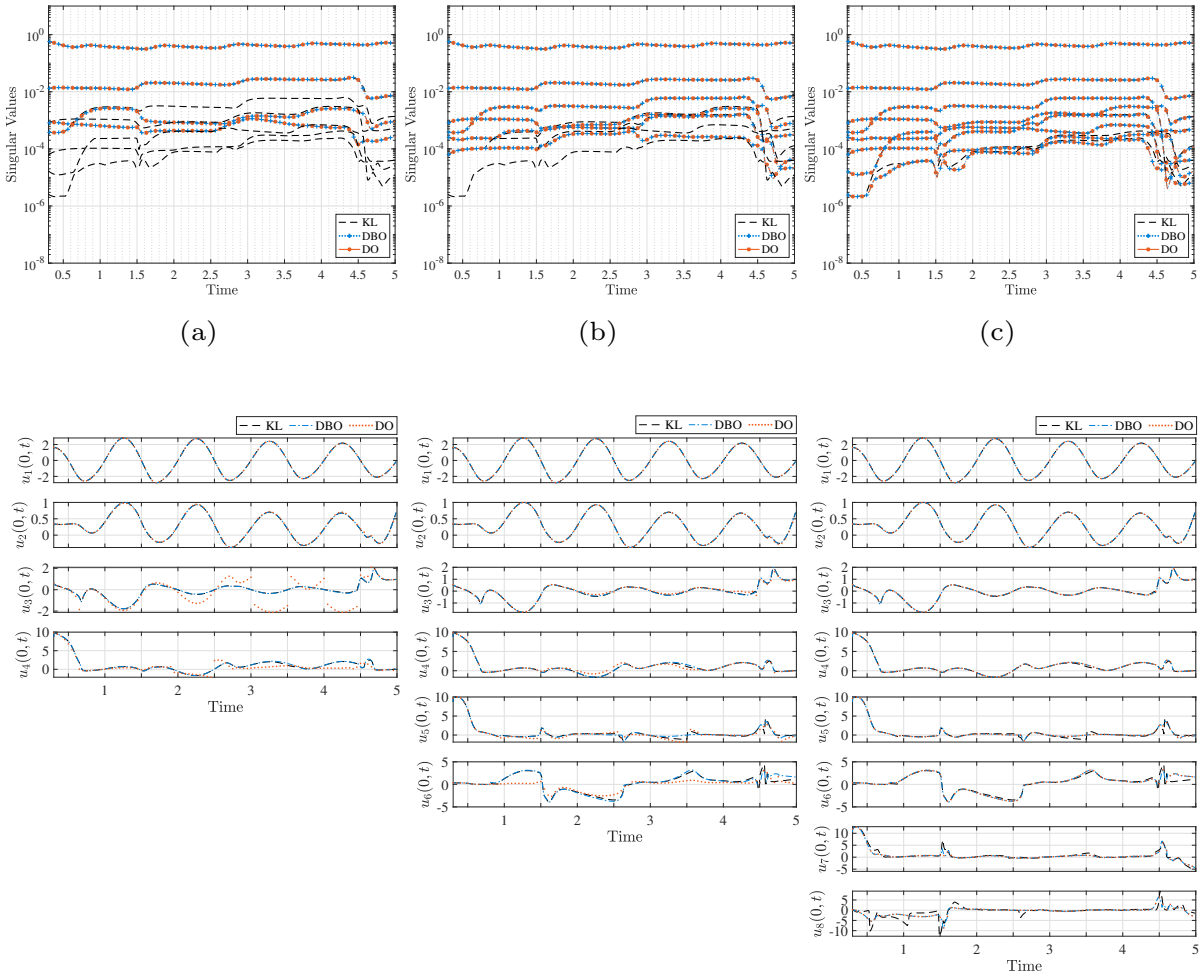

Figure 18: Burgers' equation: The first row shows the singular value comparison for KL, DBO and DO methods. The values are compared for three orders of reduction $r = 4, 6$ and 8. The evolution of the values of the modes at the left stochastic boundary are compared in the second row for the three methods.

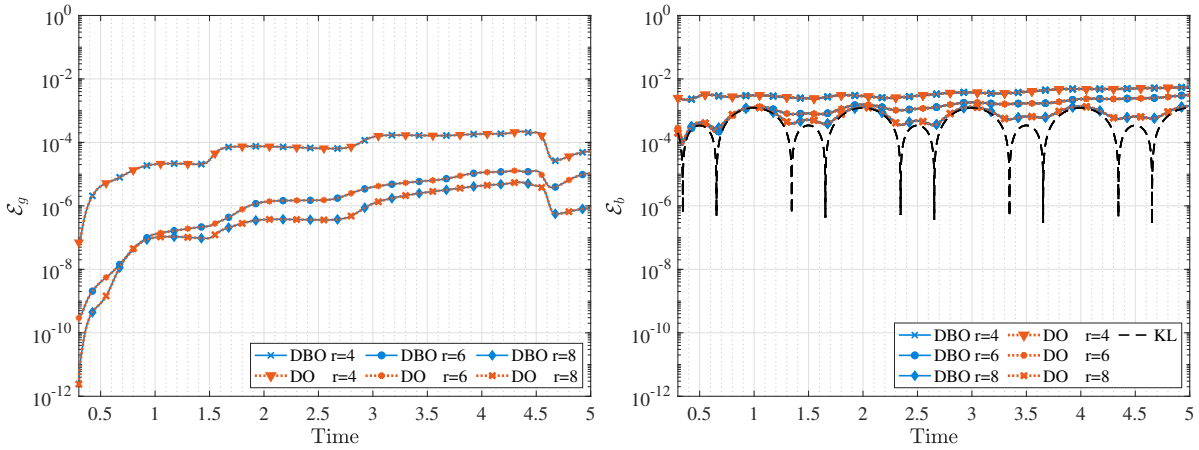

(a) Global Error

(b) Boundary error

Figure 19: Burgers' equation: Error comparison for DBO and DO as compared with the KL solution. The global error i.e., $\mathcal{E}_g$ and the boundary error i.e., $\mathcal{E}_b$ are shown in (a) and (b) respectively.

vertical outflow boundaries. The random space is taken to be $d = 6$ dimensional. The 6 dimensional random space is discretized with the ME-PCM tensor product rule [12, 48] with 1 element containing 3 points in each random direction which gives the total samples to be $s = 3^6 = 729$. All the other boundaries are taken to be wall boundaries. The temperature for all the boundaries is set to be $T = 0$. The fourth order Runge-Kutta method is used for time integration with $\Delta t = 5 \times 10^{-4}$. The system is evolved for $t_f = 11$ Time Units and the $t_s = 1$, is the switching time. Since, the initial conditions at $t = 0$ are deterministic and the stochasticity has not evolved in the system, the code is evolved till the switching time with the ME-PCM samples and the KL decomposition of the solution at $t = t_s$ is taken as the initial condition for the DBO and DO solver. The singular values and the error of the solution are compared with the solution obtained by solving for the ME-PCM samples. The singular value comparison for three different reduction orders i.e., $r = 3, 5$ & 7 is shown in Fig.(21). The global and boundary errors for this case are plotted in Fig.(23). We observe that the errors decrease as the reduction order is increased. As can be seen from the global

and boundary errors for $r = 9$, DBO gives better accuracy than the DO due to the better condition number of the Σ inversion. We also observe that the DBO boundary error for $r = 9$ is equal to the KL error. The evolution of the flow field for $t = 2.5, 5, 7.5, 10$ of the tenth sample of the ME-PCM solution and the evolution of the spatial modes of the DBO solution are shown in Fig.(24). The values of the boundary modes for different time instances are represented in a surface plot in Fig.(22). Visual comparison shows that there is a good match between the KL and the DBO solution.

3.2.7 2D Nonlinear Advection-Diffusion Equation

We lastly demonstrate the effect of stochastic boundary conditions on a two dimensional nonlinear equation. We consider the 2D advection-diffusion equation governed by:

$$\frac{\partial T}{\partial t} + (\mathbf{v} \cdot \nabla)T = \frac{1}{RePr}\nabla^2 T. \tag{3.26}$$

The velocity field $\mathbf{v} = (u, v)$ is obtained by solving the 2D incompressible Navier-Stokes equation i.e, Eq.(3.25). The Prandtl number for this case however, is taken to be temperature dependent: $Pr = f(T)$, which makes the governing equation weakly nonlinear. Here, we take Prandtl number to be $Pr = \frac{1}{300(\alpha+\beta T)}$. For this case, $\alpha = 1$ and $\beta = 0.9$. The Reynolds number is $Re = 3000$. The schematic of the problem is same as the previous case. The bottom boundary is taken to be Dirichlet boundary and the temperature profile at this boundary is given by,

$$T(x, y = 0; \omega) = g_6(x; \omega)$$
$$g_6(x; \omega) = 1 + \sigma_x \sum_{n=1}^{d} \frac{1}{n} \frac{1}{\sqrt{L_x}} \cos\left(\frac{n\pi x}{L_x}\right) \xi_n,$$

here, L_x and L_t are taken to be 5 and $\sigma_x = 0.5$. The Dirichlet boundary conditions for this case are taken to be time-independent. The boundaries at $x = -5$ and $x = 5$ are taken to be outflow boundaries i.e., $\dfrac{\partial T}{\partial x} = 0$. The choice of spatial modes is made to ensure that the points $(x, y) = (-5, 0)$ and $(5, 0)$ satisfy the Neumann boundary condition imposed at the outflow boundary. The random space is taken to $d = 6$. The samples for the random space are same as those taken in the linear case. The inflow condition at $y = 5$ is the same as the

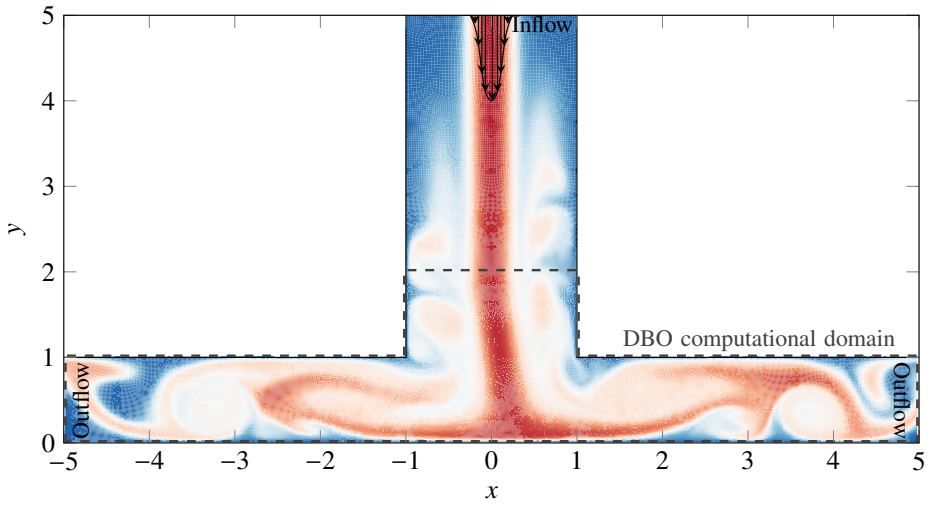

Figure 20: 2D linear case: The figure shows the computational domain for the Nektar computations. The Nektar simulations are used to compute the velocity field used to solver for the temperature equations using the DBO and DO methods. The dotted lines shows the computational domain used for the DBO computations. An inflow boundary condition is enforced at $y = 5$. Outflow boundary is enforced at $x = 5$ and $x = -5$. All other boundaries are taken to be wall boundary $(u, v = 0)$.

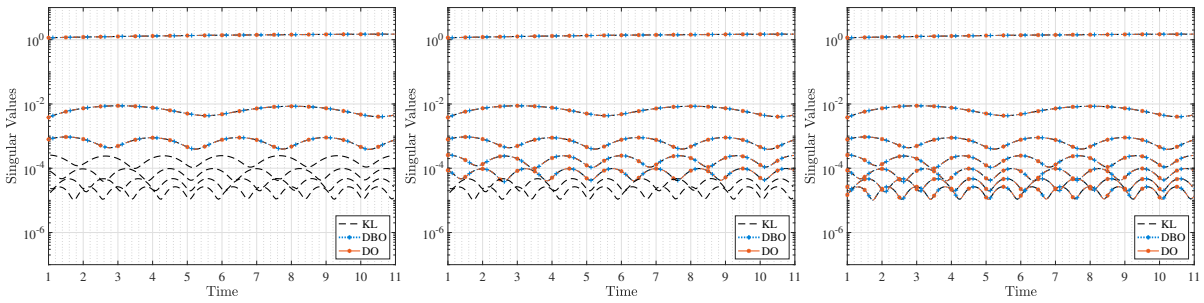

(a) (b) (c)

Figure 21: 2D linear case: The singular value comparison for KL, DBO and DO methods is shown. The values are compared for three orders of reduction $r = 3, 5$ & 7.

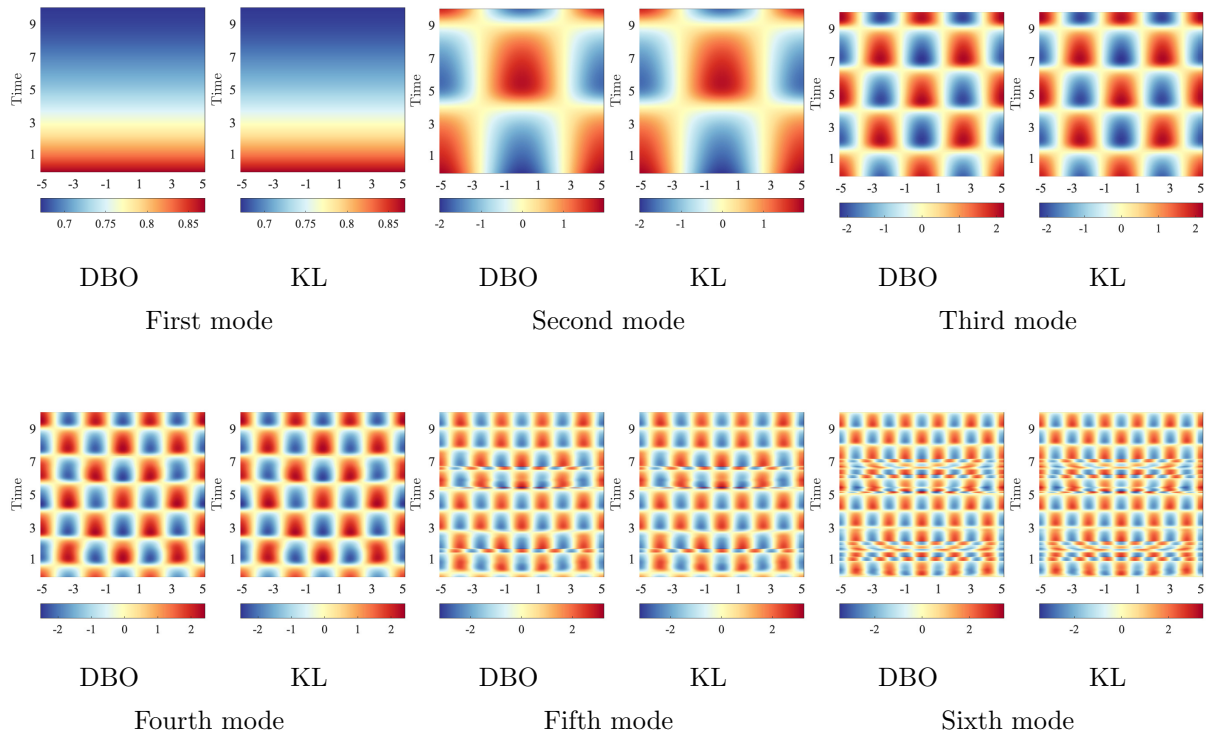

Figure 22: 2D linear case: The evolution of the values of the modes at the stochastic Dirichlet boundary at $y = 0$ are compared for DBO and KL.

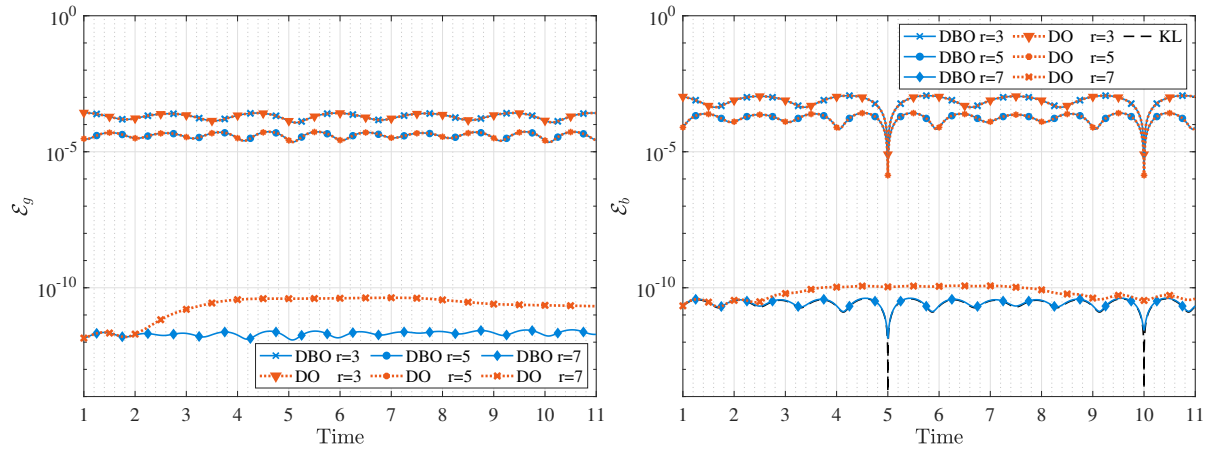

(a) Global Error (b) Boundary Error

Figure 23: 2D linear case: Error comparison for DBO and DO as compared with the KL solution. The figure on the left shows the comparison in the $\mathcal{E}_g$, i.e., global error. The figure on the right shows the comparison for the $\mathcal{E}_b$, i.e., boundary error.

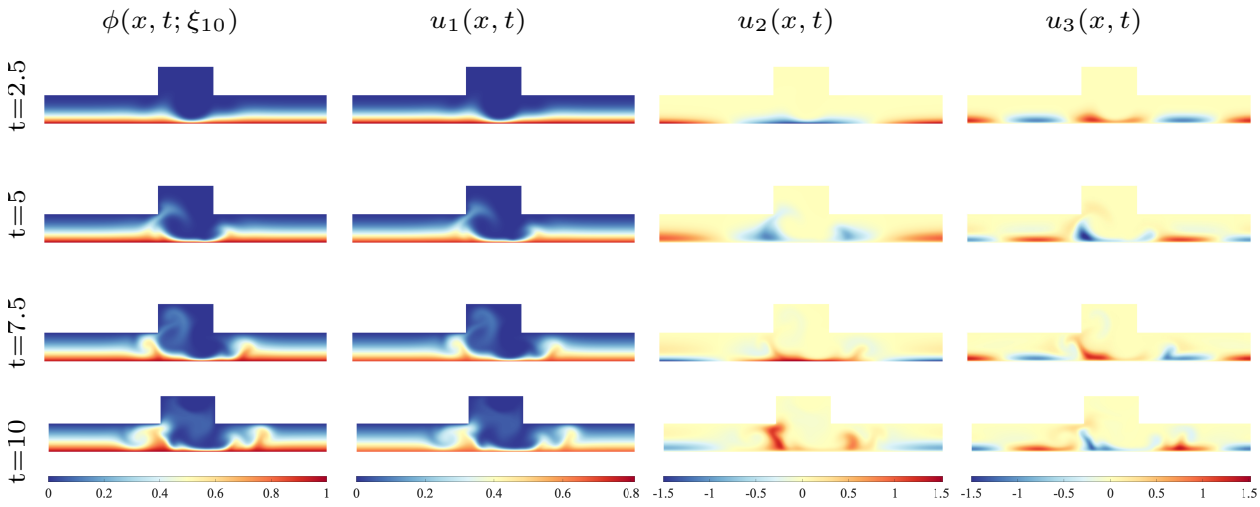

Figure 24: 2D linear case: Evolution of the first three spatial modes is shown for $t = 2.5, 5, 7.5, 10$. The first column shows the solution obtained for different time snapshots for the tenth sample. The next three columns show the evolution of the spatial modes as the flow field evolves.

previous case. The incompressible flow is solved using spectral/hp method with $N_e = 4080$ and polynomial order 5. The (u, v) data obtained from the incompressible solver is used for solving Eq.(3.26). All the other boundaries are taken to be wall boundaries. The temperature of all the other boundaries is set to $T = 0$. The fourth-order Runge-Kutta scheme is used for time integration with $\Delta t = 5 \times 10^{-4}$. The system is evolved for $t_f = 11$ Time Units and the t_s is the switching time. Since the initial conditions at $t = 0$ are deterministic and the stochasticity has not evolved in the system, the code is evolved till switching time with ME-PCM samples and the KL decomposition at $t = t_s$ is taken as the initial condition for DBO and DO modes. The singular values for this case are compared in Fig.(26). The singular values are compared for three different reduction orders, $r = 5, 7$ and 9. The error comparison for this case is plotted in Fig.(25). We observe that the errors improve for both DBO and DO as the order of reduction is increased. For the linear case, when $d = 6$ we observe that $r = 7$ can define the system exactly. However for the nonlinear case, we observe that modes 8 and 9 also have non-negligible singular values and that these values pick up energy as the system is evolved. The values of the boundary modes are for different time instances are shown in a surface plot in Fig.(27). The DBO shows a good match with the KL solution for the boundary modes.

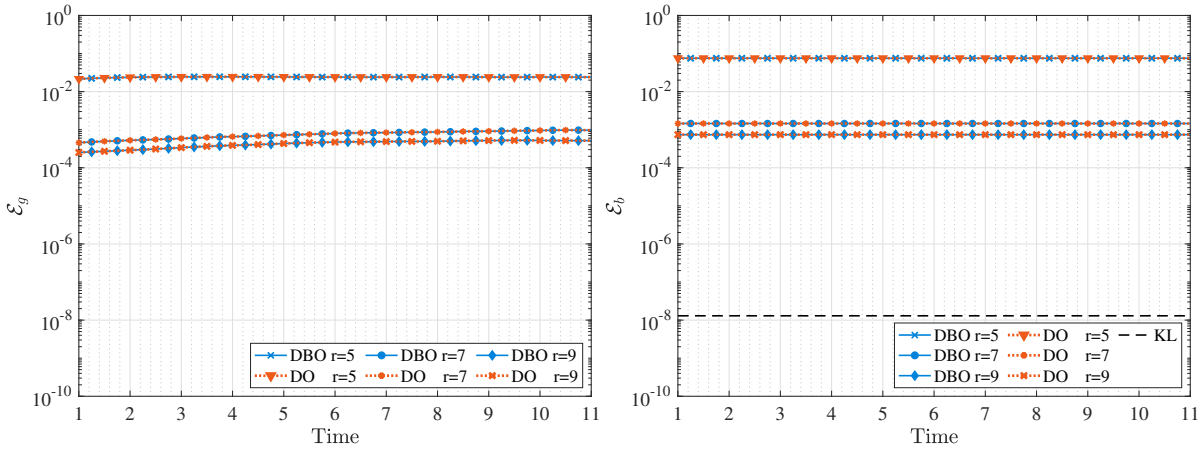

(a) Global Error (b) Boundary Error

Figure 25: 2D nonlinear case: Error comparison for DBO and DO as compared with the KL solution. The figure on the left shows the comparison in the $\mathcal{E}_g$, i.e., global error. The figure on the right shows the comparison for the $\mathcal{E}_b$, i.e., boundary error.

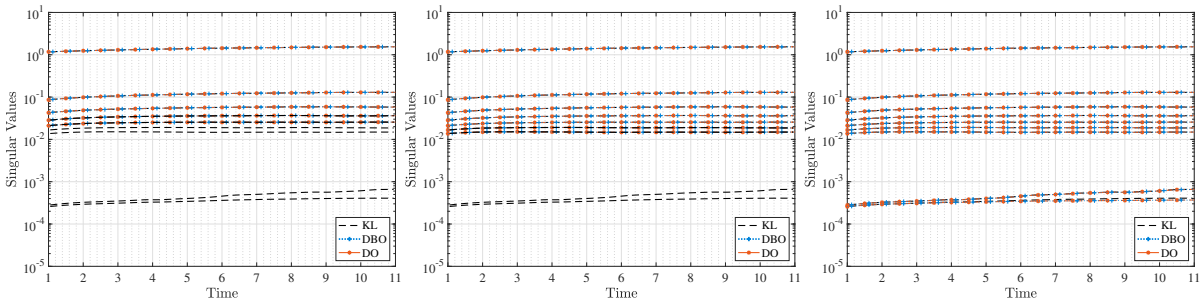

(a) (b) (c)

Figure 26: 2D nonlinear case: The singular value comparison for KL, DBO and DO methods is shown. The values are compared for three orders of reduction $r = 5, 7$ and 9

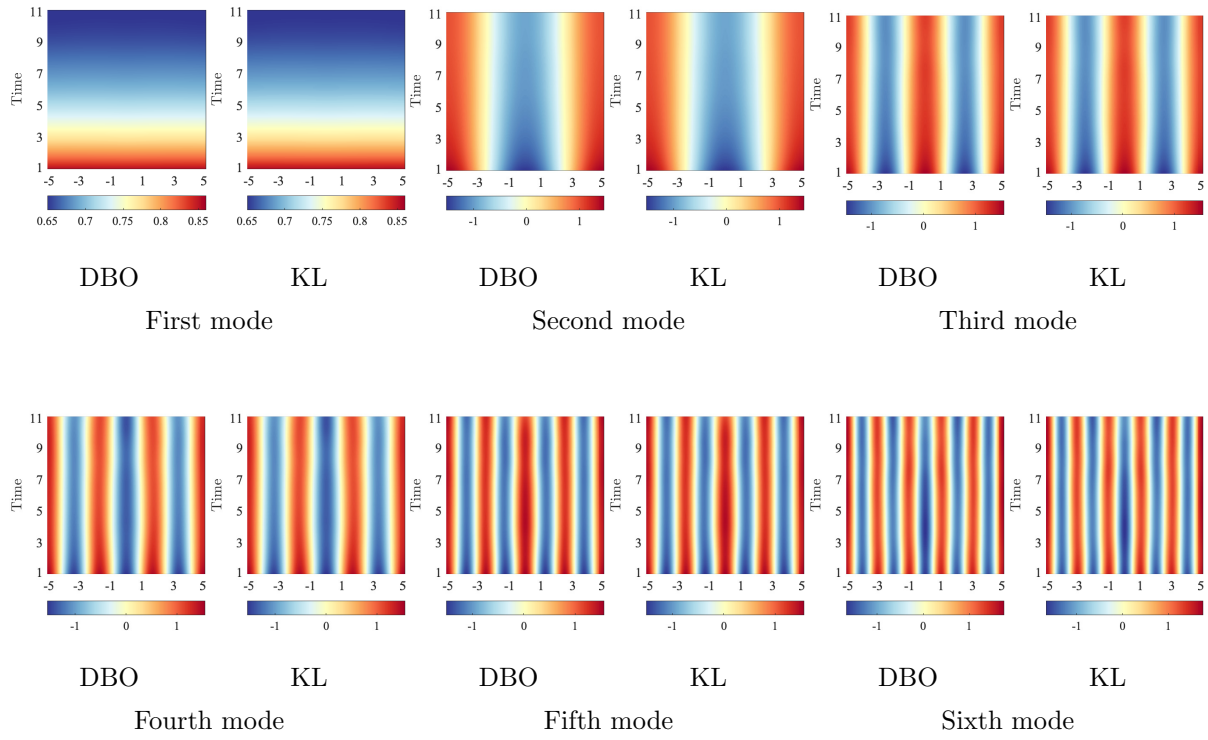

Figure 27: 2D nonlinear case: The evolution of the values of the modes for the stochastic Dirichlet boundary at $y = 0$ are compared for DBO and KL.

4.0 Application of Time-dependent Basis for Solving Deterministic PDEs

4.1 Introduction

The choice of basis is a *fundamental decision* in the representation of complex dynamical systems in the discrete numerical format. Partial differential equations (PDEs) defining the physical world systems can be expressed as a low dimensional encoding by exploiting the correlations in the complex dynamics and flow evolution. Using these correlations we can construct an optimal reduced order basis which is uniquely defined for the PDE we wish to solve. This perhaps, is a generalizable way to beat the 'curse of dimensionality '(exponential increase in computational cost with dimensions) for high dimensional PDEs. The goal of these reduced order models is two-fold: *simplicity of representations* and *faster and cheaper computations*. Proper Orthogonal Decomposition (POD) is a seminal technique in this area which was developed to analyse turbulent flows and obtain a low order representation which seeks to capture maximum energy-ranked modes of the system [49, 21, 22, 23]. The method consists of an *offline* computations stage, where the covariance matrix of the DNS snapshots is computed and the basis are extracted by eigenvector decomposition. During the *online* stage the evolution of the flow-physics is computed by performing a Galerkin projection of the basis on the model to obtain the time dependent coefficients. The POD technique has found applications in image processing, extracting coherent structure in turbulence [50], bifurcation analysis [51], flow control [52, 53] and complex geometry flows [54]. The POD method belongs to a larger class of projection based-techniques [52, 55] and incurs a high I/O storage cost and computational cost in generation of representation basis. Besides the defined basis are restricted by the snapshots of the solution and find it difficult to extrapolate the solution to different operating conditions (eg., Reynolds number, Mach number) and long time integration. Other techniques have been developed to overcome the aforementioned limitations: Least squares Petrov-galerkin [56], nonlinear model reduction techniques [57, 58], Koopman operators [59, 60, 61, 62] and Dynamic mode decomposition [24, 27].

Recently developments in area of deep neural networks (DNNs) for extracting low dimensional feature space has found applications in solving PDEs. The DNNs can be thought of as non-intrusive nonlinear reduced basis obtained through training the hyper-parameters for a particular dataset. Recent works include physics informed neural networks (PINNs) [63, 64, 65], DeepONet [66, 67], Deep Galerkin method (DGM) [68], autoencoders [69, 70, 71, 72, 73] which can be expressed as nonlinear extension of POD/SVD [74], Visual Interaction Networks [75], multi-layer convolution framework [76, 77], latent space physics [78]. The goal of the aforementioned techniques is to generate nonlinear representation functions for the PDEs by observing a series of snapshots of the evolution of the flow and minimizing the corresponding residual by computing the hyper-parameters of the neurons. As these techniques are highly data driven, they suffer from data generation cost and storage issues especially for high dimensional PDEs. Since these basis are static, they also suffer from the inability to represent transient dynamics in the flow.

Most reduced order models aim at finding a separation of variables form of the primary variable given by, $V(\mathbf{x}, t) = \alpha_i(t)\Phi_i(\mathbf{x})$, where $V(\mathbf{x}, t)$ denotes the primary variable, $\alpha_i(t)$ represents the time-dependent coefficients and $\Phi_i(\mathbf{x})$ are the low dimensional basis obtained from the offline computations of snapshots. In this work, we seek to find *time-dependent* reduced basis of the form $\Phi_i(\mathbf{x}, t)$. This allows the basis to "chase "the solution wherever it evolves and is useful in capturing transient dynamics. The concept of time-dependent basis is not new and has been developed in the context of uncertainty quantification [1, 79] for fluid flows. The method has previously existed in quantum mechanics [35], chemistry [36], dynamical low rank approximations [37] and dynamical tensor approximations [80]. The imposed conditions of orthonormality and dynamic orthogonality on the spatial basis need not be unique. Variants of the above method are bi-orthogonal decomposition (BO) [2, 32], hybrid BO-DO [40], dynamically bi-orthonormal (DBO) [46, 81]. The time-dependent basis (TDB) techniques have been adopted to problems in transient dynamics [33, 39, 82, 38], flow control[83], extreme events [84], computing sensitivities [85], skeletal model reduction [86], passive and reactive species transport [47], data compression in turbulent flows [87]. The method shows a few similarities to the evolutional DNN approach of setting the parameters for $t = 0$ and evolving them sequentially as time progresses [88, 89]. The dynamically bi-

orthonormal decomposition has a form which can be readily expanded to higher dimensions. The motivation of this chapter is to introduce the application of time-dependent basis for (i) deterministic PDEs (ii) derive the evolution equations of the one dimensional basis in each spatial directions and (iii) demonstrate the structure resolving capabilities of the method for incompressible and compressible Navier-Stokes equations.

4.2 Methodology

4.2.1 Definitions and notation

We consider a partial differential equation given by,

$$\frac{\partial V(\mathbf{x},t)}{\partial t} = \mathcal{M}(V,\mathbf{x},t), \qquad \mathbf{x} \in D, t > 0, \tag{4.1}$$

$$V(\mathbf{x},t_0) = V_0(\mathbf{x}), \qquad t = 0. \tag{4.2}$$

Here $\mathcal{M}$ is in general, a linear or non-linear differential operator, D denotes the domain, $\mathbf{x} = \{x_1, x_2, ..., x_d\}$ are d-dimensional independent variables. $V_0(\mathbf{x})$ represents the initial condition for the variable $V(\mathbf{x},t)$. We introduce the L_2 inner-product norm as,

$$\langle V(\mathbf{x}), U(\mathbf{x})\rangle_{\mathbf{x}} = \int_{x_d} \cdots \int_{x_1} V(\mathbf{x})U(\mathbf{x})\rho(x_1)\cdots\rho(x_d)dx_1\cdots dx_d,$$
$$\|U\|_{\mathbf{x}} = \langle U, U\rangle^{1/2}.$$

Here, $\rho(x_1), \cdots \rho(x_d)$ are the density weights in each direction. Similarly, an inner product for x_n is given by,

$$\langle V(\mathbf{x}), U(\mathbf{x})\rangle_{x_n} = \int_{x_n} V(\mathbf{x})U(\mathbf{x})\rho(x_n)dx_n,$$
$$\|u\|_{x_n} = \langle U, U\rangle_{x_n}^{1/2}.$$

We also introduce the following inner-product notation for inner-product with respect to all spatial dimensions except x_n as,

$$\langle V(\mathbf{x}), U(\mathbf{x}) \rangle_{\mathbf{x} \setminus x_n} =$$

$$\int_{x_d} \cdots \int_{x_{n+1}} \int_{x_{n-1}} \cdots \int_{x_1} V(\mathbf{x}) U(\mathbf{x}) \rho(x_1) \cdots \rho(x_{n-1}) \rho(x_{n+1}) \cdots \rho(x_d) dx_1 \cdots dx_{n-1} dx_{n+1} \cdots dx_d$$

4.2.2 Time Dependent Basis

We decompose a given variable $V(\mathbf{x}, t)$ as a set of time-dependent orthonormal basis (TDB) according to the equation,

$$V(\mathbf{x}, t) = \sum_{i_d=1}^{r_d} \cdots \sum_{i_2=1}^{r_2} \sum_{i_1=1}^{r_1} \underline{\mathbf{T}}_{i_1, i_2, \ldots, i_d}(t) u_{i_1}^{(1)}(x_1, t) u_{i_2}^{(2)}(x_2, t) \cdots u_{i_d}^{(d)}(x_d, t) + e(\mathbf{x}, t) \tag{4.3}$$

Here $\underline{\mathbf{T}}_{i_1, i_2, \ldots, i_d}(t) \in \mathbb{R}^{r_1 \times r_2 \times \cdots r_d}$ is a time-dependent core tensor and $\mathbf{U}^{(n)}(x_n, t) = [u_1^{(n)}(x_n, t) | u_2^{(n)}(x_n, t) | \cdots | u_{r_n}^{(n)}(x_n, t)]$ are the set of orthonormal modes in the n-direction. $e(\mathbf{x}, t)$ is the error obtained due to the reduced order modeling approximation. We define the unfolding of a tensor $\underline{\mathbf{T}} \in \mathbb{R}^{r_1 \times r_2 \times \cdots \times r_d}$ along a direction n is a matrix $\mathbf{T}_{(n)} \in \mathbb{R}^{r_n \times r_{n+1} \cdots r_d r_1 \cdots r_{n-1}}$

4.2.3 Evolution Equations

We derive close form equation for the evolution of the core tensor and the orthonormal modes in each direction. For simplicity, we derive the evolution equations for a three dimensional field which can be easily extended to higher dimensions. The decomposition is given by,

$$V(\mathbf{x}, t) = \sum_{i_3=1}^{r_3} \sum_{i_2=1}^{r_2} \sum_{i_1=1}^{r_1} \underline{\mathbf{T}}_{i_1, i_2, i_3}(t) u_{i_1}^{(1)}(x_1, t) u_{i_2}^{(2)}(x_2, t) u_{i_3}^{(3)}(x_3, t)$$

The orthornormality condition of the modes is enforced through the inner product of the modes,

$$\left\langle u_i^{(n)}(x_n, t), u_j^{(n)}(x_n, t) \right\rangle = \delta_{ij}, \quad i, j = 1, 2, \cdots r_n, \quad n = 1, 2, \cdots d. \tag{4.4}$$

For the purpose of this section $d = 3$. To obtain the evolution equations for the time-dependent bases we take a time derivative of the decomposition as,

$$\dot{V}(\mathbf{x},t) = \underline{\dot{\mathbf{T}}}_{i_1,i_2,i_3} u^{(1)}_{i_1} u^{(2)}_{i_2} u^{(3)}_{i_3} + \underline{\mathbf{T}}_{i_1,i_2,i_3} \dot{u}^{(1)}_{i_1} u^{(2)}_{i_2} u^{(3)}_{i_3} + \underline{\mathbf{T}}_{i_1,i_2,i_3} u^{(1)}_{i_1} \dot{u}^{(2)}_{i_2} u^{(3)}_{i_3} + \underline{\mathbf{T}}_{i_1,i_2,i_3} u^{(1)}_{i_1} u^{(2)}_{i_2} \dot{u}^{(3)}_{i_3} \tag{4.5}$$

Taking time derivative of the orthonormality condition,

$$\frac{d}{dt}\left\langle u^{(n)}_i(x_n,t), u^{(n)}_j(x_n,t)\right\rangle = \left\langle \dot{u}^{(n)}_i(x_n,t), u^{(n)}_j(x_n,t)\right\rangle + \left\langle u^{(n)}_i(x_n,t), \dot{u}^{(n)}_j(x_n,t)\right\rangle = 0$$

Let $\phi^{(n)}_{ij} = \left\langle \dot{u}^{(n)}_i(x_n,t), u^{(n)}_j(x_n,t)\right\rangle$, where $\phi(t)^{(n)} \in \mathbb{R}^{r_n \times r_n}$. We can see that $\phi(t)^{(n)}$ is a skew-symmetric matrix i.e., $\phi_{ij}(t)^{(n)} = -\phi_{ji}(t)^{(n)}$. To obtain the evolution equation for the core tensor, we take inner product $\left\langle \bullet, u^{(1)}_{i'_1} u^{(2)}_{i'_2} u^{(3)}_{i'_3}\right\rangle_{\mathbf{x}}$ on Eq.(4.5) and using the orthonormality condition of the modes we obtain,

$$\underline{\dot{\mathbf{T}}}_{i'_1,i'_2,i'_3} = \left\langle \dot{V}, u^{(1)}_{i'_1} u^{(2)}_{i'_2} u^{(3)}_{i'_3}\right\rangle_{\mathbf{x}} - \underline{\mathbf{T}}_{i_1,i'_2,i'_3}\phi^{(1)}_{i_1 i'_1} - \underline{\mathbf{T}}_{i'_1,i_2,i'_3}\phi^{(2)}_{i_2 i'_2} - \underline{\mathbf{T}}_{i'_1,i'_2,i_3}\phi^{(3)}_{i_3 i'_3}. \tag{4.6}$$

To obtain the evolution of the orthonormal basis $u^{(1)}_{i_1}$, we take the inner product $\left\langle \bullet, u^{(2)}_{i'_2} u^{(3)}_{i'_3}\right\rangle_{\mathbf{x}\setminus x_1}$ of Eq.(4.5)

$$\left\langle \dot{V}, u^{(2)}_{i'_2} u^{(3)}_{i'_3}\right\rangle_{\mathbf{x}\setminus x_1} = \underline{\dot{\mathbf{T}}}_{i_1,i'_2,i'_3} u^{(1)}_{i_1} + \underline{\mathbf{T}}_{i_1,i'_2,i'_3} \dot{u}^{(1)}_{i_1} + \underline{\mathbf{T}}_{i_1,i_2,i'_3} u^{(1)}_{i_1}\phi^{(2)}_{i_2 i'_2} + \underline{\mathbf{T}}_{i_1,i'_2,i_3} u^{(1)}_{i_1}\phi^{(3)}_{i_3 i'_3}.$$

Substituting the value of $\underline{\dot{\mathbf{T}}}_{i_1,i'_2,i'_3}$ from Eq.(4.6) in the above equation,

$$\left\langle \dot{V}, u^{(2)}_{i'_2} u^{(3)}_{i'_3}\right\rangle_{\mathbf{x}\setminus x_1} = \left[\left\langle \dot{V}, u^{(1)}_{i_1} u^{(2)}_{i'_2} u^{(3)}_{i'_3}\right\rangle_{\mathbf{x}} - \underline{\mathbf{T}}_{j_1,i'_2,i'_3}\phi^{(1)}_{j_1 i_1} - \underline{\mathbf{T}}_{i_1,i_2,i'_3}\phi^{(2)}_{i_2 i'_2} - \underline{\mathbf{T}}_{i_1,i'_2,i_3}\phi^{(3)}_{i_3 i'_3}\right] u^{(1)}_{i_1} + \underline{\mathbf{T}}_{i_1,i'_2,i'_3}\dot{u}^{(1)}_{i_1} + \underline{\mathbf{T}}_{i_1,i_2,i'_3} u^{(2)}_{i_1}\phi^{(2)}_{i_2 i'_2} + \underline{\mathbf{T}}_{i_1,i'_2,i_3} u^{(3)}_{i_1}\phi^{(3)}_{i_3 i'_3}$$

The equation becomes,

$$\left\langle \dot{V}, u^{(2)}_{i'_2} u^{(3)}_{i'_3}\right\rangle_{\mathbf{x}\setminus x_1} = \left[\left\langle \dot{V}, u^{(1)}_{i_1} u^{(2)}_{i'_2} u^{(3)}_{i'_3}\right\rangle_{\mathbf{x}} - \underline{\mathbf{T}}_{j_1,i'_2,i'_3}\phi^{(1)}_{j_1 i_1}\right] u^{(1)}_{i_1} + \underline{\mathbf{T}}_{i_1,i'_2,i'_3}\dot{u}^{(1)}_{i_1}$$

Rearranging the above terms we obtain,

$$\underline{\mathbf{T}}_{i_1,i'_2,i'_3}\dot{u}^{(1)}_{i_1} = \left\langle \dot{V}, u^{(2)}_{i'_2} u^{(3)}_{i'_3}\right\rangle_{\mathbf{x}\setminus x_1} - u^{(1)}_{i_1}\left[\left\langle \dot{V}, u^{(1)}_{i_1} u^{(2)}_{i'_2} u^{(3)}_{i'_3}\right\rangle_{\mathbf{x}} - \underline{\mathbf{T}}_{j_1,i'_2,i'_3}\phi^{(1)}_{j_1 i_1}\right]$$

The above equation can be considered as an under-determined systems with respect to the unknowns $\dot{u}^{(1)}_{i_1}$ if $r_1 > r_2 r_3$ and it could be an over-determined system otherwise. We find the

least squares solution to the above problem by multiplying the above equation by $\underline{\mathbf{T}}_{(1)}^T$ and computing the pesudo-inverse term given by $\mathbf{T}^{(1)\dagger} = \mathbf{T}_{(1)}^T \left(\mathbf{T}_{(1)}\mathbf{T}_{(1)}^T\right)^{-1}$. Thus the evolution equation for the orthonormal modes $u_{i_1}^{(1)}$ is given by,

$$\dot{u}_{i_1}^{(1)} = \left[\left\langle \dot{V}, u_{i_2'}^{(2)} u_{i_3'}^{(3)} \right\rangle_{\mathbf{x}\setminus x_1} - u_{i_1}^{(1)} \left\langle \dot{V}, u_{i_1}^{(1)} u_{i_2'}^{(2)} u_{i_3'}^{(3)} \right\rangle_{\mathbf{x}}\right] \mathbf{T}_{i_1,i_2'i_3'}^{(1)\dagger} + u_{i_1}^{(1)} \phi_{i_1'i_1}^{(1)}.$$

Similarly, the evolution equations for $u_{i_2}^{(2)}$ and $u_{i_3}^{(3)}$ are given by,

$$\dot{u}_{i_2}^{(2)} = \left[\left\langle \dot{V}, u_{i_1'}^{(1)} u_{i_3'}^{(3)} \right\rangle_{\mathbf{x}\setminus x_2} - u_{i_2}^{(2)} \left\langle \dot{V}, u_{i_1}^{(1)} u_{i_2'}^{(2)} u_{i_3'}^{(3)} \right\rangle_{\mathbf{x}}\right] \mathbf{T}_{i_2,i_1'i_3'}^{(2)\dagger} + u_{i_2}^{(2)} \phi_{i_2'i_2}^{(2)}.$$

$$\dot{u}_{i_3}^{(3)} = \left[\left\langle \dot{V}, u_{i_1'}^{(1)} u_{i_2'}^{(2)} \right\rangle_{\mathbf{x}\setminus x_3} - u_{i_3}^{(3)} \left\langle \dot{V}, u_{i_1}^{(1)} u_{i_2'}^{(2)} u_{i_3'}^{(3)} \right\rangle_{\mathbf{x}}\right] \mathbf{T}_{i_3,i_1'i_2'}^{(3)\dagger} + u_{i_3}^{(3)} \phi_{i_3'i_3}^{(3)}.$$

4.3 Variational Principle

It is shown in [47, 81] that the evolution equations for time dependent modes for reduced order modeling of stochastic fields in uncertainty quantification and species concentration in passive/reactive transport equations are obtained as optimal conditions of a variational principle. In this section we formulate the variational principle for the evolution of the time dependent basis for a n-dimensional tensor. The variational principle for the time dependent basis seeks to minimize the functional:

$$\mathscr{F}(\dot{u}_{i_1}^{(1)}, \dot{u}_{i_2}^{(2)}, \cdots, \dot{u}_{i_n}^{(n)}, \dot{\mathbf{T}}_{i_1,i_2,\ldots,i_n}) = \left\| \frac{d}{dt}\left(\dot{u}_{i_1}^{(1)}, \dot{u}_{i_2}^{(2)}, \cdots, \dot{u}_{i_n}^{(n)}, \dot{\mathbf{T}}_{i_1,i_2,\ldots,i_n}\right) - \mathcal{M} \right\|_F,$$

subject to the orthonormality conditions of the bases $\left\langle u_i^{(n)}(x_n,t), u_j^{(n)}(x_n,t)\right\rangle = \delta_{ij}$. Here, $\mathcal{M}$ represents the linear/nonlinear differential operator. Simply put, the variational principle seeks to minimize the distance between the time derivative of the time dependent basis decomposition and the right hand size of the partial differential equation by optimally updating the bases and the core tensor.

5.0 Demonstration Cases: Time-dependent Basis

5.1 2D Linear Advection Diffusion Equation

This case demonstrates the application of the TDB method for solving linear partial differential equations and the computational speed up obtained using this method as compared to the evolution of the DNS system.

5.1.1 Problem Statement

A periodic two dimensional domain is considered with $L_{x_1} = L_{x_2} = 2\pi$. $V(x_1, x_2, t)$ is a scalar whose evolution is given by the linear advection diffusion equation,

$$\frac{\partial V}{\partial t} + c_1 \frac{\partial V}{\partial x_1} + c_2 \frac{\partial V}{\partial x_2} = \nu \left(\frac{\partial^2 V}{\partial x_1^2} + \frac{\partial^2 V}{\partial x_2^2} \right), \qquad x_1, x_2 \in [0, 2\pi], t \in [0, T_f], \tag{5.1}$$

where c_1 and c_1 denote the velocities in the x_1- and x_2-directions respectively. These velocities are taken to be constant and $c_1 = 0.5$, $c_2 = 1.0$. The diffusion coefficient is denoted by ν and we take the value to be 0.01. The initial condition for the scalar $V(x_1, x_2, t)$ for which the equation is solved is given by,

$$V(x_1, x_2, t = 0) = \exp(-\sin(x_1)^3 \cos(2x_2)^3). \tag{5.2}$$

5.1.2 Evolution Equations Using The Time Dependent Basis Formulation

For the derivation of the evolution equations of the modes, we consider the time dependent basis decomposition,

$$V(x_1, x_2, t) = \sum_{i=1}^{r} \sum_{j=1}^{r} u_i^{(1)}(x_1, t)\ \mathbf{T}_{ij}(t)\ u_j^{(2)}(x_2, t), +\epsilon,$$

where $u_i^{(1)}(x_1, t), u_j^{(2)}(x_2, t)$ are the time dependent orthonormal modes in the x_1 and x_2 direction respectively, r denotes the reduction order and ϵ represents the residual error due to the reduction. $\mathbf{T}$ is a matrix which denotes the factor of the covariance matrix. For easy readability and sake of brevity in notation for the subsequent section, we denote $u_i^{(1)}(x_1, t)$ as $u_i^{(1)}$, $u_j^{(2)}(x_2, t)$ as $u_j^{(2)}$ and $\mathbf{T}_{ij}(t)$ as $\mathbf{T}_{ij}$. Thus, we can write the low rank form of $V_r(x_1, x_2, t)$ as,

$$V_r(x_1, x_2, t) = \sum_{i=1}^{r} \sum_{j=1}^{r} u_i^{(1)}(x_1, t)\ \mathbf{T}_{ij}(t)\ u_j^{(2)}(x_2, t). \tag{5.3}$$

To obtain the evolution equations for each of the components of the decomposition, we substitute Eq.(5.3) in Eq.(5.1) to obtain,

$$\frac{\partial}{\partial t}\left(u_i^{(1)}\mathbf{T}_{ij}u_j^{(2)}\right) = -c_1\frac{\partial u_i^{(1)}}{\partial x_1}\mathbf{T}_{ij}u_j^{(2)} - c_2 u_i^{(1)}\mathbf{T}_{ij}\frac{\partial u_j^{(2)}}{\partial x_2} + \nu\left(\frac{\partial^2 u_i^{(1)}}{\partial x_1^2}\mathbf{T}_{ij}u_j^{(2)} + u_i^{(1)}\mathbf{T}_{ij}\frac{\partial^2 u_j^{(2)}}{\partial x_2^2}\right). \tag{5.4}$$

The $u^{(1)}$ and $u^{(2)}$ modes are orthonormal and dynamically orthogonal i.e.,

$$\left\langle u_i^{(1)}, u_j^{(1)} \right\rangle = \delta_{ij}, \qquad \left\langle \frac{\partial u_i^{(1)}}{\partial t}, u_j^{(1)} \right\rangle = 0, \tag{5.5}$$

$$\left\langle u_i^{(2)}, u_j^{(2)} \right\rangle = \delta_{ij}, \qquad \left\langle \frac{\partial u_i^{(2)}}{\partial t}, u_j^{(2)} \right\rangle = 0. \tag{5.6}$$

Remark 5.1.1. $\left\langle \dot{u}_i^{(2)}, u_j^{(2)} \right\rangle$ *is a skew symmetric matrix. It has been shown in [47], that any choice of skew symmetric matrix leads to an equivalent low rank-approximation of the solution. Without the loss of generality, we assume the matrix to be a zero matrix.*

Taking inner product of Eq.(5.4) with $u_k^{(1)}$ and using the orthonormality and dynamic orthogonality condition from Eq.(5.5) we obtain,

$$\frac{d\mathbf{T}_{kj}}{dt}u_j^{(2)} + \mathbf{T}_{kj}\frac{\partial u_j^{(2)}}{\partial t} = -c_1\left\langle u_k^{(1)}, \frac{\partial u_i^{(1)}}{\partial x_1}\right\rangle \mathbf{T}_{ij}u_j^{(2)} - c_2\mathbf{T}_{kj}\frac{\partial u_j^{(2)}}{\partial x_2} + \nu\left(\left\langle u_k^{(1)}, \frac{\partial^2 u_i^{(1)}}{\partial x_1^2}\right\rangle \mathbf{T}_{ij}u_j^{(2)} + \mathbf{T}_{kj}\frac{\partial^2 u_j^{(2)}}{\partial x_2^2}\right). \tag{5.7}$$

To obtain the evolution equation for $\mathbf{T}_{ij}$, we take an inner product of the above equation with $u_m^{(2)}$ and apply the orthonormality and dynamic orthogonality condition from Eq.(5.6). Thus, we obtain,

$$\frac{d\mathbf{T}_{ij}}{dt} = -c_1\left\langle u_i^{(1)}, \frac{\partial u_k^{(1)}}{\partial x_1}\right\rangle \mathbf{T}_{kj} - c_2\mathbf{T}_{ik}\left\langle \frac{\partial u_k^{(2)}}{\partial x_2}, u_j^{(2)}\right\rangle + \nu\left(\left\langle u_i^{(1)}, \frac{\partial^2 u_k^{(1)}}{\partial x_1^2}\right\rangle \mathbf{T}_{kj} + \mathbf{T}_{ik}\left\langle \frac{\partial^2 u_k^{(2)}}{\partial x_2^2}, u_j^{(2)}\right\rangle\right). \tag{5.8}$$

To obtain the evolution equation of $u^{(2)}$ modes, we substitute the value of $\dot{\mathbf{T}}$ from Eq.(5.8) in Eq.(5.7). Thus, we obtain,

$$\begin{aligned}\mathbf{T}_{kj}\frac{\partial u_j^{(2)}}{\partial t} &= -c_1\left\langle u_k^{(1)}, \frac{\partial u_i^{(1)}}{\partial x_1}\right\rangle \mathbf{T}_{ij}u_j^{(2)} - c_2\mathbf{T}_{kj}\frac{\partial u_j^{(2)}}{\partial x_2} \\ &+ \nu\left(\left\langle u_k^{(1)}, \frac{\partial^2 u_i^{(1)}}{\partial x_1^2}\right\rangle \mathbf{T}_{ij}u_j^{(2)} + \mathbf{T}_{kj}\frac{\partial^2 u_j^{(2)}}{\partial x_2^2}\right) \\ &+ c_1\left\langle u_k^{(1)}, \frac{\partial u_m^{(1)}}{\partial x_1}\right\rangle \mathbf{T}_{mj}u_j^{(2)} + c_2\mathbf{T}_{ki}\left\langle \frac{\partial u_i^{(2)}}{\partial x_2}, u_j^{(2)}\right\rangle u_j^{(2)} \\ &- \nu\left(\left\langle u_k^{(1)}, \frac{\partial^2 u_m^{(1)}}{\partial x_1^2}\right\rangle \mathbf{T}_{mj}u_j^{(2)} + \mathbf{T}_{km}\left\langle \frac{\partial^2 u_m^{(2)}}{\partial x_2^2}, u_j^{(2)}\right\rangle u_j^{(2)}\right).\end{aligned} \tag{5.9}$$

We observe that term 1 and term 5 can be cancelled as well as term 3 and term 7. Simplifying the above equation and multiplying the equation by $\mathbf{T}_{kj}^{-1}$ on both sides we obtain,

$$\frac{\partial u_i^{(2)}}{\partial t} = -c_2\left[\frac{\partial u_i^{(2)}}{\partial x_2} - \left\langle \frac{\partial u_i^{(2)}}{\partial x_2}, u_j^{(2)}\right\rangle u_j^{(2)}\right] + \nu\left[\frac{\partial^2 u_i^{(2)}}{\partial x_2^2} - \left\langle \frac{\partial^2 u_i^{(2)}}{\partial x_2^2}, u_j^{(2)}\right\rangle u_j^{(2)}\right]. \tag{5.10}$$

Now to obtain the evolution equation for $u^{(1)}$ modes, we take inner product of Eq.(5.4) with $u_k^{(2)}$ and using the orthonormality and dynamic orthogonality condition from Eq.(5.6) we obtain,

$$\frac{\partial u_i^{(1)}}{\partial t}\mathbf{T}_{ik} + u_i^{(1)}\frac{d\mathbf{T}_{ik}}{dt} = -c_1\frac{\partial u_i^{(1)}}{\partial x_1}\mathbf{T}_{ik} - c_2 u_i^{(1)}\mathbf{T}_{ij}\left\langle \frac{\partial u_j^{(2)}}{\partial x_2}, u_k^{(2)} \right\rangle + \nu\left(\frac{\partial^2 u_i^{(1)}}{\partial x_1^2}\mathbf{T}_{ik} + u_i^{(1)}\mathbf{T}_{ij}\left\langle \frac{\partial^2 u_j^{(1)}}{\partial x_2^2}, u_k^{(2)} \right\rangle\right).$$

We sustitute the value of $\dot{\mathbf{T}}$ from Eq.(5.8) in the above equation. Thus, we obtain,

$$\begin{aligned}\frac{\partial u_i^{(1)}}{\partial t}\mathbf{T}_{ik} = &-c_1\frac{\partial u_i^{(1)}}{\partial x_1}\mathbf{T}_{ik} - c_2 u_i^{(1)}\mathbf{T}_{ij}\left\langle \frac{\partial u_j^{(2)}}{\partial x_2}, u_k^{(2)} \right\rangle \\ &+ \nu\left(\frac{\partial^2 u_i^{(1)}}{\partial x_1^2}\mathbf{T}_{ik} + u_i^{(1)}\mathbf{T}_{ij}\left\langle \frac{\partial^2 u_j^{(1)}}{\partial x_2^2}, u_k^{(2)} \right\rangle\right) \\ &+ c_1 u_i^{(1)}\left\langle u_i^{(1)}, \frac{\partial u_j^{(1)}}{\partial x_1} \right\rangle \mathbf{T}_{jk} + c_2 u_i^{(1)}\mathbf{T}_{ij}\left\langle \frac{\partial u_j^{(2)}}{\partial x_2}, u_k^{(2)} \right\rangle \\ &- \nu\left(u_i^{(1)}\left\langle u_i^{(1)}, \frac{\partial^2 u_j^{(1)}}{\partial x_1^2} \right\rangle \mathbf{T}_{jk} + u_i^{(1)}\mathbf{T}_{ij}\left\langle \frac{\partial^2 u_j^{(2)}}{\partial x_2^2}, u_k^{(2)} \right\rangle\right).\end{aligned}$$

We observe that term 2 and term 6 can be cancelled as well as term 4 and term 8. Simplifying the above equation and multiplying the equation by $\mathbf{T}_{ij}^{-1}$ on both sides we obtain,

$$\frac{\partial u_i^{(1)}}{\partial t} = -c_1\left[\frac{\partial u_i^{(1)}}{\partial x_1} - u_j^{(1)}\left\langle u_j^{(1)}, \frac{\partial u_i^{(1)}}{\partial x_1} \right\rangle\right] + \nu\left[\frac{\partial^2 u_i^{(1)}}{\partial x_1^2} - u_j^{(1)}\left\langle u_j^{(1)}, \frac{\partial^2 u_i^{(1)}}{\partial x_1^2} \right\rangle\right]. \tag{5.11}$$

Thus, Eq.(5.8), Eq.(5.11) and Eq.(5.10) describe the evolution equations of the modes and the factor of covariance matrix.

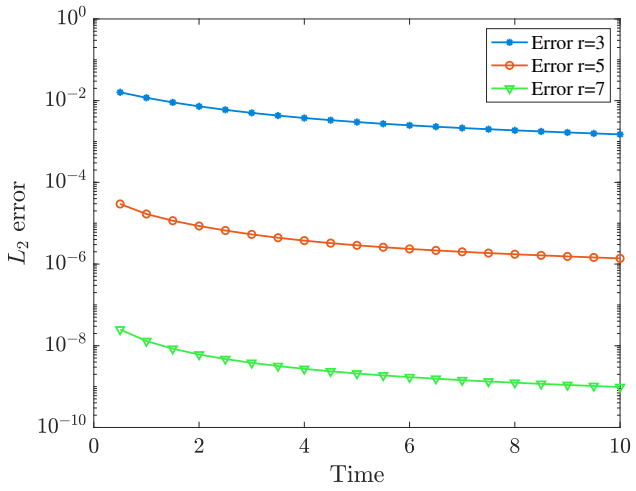

Figure 28: The evolution of the L_2-error is plotted for three different reduction orders: $r = 3, 5$ and 7. We observe that as the reduction order increases and as the modes capture lower singular values, the L_2 error reduces.

5.1.3 Computational Details

We discretize the domain using Fourier spectral methods with $N = 256$. The system is evolved using the evolution equations for the time dependent basis till $T_f = 10$. The fourth order Runge-Kutta method is used for time integration with $\Delta t = 0.0005$. The results of the TDB method are compared with the DNS solution for three different reduction orders $r = 3, 5, 7$. Fig.(28) shows the evolution of L_2 error for the three different reduction orders. We observe that as the reduction order is increased i.e., the modes capture lower singular values, the L_2 error decreases. Fig.(29) shows the evolution of the modes and the flow field for two different time step $t = 5$ and 10. The first column shows the evolution of the flow field. The second and the third column show the evolution of the x_1 and x_2 modes respectively. We observe that as the flow field evolves, the modes adapt to the solution as well.

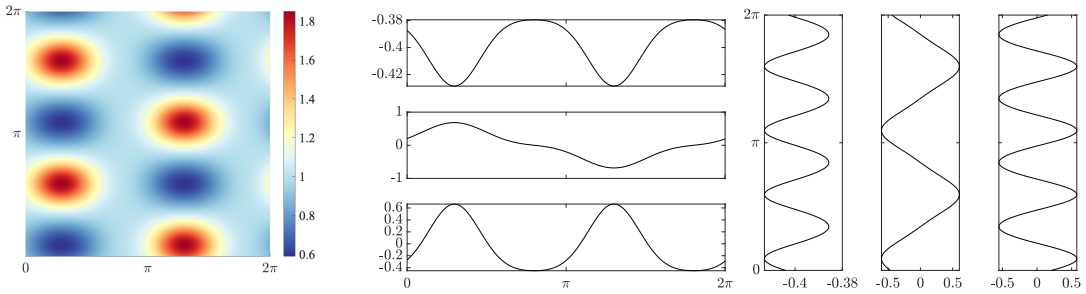

(a)

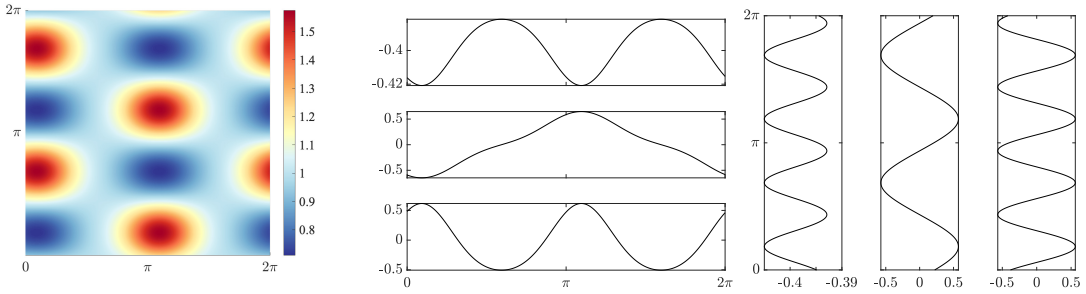

(b)

Figure 29: The above figure show the evolution of the flow field and the evolution of the x_1 and x_2 modes at $t = 5$ and 10.

5.1.4 Computational Cost

The computational cost associated with solving the evolution of $\mathbf{T}$ i.e., Eq.(5.8) is negligible as it as $r \times r$ matrix (where r is the order of reduction). As $r \ll N$ and the right hand side of Eq.(5.8) consists of computing matrices of size $r \times r$, this equation is computationally inexpensive. The equations for the evolution of the time dependent modes i.e, Eq.(5.10,5.11) consist of solving one dimensional partial differential equations of the size $N \times r$. This *compressed form* of the equations offers a massive computational speed-up as compared to the DNS solver which computes the solution of the partial differential equation of size $N \times N$. Table.(**??**) shows a comparison of the computational cost for the TDB and DNS solutions. We observe that the solution obtained from the evolution of the TDB modes is computationally cheaper than the DNS solution for a linear equation. The computations were performed on a Apple M1 processor.

The *compressed form* of the solution at every time step also offers memory storage advantages. The compressed form can be used to obtain the solution for entire flow-field without incurring the full storage cost. Considering $N \ll r$, the compression ratio can be given by $CR \approx N/r$. These computational and storage savings can be important for high performance computing problems where the bottle neck is generally memory limitations and computational cost of solving for the full domain.

5.2 Computational Cost: 2D Nonlinear Advection Diffusion Reaction Equation

In this case, we discuss the application of the TDB method for solving nonlinear partial differential equations and the challenges associated with the computational cost of nonlinear terms.

Table 3: The table shows the computational cost for the TDB and the DNS solutions. We see that the solution obtained from the evolution of the TDB modes is computationally cheaper than the DNS solution for a linear equation. The computational time for each of the simulations is evaluated on an Apple M1 processor.

Simulation	Computational cost
TDB $N = 256, r = 3$	1483.7 iter/sec
TDB $N = 256, r = 5$	1419.4 iter/sec
TDB $N = 256, r = 7$	1217.3 iter/sec
DNS 256×256	85.7 iter/sec
TDB $N = 512, r = 3$	1009 iter/sec
TDB $N = 512, r = 5$	898.9 iter/sec
TDB $N = 512, r = 7$	751.9 iter/sec
DNS 512×512	19.6 iter/sec

5.2.1 Problem Statement

Adding a nonlinear reaction terms to Eq.(5.1) we obtain the following equation,

$$\frac{\partial V}{\partial t}+c_1\frac{\partial V}{\partial x_1}+c_2\frac{\partial V}{\partial x_2}=\nu\left(\frac{\partial^2 V}{\partial x_1^2}+\frac{\partial^2 V}{\partial x_2^2}\right)+S(V), \qquad x_1,x_2\in[0,2\pi], t\in[0,T_f], \quad (5.12)$$

where $S(V,t)$ is a time dependent *nonlinear* reaction term. The $S(V)$ term acts as a forcing term for this equation. For the ease of notation, let us consider,

$$\begin{aligned} L(V) &= -c_1\frac{\partial V}{\partial x_1}-c_2\frac{\partial V}{\partial x_2}+\nu\left(\frac{\partial^2 V}{\partial x_1^2}+\frac{\partial^2 V}{\partial x_2^2}\right), \\ \implies \frac{\partial V}{\partial t} &= L(V)+S(V), \end{aligned} \quad (5.13)$$

where $L(V)$ is the linear term for the above equation.

5.2.2 Evolution Equations

The derivation of the evolution equation for the linear terms $L(V)$ is similar to the previous section. Let us consider the nonlinear term $S(V)$ which is a time dependent function of the scalar $V(x_1,x_2,t)$ to take the quadratic form i.e., $S(V)=f(V^2)$. The quadratic nonlinearity is a part of the Navier-Stokes equation through the term: $v_i\dfrac{\partial v_i}{\partial x_j}$. Considering a discretized form of $V(x_1,x_2,t)$ at a given time instant, we obtain a matrix $\mathbf{V}_{N\times N}$. Where N represents the number of discretized points in the x_1- and x_2- directions of the domain. The $f(\mathbf{V}^2)$ term now represents a Hadamard product (element-wise multiplication) of the matrix $\mathbf{V}$ with itself. Due to the Hadamard product the rank of the nonlinear term changes.

$$\text{rank}(\mathbf{V}^2)\leq \text{rank}(\mathbf{V})\text{rank}(\mathbf{V})$$

This expansion/contraction in the rank needs to be taken into account while computing the evolution equations of the modes. Consider two square matrices $\mathbf{A},\mathbf{B}\in\mathbb{R}^{N\times N}$ with the singular value decompositions given by,

$$\mathbf{A}=\mathbf{U_A}\mathbf{\Sigma_A}\mathbf{V_A}^T, \qquad \mathbf{B}=\mathbf{U_B}\mathbf{\Sigma_B}\mathbf{V_B}^T.$$

Assuming a low rank representation of the matrices i.e., $r_A, r_B < N$, where r_A is the low rank of $\mathbf{A}$ and r_B is the low rank of $\mathbf{B}$. $\mathbf{U_A}\in\mathbb{R}^{N\times r_A}, \mathbf{U_B}\in\mathbb{R}^{N\times r_B}$ are the left eigenvectors

of $\mathbf{A}$ and $\mathbf{B}$ respectively. $\mathbf{V_A} \in \mathbb{R}^{N\times r_A}, \mathbf{V_B} \in \mathbb{R}^{N\times r_B}$ are the right eigenvectors of $\mathbf{A}$ and $\mathbf{B}$ respectively. $\mathbf{\Sigma_A} \in \mathbb{R}^{r_A\times r_A}, \mathbf{\Sigma_B} \in \mathbb{R}^{r_B\times r_B}$ represent the diagonal singular value matrix of $\mathbf{A}$ and $\mathbf{B}$ respectively. The Hadamard product of two matrices can be written in the following representation,

$$\mathbf{A}\circ\mathbf{B} = \left(\mathbf{U_A^T}\odot\mathbf{U_B^T}\right)^T_{N\times r_Ar_B}\left(\mathbf{\Sigma_A}\otimes\mathbf{\Sigma_B}\right)_{r_Ar_B\times r_Ar_B}\left(\mathbf{V_A^T}\odot\mathbf{V_B^T}\right)_{r_Ar_B\times N}.$$

Here, $\circ$ represents the Hadamard product of two matrices, $\odot$ represents the Khatri-Rao product and $\otimes$ represents the Kronecker product. In case of $r_A \ll N, r_B \ll N$ the equations can be computed in a low rank format or the *compressed form*. The size of the matrices and the computational cost associated with computing the $\left(\mathbf{U_A^T}\odot\mathbf{U_B^T}\right)^T_{N\times r_Ar_B}$ and $\left(\mathbf{V_A^T}\odot\mathbf{V_B^T}\right)_{r_Ar_B\times N}$ can increase significantly for $r_Ar_B > N$. This cost increase in the low rank form can exceed the cost of the DNS simulation.

Besides the computational cost associated with the nonlinear term, the low rank format for other nonlinearities cannot be easily computed. Hence, for nonlinear simulations we compute the equations in the *decompressed form*, wherein the right hand side of the equations are computed pointwise at every grid point in the domain. This makes the computational cost of the TDB simulations of nonlinear equations equivalent to the computational cost of the DNS simulations. Effective techniques for cost reduction of the TDB simulations of nonlinear equations will be explored in future work.

To compute the evolution equations of the nonlinear term, we substitue the Eq.(5.3) in the nonlinear part of Eq.(5.13),

$$\frac{\partial}{\partial t}\left(u_i^{(1)}\mathbf{T}_{ij}u_j^{(2)}\right) = S(u_i^{(1)}(x_1,t)\ \mathbf{T}_{ij}(t)\ u_j^{(2)}(x_2,t)). \tag{5.14}$$

In numerical computations, the reconstructed form of $V_r(x_1,x_2,t)$ from the low rank form is used to compute $S(V_r)$. Taking inner product of the above equation (nonlinear terms) with $u_k^{(1)}$ and using the orthonormality and dynamic orthogonality condition from Eq.(5.5) we obtain,

$$\frac{d\mathbf{T}_{kj}}{dt}u_j^{(2)} + \mathbf{T}_{kj}\frac{\partial u_j^{(2)}}{\partial t} = \left\langle u_k^{(1)}, S(V_r)\right\rangle. \tag{5.15}$$

To obtain the nonlinear terms in the evolution equation of T_{ij} we take an inner product of the above equation wiht $u_m^{(2)}$ and apply the orthonormality and dynamic orthogonality condition from Eq.(5.6). Thus, we obtain,

$$\frac{d\mathbf{T}_{ij}}{dt} = \left\langle \left\langle u_i^{(1)}, S(V_r) \right\rangle, u_j^{(2)} \right\rangle. \tag{5.16}$$

Rewriting Eq.(5.15) and substituting the value of $\mathbf{T}_{kj}$ from Eq.(5.16) we get,

$$\begin{aligned} \frac{\partial u_j^{(2)}}{\partial t} &= \left\langle u_k^{(1)}, S(V_r) \right\rangle - \left\langle \left\langle u_k^{(1)}, S(V_r) \right\rangle, u_j^{(2)} \right\rangle u_j^{(2)}, \\ \frac{\partial u_j^{(2)}}{\partial t} &= \left(\left\langle u_k^{(1)}, S(V_r) \right\rangle - \left\langle \left\langle u_k^{(1)}, S(V_r) \right\rangle, u_j^{(2)} \right\rangle u_j^{(2)} \right) \mathbf{T}_{kj}^{-1}. \end{aligned} \tag{5.17}$$

To obtain evolution equation of $u^{(1)}$ modes, we take the inner product of Eq.(5.14) with $u_k^{(2)}$ and using the orthonormality and dynamic orthogonality condition from Eq.(5.6) we obtain,

$$\frac{\partial u_i^{(1)}}{\partial t}\mathbf{T}_{ik} = \left\langle S(V_r), u_k^{(2)} \right\rangle - u_i^{(1)} \frac{d\mathbf{T}_{ik}}{dt}.$$

Substituting the value of $\mathbf{T}_{ik}$ in the baove equation we obtain

$$\frac{\partial u_i^{(1)}}{\partial t} = \left(\left\langle S(V_r), u_k^{(2)} \right\rangle - u_i^{(1)} \left\langle \left\langle u_i^{(1)}, S(V_r) \right\rangle, u_k^{(2)} \right\rangle \right) \mathbf{T}_{ik}^{-1}. \tag{5.18}$$

Thus, Eq.(5.16), Eq.(5.17) and Eq.(5.18) show the evolution of the nonlinear terms of the linear advection diffusion equations for $\mathbf{T}, u^{(2)}, u^{(1)}$ respectively.

5.3 Vortex Dipole

In this case, we demonstrate the ability of the time-dependent basis for solving incompressible Navier-Stokes equations and the property of the modes to adapt according to the evolution of the flow-field. The case has been referred from [90]. We also demonstrate the advantage of using time dependent basis over static basis obtained from Proper Orthogonal decomposition (POD). Due to the localization of the vortices in the domain at a given time instant, static basis need to observe the solution for all the time steps to obtain the appropriate basis. Static basis find it difficult to extrapolate the solution based on a few observations. The POD solution in this example is shown for two cases: (i) *POD basis are extracted from solution at a few time steps* (ii) *POD basis are extracted from solution at all time steps*. We also study the error convergence properties of the two methods with different reduction orders.

5.3.1 Problem Statement

A periodic to dimensional domain is considered with $L_{x_1} = L_{x_2} = 1$. $\omega(x_1, x_2, t)$ is the vorticity in the x_3 direction and $\psi(x_1, x_2, t)$ is the streamfunction whose evolution is given by the vorticity-streamfunction equations,

$$\frac{\partial \omega}{\partial t} + v_1 \frac{\partial \omega}{\partial x_1} + v_2 \frac{\partial \omega}{\partial x_2} = \frac{1}{Re}\left(\frac{\partial^2 \omega}{\partial x_1^2} + \frac{\partial^2 \omega}{\partial x_2^2}\right),$$
$$\nabla^2 \psi = -\omega.$$

Here, Re denotes the Reynolds number which is taken to be 2000. The streamfunction is used to compute the velocities in the x_1 and the x_2- directions i.e., v_1 and v_2 using the following equations,

$$v_1 = \frac{\partial \psi}{\partial x_2}, \qquad v_2 = -\frac{\partial \psi}{\partial x_1}.$$

We use the TDB formulation to solve for the vorticity equation using the decomposition,

$$\omega(x_1, x_2, t) = u_i^{(1)}(x_1, t)\mathbf{T}_{ij}(t)u_j^{(2)}(x_2, t).$$

5.3.2 Computational Details

At $t = 0$, we consider two vortices with Gaussian profile and opposite circulation. The vorticity field at $t = 0$ is taken to be superposition of the two vortices given by,

$$\begin{aligned}\omega(x_1, x_2, t = 0) =& \frac{\Gamma_1}{\pi r_1^2} \exp\left(-\frac{(x_1 - 0.1)^2 + (x_2 - 0.47)^2}{r_1^2}\right) \\ &+ \frac{\Gamma_2}{\pi r_2^2} \exp\left(-\frac{(x_1 - 0.1)^2 + (x_2 - 0.53)^2}{r_2^2}\right).\end{aligned}$$

Here we take, $\Gamma_1 = -\Gamma_2 = -\pi/20$, $r_1^2 = r_2^2 = 1/1000$. The vorticity at $t = 0$ is shown in Fig.(30). We discretize the space with 256 Fourier spectral modes in both x_1 and x_2 directions. The fourth order Runge-Kutta method is used for evolving the system in time with $\Delta t = 0.0005$. The system is evolved till $T_{final} = 11$. For the TDB solution, the system is evolved till $T_i = 1$ using the DNS evolution equations. We take the singular value decomposition of the solution at $t = T_i$ time instant and the modes are initialized using the eigenvectors obtained from the SVD. Similarly the $\mathbf{T}$ matrix is initialized using the singular values. For $t > 1$ the TDB formulation is used for the evolution of the vorticity. The streamfunction at every step for both methods is computed by taking the inverse of the Laplacian computed in the 2D Fourier transform space.

$$\hat{\psi} = -\left(\nabla^2\right)^{-1} \hat{\omega}$$

For the POD solution, the system is initialized for the coefficients of the POD modes at $T_i = 1$ using the DNS solution. The POD modes are obtained by taking eigenvectors of covariance matrix obtained by taking snapshots of the DNS solution till $T_{observed}$ at every 500th time step. The value of $T_{observed}$ taken for forming the POD modes affects the accuracy of the solution. To demonstrate the effect of $T_{observed}$ on the solution, we take two cases: (i) $T_{observed} = 5.5$ (ii)$T_{observed} = 11$. The POD modes for both the cases are shown in Fig.(31). The first row shows the shape of the modes for $T_{observed} = 5.5$. The second row shows the shape of the modes for $T_{observed} = 11$. The first column shows the mean of the snapshots for the respective cases. Column 2,3 and 4 show the structure of the modes in order of decreasing energy. The modes in row 2, can be seen to extend to more area as that case has been exposed to more snapshots of the solution.

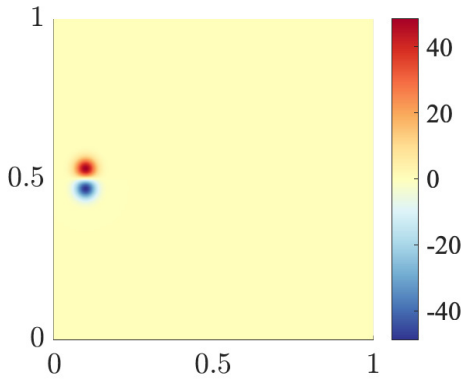

Figure 30: The vorticity field at $t = 0$ is shown. The vortex centers lie at $(0.1, 0.47)$ and $(0.1, 0.53)$. The vortices have equal and opposite strengths. This vortex dipole configuration induces a velocity to the right on both the vortices and we will see them move to the right as time evolves.

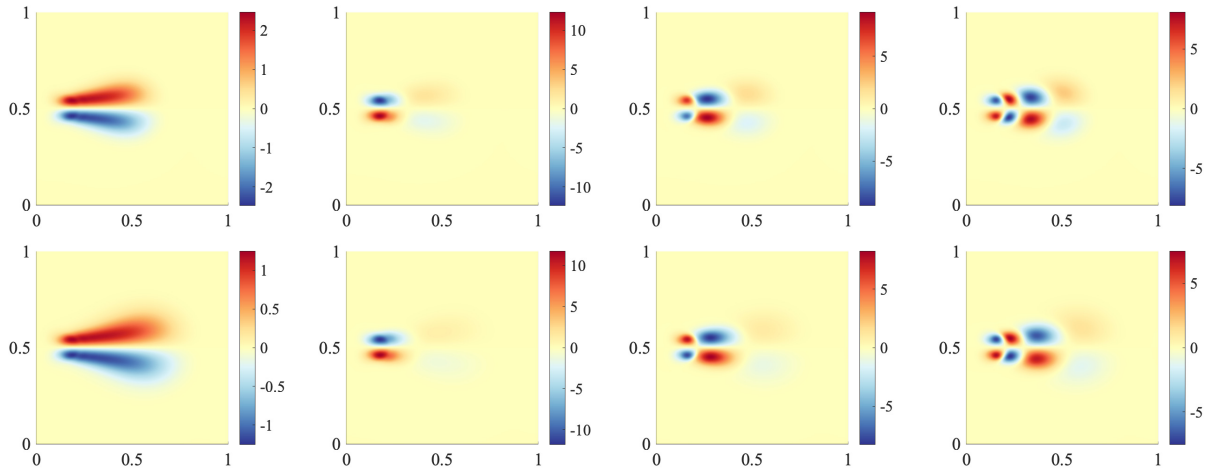

Figure 31: The figure shows the structure of the POD modes for the two cases. The first row shows the shape of the modes for $T_{observed} = 5.5$. The second row shows the shape of the modes for $T_{observed} = 11$. The first column shows the mean of the snapshots taken. Column 2,3 and 4 show the modes in the order of decreasing energy. We observe that the modes in row 2, occupy more area as compared to the modes in row 1 due to the increase in the time for which the solution is observed.

The evolution of the vorticity flow field as time evolves is shown in Fig.(32) for the TBD solution. The two vortices induces velocity in x_1 direction on each other and the vortices convect towards right as seen at $t = 4, 6, 8, 10$. Along with convection, we also observe that the vortices diffuse as seen with the increasing area of the vortices and decreasing strength of the vorticity field. Fig.(33) and Fig.(34) show the evolution of the vorticity solution with the POD modes. The POD modes are constructed based on snapshots of a reference solution. Since the snapshots of the reference solution are taken till $T_{observed} = 5.5$ for Fig.(33), the vortices in the figure show distortion for $t > 6$. Extrapolation of the solution is one of the drawbacks of the POD method. Extrapolation and the localized nature of the solution cause the flow field to incorrectly evolve beyond $T_{observed}$.

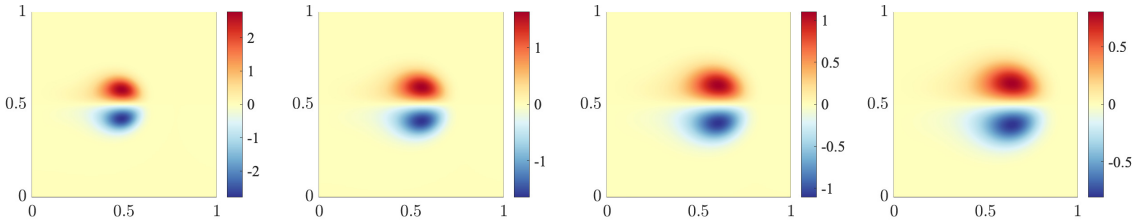

(a) $t = 4$ (b) $t = 6$ (c) $t = 8$ (d) $t = 10$

Figure 32: The TDB evolution of the vortex dipole at $t = 4, 6, 8, 10$ is shown in the figure above. We observe that the dipole convects to the right as time evolves. We also observe the diffusion of the vortices as seen by the increase in the area of the vortices and the decreasing strength of the vortices.

Fig.(35) shows the evolution of the first two modes time dependent modes at $t = 2, 4, 6, 8, 10$. The first row shows the evolution of the modes in the x_1 direction. It is observed that as the vortex convects to the right the localized mode convects to the right as well. We also observe the decreasing strength of the vortices as seen in the reduction of the amplitude of the first and second modes as time evolves. The second row show the evolution of the modes in the x_2 direction. We observe a change in the amplitude of the mode due to diffusion as time progresses. Since, there is no drift of the vortices in the x_2 direction, the point of inflection of the modes stays constant at $x_2 = 0$ for all times.

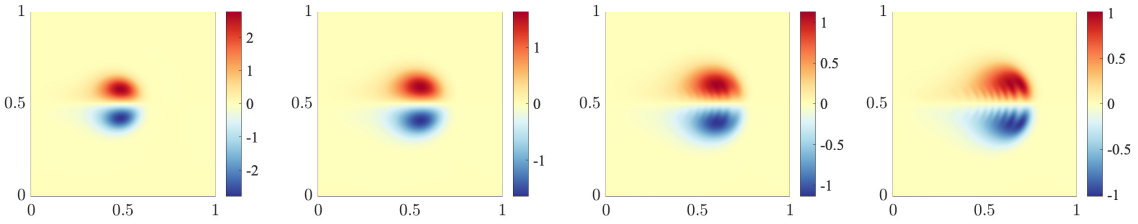

(a) $t = 4$ (b) $t = 6$ (c) $t = 8$ (d) $t = 10$

Figure 33: The solution obtained from POD for the case where $T_{observed} = 5.5$ is shown in the figure above. Since, the POD modes were exposed to the evolution of the vortex till $t = 5.5$, the solution till $t = 6$, is observed to be correct. However, the vortices for $t = 8, 10$ show distortion near $x_2 = 0.5$.

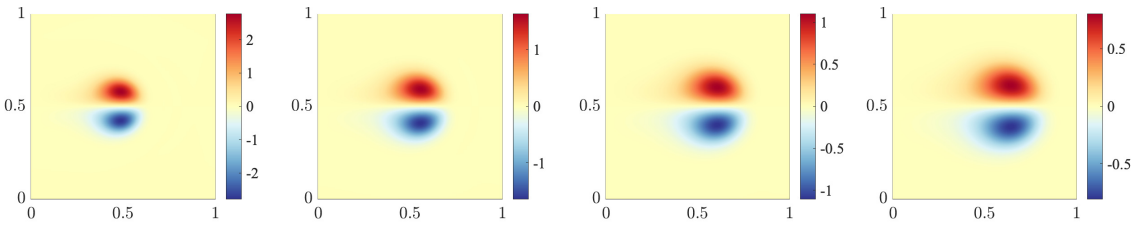

(a) $t = 4$ (b) $t = 6$ (c) $t = 8$ (d) $t = 10$

Figure 34: The solution obtained from POD for the case where $T_{observed} = 11$ is shown in the figure above. In this case, since the POD modes were exposed to the evolution of the vortex till $t = 11$, the solution is observed to match the DNS solution for all time steps. No vortex distortion is observed.

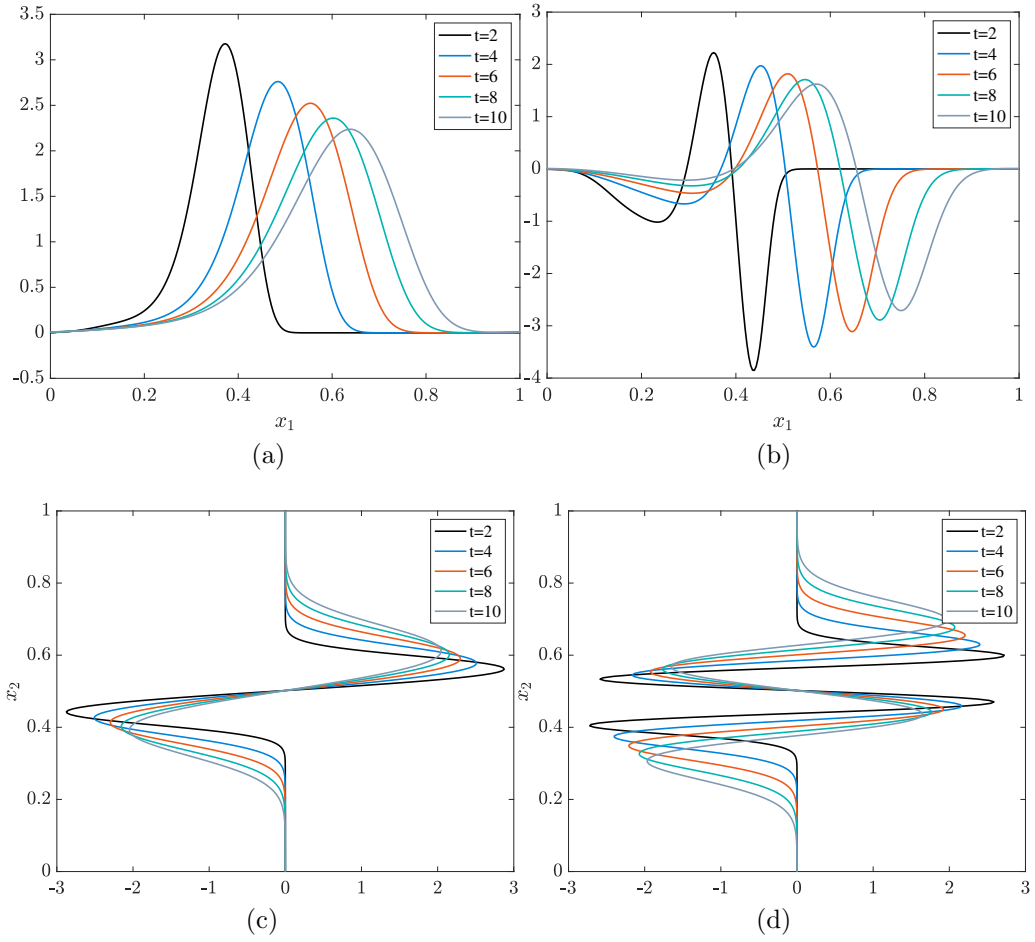

Figure 35: Row one shows the evolution of the modes in the x_1 direction. It is observed that as time progressed the modes convect to the right. The second row shows the evolution of the x_2 modes for $t = 2, 4, 6, 8, 10$. It is observed that the modes in the x_2 direction change in amplitude as the diffusion causes the vortices to lose their strength and increase in area. This change in the structure of the vortices is observed from the modes in the x_2 direction.

We perform the analysis of the time-dependent basis for three different reduction orders $r = 5, 10, 15, 20$. The evolution of the error is plotted in Fig.(36) for both POD and TDB solution. The figure on the left shows the comparison of error for TDB solution with the POD case where $T_{observed} = 5.5$. We observe that TDB solution has an overall lower error as compared to POD. We also jump in the error beyond $T_{observed}$. The solution is not able to extrapolate the solution for $t > 5.5$. The figure on the right shows the error comparison for $T_{observed} = 11$. Since no extrapolation of the solution is performed the solution does not show a sudden jump in the error. The TDB solution shows a lower error than the POD solution for the same reduction order. For both the cases we observe that as the reduction order increases, the error decreases.

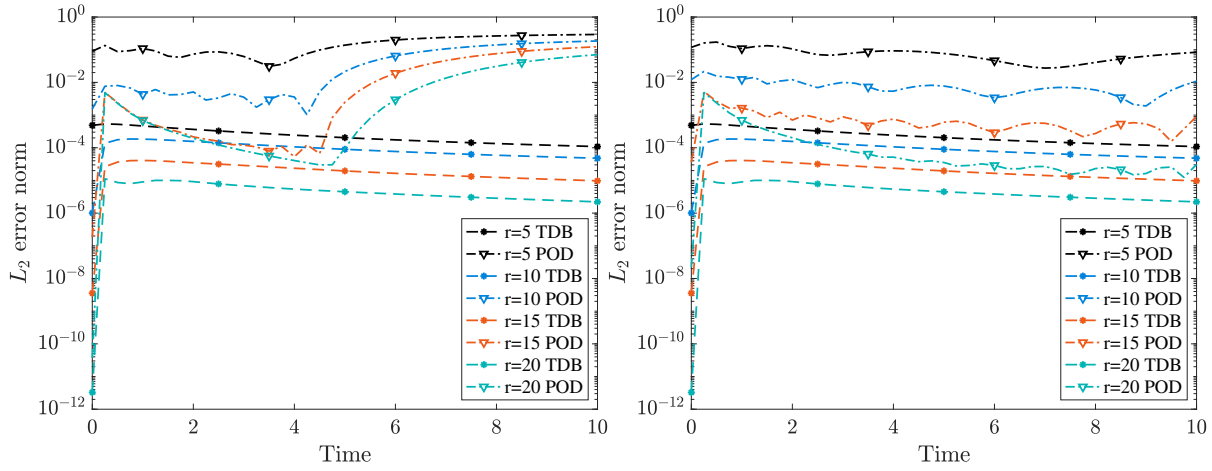

(a) $T_{observed} = 5.5$ (b) $T_{observed} = 11$

Figure 36: The above figure shows the reduction error vs time for four different reduction orders $r = 5, 10, 15, 20$. It is observed that as the reduction order increases the L_2 error of the solution decreases.

5.3.3 Asymmetric Vortex Dipole

In this case, we demonstrate the ability of the method for solving incompressible Navier-Stokes equations and the property of the modes to adapt according to the evolution of the flow-field. We also demonstrate the advantage of using time-dependent basis over static basis

obtained from Proper Orthogonal Decomposition (POD). Due to the localized nature of the vortices in the domain at any given time instant, static basis need to observe the solution for all time steps to obtain the appropriate basis. Static basis are unable to extrapolate the solution based on a few observations. The POD solution in this example is shown for two cases: (i) *POD basis are extracted form solution at a few time steps* (ii) *POD basis are extracted from solution at all time steps.* We also study the error convergence properties of the two methods with different reduction orders.

5.3.4 Problem Statement

A periodic two dimensional domain is considered with $L_{x_1} = L_{x_2} = 1$. $\omega(x_1, x_2, t)$ is the scalar vorticity field in the x_3 direction and $\psi(x_1, x_2, t, t)$ is the streamfunction whose evolution is given by the vorticity-streamfunction equations,

$$\frac{\partial \omega}{\partial t} + v_1 \frac{\partial \omega}{\partial x_1} + v_2 \frac{\partial \omega}{\partial x_2} = \frac{1}{Re}\left(\frac{\partial^2 \omega}{\partial x_1^2} + \frac{\partial^2 \omega}{\partial x_2^2}\right)$$
$$\nabla^2 \psi = -\omega$$

Here Re denotes the Reynolds number which is taken to be 2000. The streamfunction is used to compute the velocities in the x_1 and x_2 directions i.e., v_1 and v_2 using the following equations,

$$v_1 = \frac{\partial \psi}{\partial x_2}, \qquad v_2 = -\frac{\partial \psi}{\partial x_1}.$$

We use the TDB formulation to solve for the vorticity equation using the decomposition,

$$\omega(x_1, x_2, t) = u_i^{(1)}(x_1, t)\mathbf{T}_{ij}(t)u_j^{(2)}(x_2, t).$$

5.3.5 Computational Details

At $t = 0$, we consider two vortices with Gaussian vorticity profile and opposite circulation. The vorticity at $t = 0$ is taken to be superposition of two vortices given by,

$$\omega(x_1, x_2, t = 0) = \frac{\Gamma_1}{\pi r_1^2} \exp\left(-\frac{(x_1 - 0.1)^2 + (x_2 - 0.4)^2}{r_1^2}\right) + \frac{\Gamma_2}{\pi r_2^2} \exp\left(-\frac{(x_1 - 0.1)^2 + (x_2 - 0.6)^2}{r_2^2}\right).$$

Here we take, $\Gamma_1 = -\pi/20$, $\Gamma_2 = -1.1\Gamma_1$ $r_1^2 = r_2^2 = 1/1000$. The strength of Γ_2 is 1.1 times in strength of Γ_1 which induces asymmetry to the solution as the vortex dipole evolves. The vorticity at $t = 0$ is shown in Fig.(37). We discretize the space with 256 Fourier spectral modes in both x_1 and x_2 directions. The fourth order Runge-Kutta method is used for evolving the system in time with $\Delta t = 0.0005$. The system is evolved till $T_{final} = 11$. For the TDB solution, we evolve the equations till $T_i = 1$ using the DNS evolution equations. At $t = T_i$, the singular values decomposition of the DNS solution is taken and the eigenvectors are used to initialize the TDB in the x_1 and x_2 direction. Similarly, the $\mathbf{T}$ matrix is initialized using the singular values. For $t > 1$, the TDB formulation is used for the evolution of the vorticity equation. The streamfunction at every step for both methods is computed by taking the inverse of the Laplacian computed in the 2D Fourier transformed space,

$$\hat{\psi} = -\left(\nabla^2\right)^{-1} \hat{\omega}.$$

For the POD solution, the system is initialized for the coefficients of the POD modes at $T_i = 1$ using the DNS solution. The POD modes are obtained by taking eigenvectors of covariance matrix obtained by taking snapshots of the DNS solution till $T_{observed}$ at every 500th time step. The value of $T_{observed}$ taken for forming the POD modes for affects the accuracy of the solution. To demonstrate the effect of $T_{observed}$ on the solution, we take two cases: (i) $T_{observed} = 5.5$ (ii) $T_{observed} = 11$. The POD modes for both the cases are shown in Fig.(38). The first row shows the shape of the modes for $T_{observed} = 5.5$. The second row shows the shape of the modes for $T_{observed} = 11$. The first column shows the mean of the snapshots for the respective cases. column 2,3 and 4 show the structure of the modes in order of decreasing energy. The modes in row 2 can be seen to extend to more area as comapred to the modes in row 1, since that has been exposed to more snapshots of the solution.

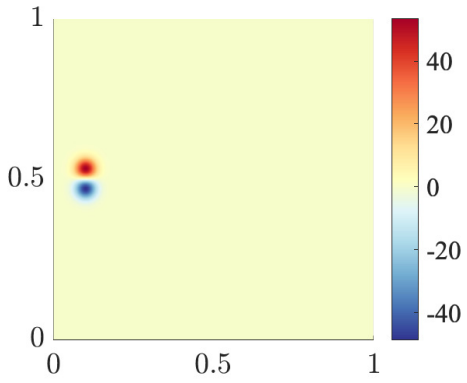

Figure 37: The initial condition for the vorticity is shown in the figure above. The vortex centers lie at $(0.1, 0.47)$ and $(0.1, 0.53)$. The vortex at the bottom has strength which is -1.1 times the strength of the vortex at the top. Due to this difference in the strength of the vortices, we expect the evolution of the flow field to be asymmetric.

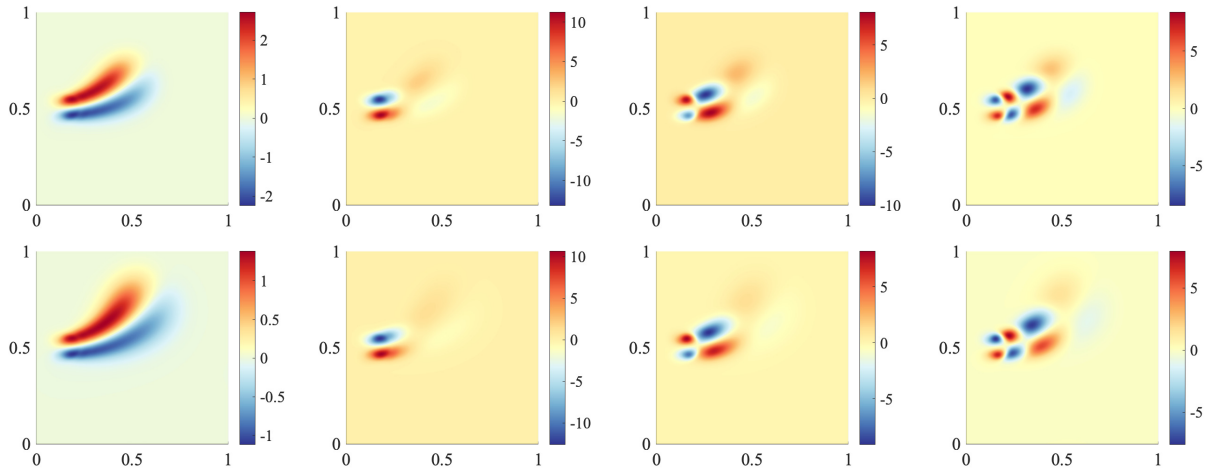

Figure 38: The figure shows the structure of the POD modes for the two cases. The first row shows the shape of the modes for $T_{observed} = 5.5$. The second row shows the shape of the modes for $T_{observed} = 11$. The first column shows the mean of the snapshots taken. Column 2,3 and 4 show the modes in the order of decreasing energy. We observe that the modes in row 2, occupy more area as compared to the modes in row 1 due to the increase in the time for which the solution is observed.

The evolution of the vorticity flow field as time evolves is shown in Fig.(39) for the TDB solution. The two vortices induce velocity in x_1 direction on each other and the vortices convect towards right as seen at $t = 4, 6, 8, 10$. Due to the unequal strength of the vortices we also observe a drift of the vortices upwards. Along with convection, we also observe that the vortices diffuse as seen with the increasing area of the vortices and decreasing strength of the vorticity field. Fig.(40) and Fig.(41 show the evolution of the vorticity solution with the POD modes. The POD modes are constructed based on snapshots of a reference solution. Since the snapshots of the reference solution are taken till $T_{observed} = 5.5$ for Fig.(40), the vortices in the figure show distortion for $t > 6$. Extrapolation of the solution is one of the drawbacks of the POD method. Extrapolation and the localized nature of the solution cause the flow field to incorrectly evolve beyond $T_{observed}$. Fig.(42) shows the evolution of the

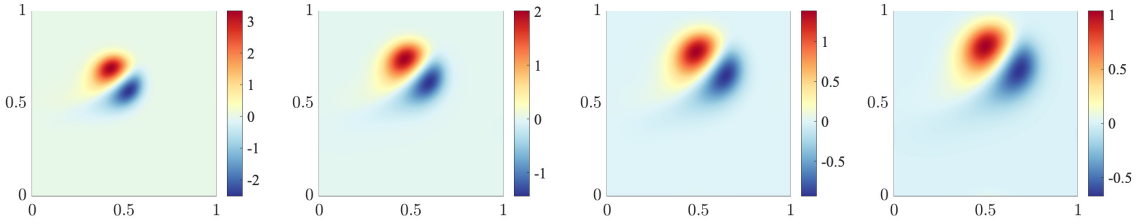

(a) $t = 4$ (b) $t = 6$ (c) $t = 8$ (d) $t = 10$

Figure 39: The evolution of the flow field of the vortex dipole is shown in the figure above. We observe that the dipole convects to the right as time evolves and diffuses. Due to asymmetry in the strength of the vortices, we also observe an upwards drift of the vortices.

first two time dependent modes at $t = 2, 4, 6, 8, 10$. The first row shows the evolution of the modes in the x_1 direction. It is observed that as the vortex convects to the right the localized time dependent mode convects to the right as well. We also observe the decreasing strength of the vortices as seen in the reduction of the amplitude of the first and second modes as time evolves. The second row shows the evolution of the modes in the x_2 direction. We observe a change in the amplitude of the modes due to diffusion as time progresses. Due to unequal vortex strength we also observe a drift of the inflection point of the modes in the positive x_2 direction.

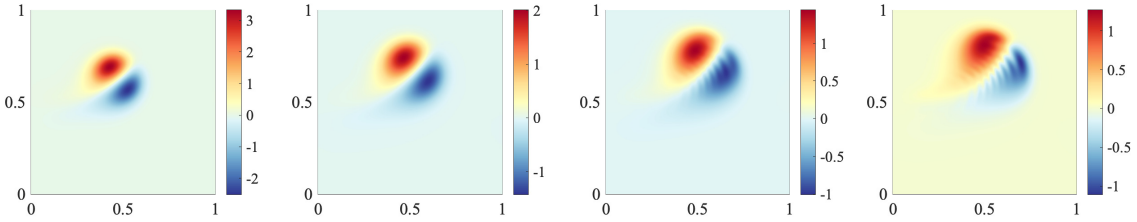

(a) $t = 4$ (b) $t = 6$ (c) $t = 8$ (d) $t = 10$

Figure 40: The solution obtained from POD for the case where $T_{observed} = 5.5$ is shown in the figure above. Since, the POD modes were exposed to the evolution of the vortex till $t = 5.5$, the solution till $t = 6$, is observed to be correct. However, the vortices for $t = 8, 10$ show distortion.

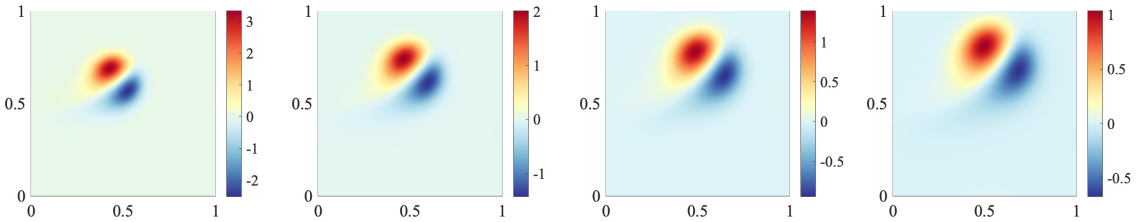

(a) $t = 4$ (b) $t = 6$ (c) $t = 8$ (d) $t = 10$

Figure 41: The solution obtained from POD for the case where $T_{observed} = 11$ is shown in the figure above. In this case, since the POD modes were exposed to the evolution of the vortex till $t = 11$, the solution is observed to match the DNS solution for all time steps. No vortex distortion is observed.

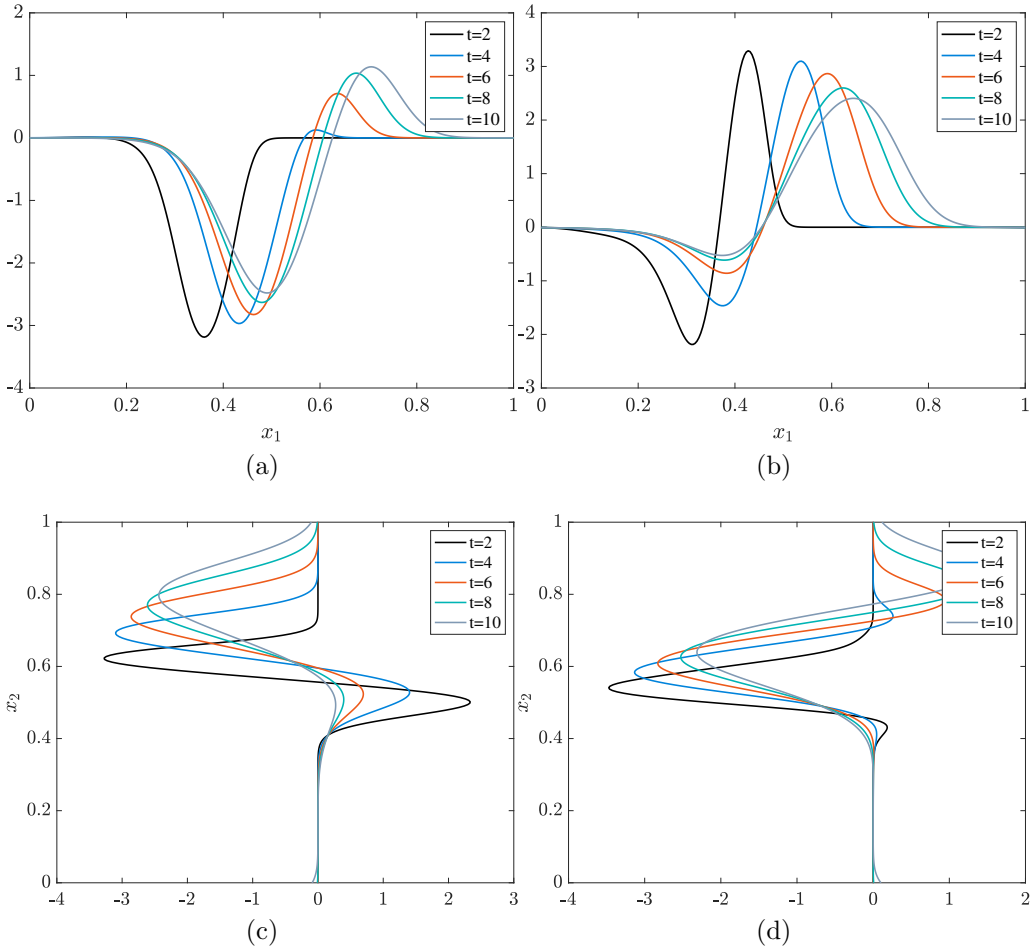

Figure 42: The above figure shows the evolution of the first mode in the x_1 and x_2 direction as time is evolved. As the vortex convects along the x_1 direction we observe that the first mode evolves along x_1. We also observe the drift in the x_2 direction due to unequal vortex strength.

We perform the analysis of the time-dependent basis for three different reduction orders $r = 5, 10, 15, 20$. The evolution of the error is plotted in Fig.(43) for both POD and TDB solution. The figure on the left shows the comparison of error for TDB solution with the POD case where $T_{observed} = 5.5$. We observe that TDB solution has an overall lower error as compared to POD. We also jump in the error beyond $T_{observed}$. The solution is not able to extrapolate the vorticity for $t > 5.5$. The figure on the right shows the error comparison for $T_{observed} = 11$. Since no extrapolation of the solution is performed the solution does not show a sudden jump in the error. The TDB solution shows a lower error than the POD solution for the same reduction order. For both the cases we observe that as the reduction order increases, the error decreases.

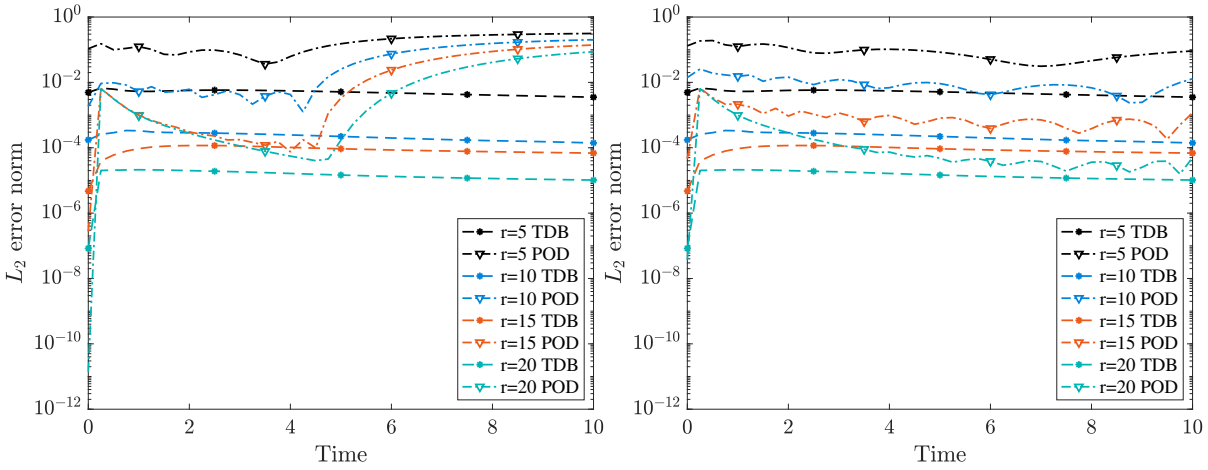

(a) $T_{observed} = 5.5$ (b) $T_{observed} = 11$

Figure 43: The above figure shows the reduction error vs time for four different reduction orders $r = 5, 10, 15, 20$. It is observed that as the reduction order increases the L_2 error of the solution decreases.

5.4 Compressible Flow Solver

In this section the capability of using time dependent basis is demonstrated for solving compressible Navier-Stokes cases. In the first case, we solve for a two dimensional temporally

evolving jet with periodic domain. The solutions obtained from the time dependent basis are compared with the results obtained from direct numerical simulations. The errors for different reduction orders are compared for both the time dependent basis and equivalent DNS.

5.4.1 2D Temporally Evolving Jet

This case demonstrates the application of the DBO method for solving the two-dimensional compressible Navier-Stokes equations for a temporally evolving jet. The schematic of the problem is given in Fig.(44). The domain is considered to be periodic in both stream-wise and cross-stream directions. The length of the domain is taken to be $2L$ and the height is taken to be L.

The primary variables considered here are, density $\rho(x_1, x_2, t)$, velocity vector $\mathbf{v}(\mathbf{x}, t) =$

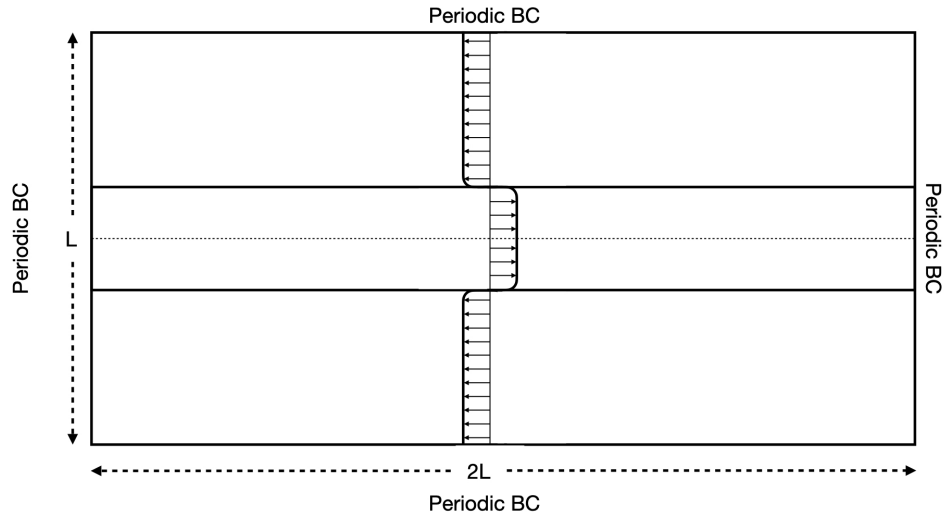

Figure 44: The schematic of the temporally evolving jet is shown in the figure above. The domain is considered periodic in both stream-wise and cross-stream directions.

$[v_1(x_1, x_2, t), v_2(x_1, x_2, t)]$, pressure $p(x_1, x_2, t)$, total energy $E_t(x_1, x_2, t)$ and temperature $T(x_1, x_2, t)$. The equations for the evolution of the variables are given by,

$$\frac{\partial \mathbf{V}}{\partial t} + \frac{\partial \mathbf{E}}{\partial x_1} + \frac{\partial \mathbf{F}}{\partial x_2} = 0, \tag{5.19}$$

where $\mathbf{U}, \mathbf{E}, \mathbf{F}$ are the vectors given by,

$$\mathbf{V} = \begin{bmatrix} \rho \\ \rho v_1 \\ \rho v_2 \\ E_t \end{bmatrix}, \mathbf{E} = \begin{bmatrix} \rho v_1 \\ \rho v_1^2 + p - \tau_{11} \\ \rho v_1 v_2 - \tau_{12} \\ (E_t + p)v_1 - v_1\tau_{11} - v_2\tau_{12} + q_1 \end{bmatrix}, \mathbf{F} = \begin{bmatrix} \rho v_2 \\ \rho v_1 v_2 - \tau_{12} \\ \rho v_2^2 + p - \tau_{22} \\ (E_t + p)v_2 - v_1\tau_{12} - v_2\tau_{22} + q_2 \end{bmatrix}.$$

Here E_t is the total energy per unit volume and e is the internal energy per unit mass. τ_{ij} represents the components of viscous stress tensor and q_i are the heat flux vectors. Further details about the computations and initial conditions are given in Appendix E.

The time dependent basis decomposition is employed for the $\rho, \rho v_1, \rho v_2$ and E_t variables in the following manner,

$$\rho(x_1, x_2, t) = \sum_{j=1}^{r} \sum_{i=1}^{r} \rho_{2i}(x_2, t)\Sigma_{\rho_{ij}}(t)\rho_{1j}(x_1, t).$$

We investigate how well the evolution of the vortices in the jet flow are captured by the time dependent basis formulation by comparing the results to a fully resolved DNS. The fully resolved DNS is computed on a grid of size 896×896. In addition, the solution obtained from time dependent basis for different reduction orders is compared to an equivalent DNS where the degrees of freedom for the two methods are taken to be same. The equivalent DNS or referred to as URDNS (under-resolved DNS) in the subsequent text is computed as,

$$N_{URDNS}^2 = 2rN_{DNS} + r^2.$$

The N_{DNS} in this case is taken to the resolution of the grid in the x_1 and x_2 directions from the DNS simulation, which in this case is taken to be 896. Table.(**??**) shows the values of the URDNS grid for different reduction orders.

The results obtained from TDB are compared against the results obtained from DNS and URDNS. Fig.(45) shows the comparison for the results for the density field. The results are compared for three different time snapshots, $t = 2, 4$ and 6 for TDB and equivalent URDNS grids. It is observed that the TDB solution for reduction order $r = 40$ and its equivalent URDNS 272×272 show the flow field matching the DNS solution. However for TDB $r = 30$ and $r = 25$, the equivalent URDNS 232×232 and 212×212 show divergence

Table 4: The table shows the size of the URDNS grid i.e, N_{URDNS} for different TDB reduction orders (r).

Reduction order(r)	N_{URDNS}
25	212
30	232
40	272
50	304

after 4 Time Units. The build-up in the error due to aliasing can be seen in the solution of URDNS 212×212 along $x_2 = 0.5$ center line. This error buildup in the solution results in the divergence of the solution at $t = 6$ for URDNS.

The TDB solution on the other hand, is not susceptible to this aliasing and shows the flow field matching with the structures visualized in the DNS solution. However, the error depends on the number of modes resolved or the reduction order of the solution (denoted by r in these cases). The error caused by ignoring the higher modes in the solution can be visualized in the TDb solution for $r = 25$ for $t = 4$ and 6. For $t = 2$, as the solution has a lower number of modes $r = 25$ is able to resolve the solution accurately. As the system evolves, the lower modes of the system gain energy the error in the solution in much more visible as seen at $t = 4$ and 6. We can observe salt and pepper type error in the solution as compared to the DNS solution.

A comparison between the singular values obtained from instantaneous SVD of DNS solution and TDB solution (Σ_ρ) for density is shown in Fig.(47). The figure shows the error incurred in the solution for lower reduction orders $r = 20, 30$. This is the cause of the salt and pepper error mentioned in the previous figure. For $r = 20$ and 30 while the lower singular values (higher energy) are captured accurately we observe large errors in the higher singular values (lower energy) as can be observed from large deviations between those modes and their

DNS counterparts. For $r = 40$ and 50 as more higher modes (lower energy) are resolved, the errors will reduce and we observe that the accuracy of the lower singular modes is also improved. The improvement in the accuracy of the singular value (Σ_{20}) as reduction order is increased is seen in row 3 of Fig.(47). Fig.(48) shows a comparison between the density spectrum obtained for reduction order $r = 50$, DNS solution for grid size 896×896 and URDNS solution for grid of size 304×304. The spectrum is plotted for three different time units: $t = 2, 4$ and 6. At $t = 2$ the spectrum extends till 10^{-15}. The TDB solution is able to capture the spectrum accurately. However, the URDNS solution only captures the spectrum till values up to 10^{-7}. Due to the under resolved grid, the lower values are not captured. While these errors are small ($\mathcal{O}(10^{-6})$, the URDNS also has difficult capturing the values of the lower wavenumbers. The errors introduced in capturing the lower wavenumbers introduce higher inaccuracy than that in capturing the higher wavenumbers. At $t = 4$, we observe that the spectrum is captured correctly by the TDB solution and the errors in the URDNS solution come from under resolution of the grid and inaccuracies in capturing lower wavenumbers. At $t = 6$, we now observe an error in the TDB solution for the higher wavenumbers. This error in capturing the higher wavenumbers can be attributed to fact that more reduction orders are required to accurately capture the lower energy (high wavenumber) modes. As the system evolves beyond $t > 4$, the modes with negligible energy ($r > 50$) at the beginning of the simulation start gaining energy and need to be resolved to keep the errors low.

A similar density spectrum comparison is shown for three reduction orders $r = 30, 40, 50$ with DNS spectrum in Fig.(49). This figure shows the behaviour of the spectrum for different reduction orders. The behaviour of the spectrum depends on the energy of the modes in the unresolved modes. At $t = 2$, we observe that since the unresolved modes have low energy the spectrum is correctly resolved by all the reduction orders. At $t = 4$ modes $20 < r < 50$ gain energy and are no longer negligible. Hence, the spectrum obtained for $r = 20, 30$ show higher deviation from the DNS spectrum. Since, $r = 50$ accurately resolves the modes up to the fiftieth mode; the spectrum for reduction order 50 follows the DNS spectrum. At $t = 6$, modes $r > 50$ start to gain energy and hence we now observe a deviation of reduction order 50 from the DNS spectrum.

An important quality of the time dependent modes is the adaptivity of the modes to the evolution of the flow field. Figs.(50,51,52) demonstrate this property of the time dependent modes. In Fig.(50) the evolution of the first three modes in x_1 and x_2 directions are shown at $t = 2, 4, 6$. The modes in the x_1 direction follow the evolution and merging of the vortices. The modes obtained in the x_2 direction can be seen to be following the width of the jet. As time evolves and the jet widens the modes in the x_2 direction evolve to reflect this change. The evolution of the first mode in the x_2 direction is shown in Fig.(51). The width of the jet widens as the flow evolves and the vortices in the flow merge together. Fig.(52) shows the evolution of the second mode in the x_1 direction. As the flow evolves the seemingly sinusoidal-type structure of the mode is disrupted as the vortices merge for $t > 4$.

Finally, the errors in the TDB solution for different reduction orders is plotted in Fig.(53). It is observed that as the reduction order increases i.e., more lower energy modes are resolved, the errors reduce. The reduction in the errors is a property of the singular values spectrum and the number of modes resolved at a particular time. The L_2 error norm is computed by taking the Frobenius norm of the difference in the solution between the DNS and the TDB solution.

5.4.2 3D Temporally Evolving Jet

This case demonstrates the application of the TDB method for solving the three-dimensional compressible Navier-Stokes equations for a temporally evolving jet. The schematic of the problem is given in Fig.(54). The domain is considered to be periodic in all three directions. The lenght of the domain in all three directions is taken to be L. The primary variables considered here are, density $\rho(x_1, x_2, x_3, t)$, velocity vector $\mathbf{v}(\mathbf{x}, t) = [v_1(x_1, x_2, x_3, t), v_2(x_1, x_2, x_3, t), v_3(x_1, x_2, x_3, t)]$, pressure $p(x_1, x_2, x_3, t)$, total energy $E_t(x_1, x_2, x_3, t)$ and temperature $T(x_1, x_2, x_3, t)$. The equations for the evolution of the primary variables are given by,

$$\frac{\partial \mathbf{V}}{\partial t} + \frac{\partial \mathbf{E}}{\partial x_1} + \frac{\partial \mathbf{F}}{\partial x_2} + \frac{\partial \mathbf{G}}{\partial x_3} = 0. \tag{5.20}$$

The definition the vectors $\mathbf{V}, \mathbf{E}, \mathbf{F}, \mathbf{G}$, computational details and initial conditions are given in Appendix E. We investigate how well the evolution of the vortices in the jet flow are

captured by the TDB formulation by comparing the results to a fully resolved DNS. The fully resolved DNS is computed on a grid of size $256 \times 256 \times 64$. In addition, the solution obtained from TDB for different reduction orders is compared to an equivalent DNS where the degrees of freedom for the two methods are taken to be same. The equivalent DNS or referred to as URDNS (under-resolved DNS) in the subsequent text and is computed as,

$$\frac{N^3_{URDNS}}{4} = N_{1_{DNS}} r_1 + N_{2_{DNS}} r_2 + N_{3_{DNS}} r_3 + r_1 r_2 r_3. \tag{5.21}$$

The $N_{1_{DNS}}, N_{2_{DNS}}$ in this case is taken to the resolution of the grid in the x_1 and x_2 direction from the DNS simulation, which in this case is taken to be 256. N_{3DNS} in this case is taken to be 64. Table.(**??**) shows the values of the URDNS grid for different reduction orders. Since the DNS solution is computed on a grid where $N_3 = N_1/4$, the URDNS computed in Eq.(5.21) also follows the same criterion. The x_2 direction requires a large number of modes for correct resolution, hence the reduction order study is done by increasing the number of modes in the x_2 direction i.e., r_2. For constant $(r_1, r_3) = (30, 30)$, we consider three different reduction orders for $r_3 = (20, 40, 60)$.

The results obtained from TDB are compared against the results obtained from the DNS and URDNS. Fig.(55) shows the comparison for the results of the density field with slices taken in the x_3 direction at (0.1,0.5,0.9). The results are compared for three different time snapshots at $t = 5, 7$ and 9. It is observed that the TDB solution for reduction orders $r_2 = 40, 60$ match the DNS solution. Whereas the URDNS solution for both these cases i.e., $69 \times 69 \times 19$ and $62 \times 62 \times 17$ show large deviation from the DNS solution. The URDNS solution for $43 \times 43 \times 11$ diverges for $t > 5$. The advantages of using the time dependent basis is visible in the 3D simulations where the TDB is able to capture the flow field correctly whereas the equivalent DNS struggles with capturing even the larger wavenumbers in the flow correctly.

The source of the errors in the solution of the time dependent basis formulation is the unresolved modes in the system and the accuracy of each of the resolved singular values. Fig.(57) shows the evolution of the resolved singular values obtained from TDB solution. The singular values are compared with the instantaneous SVD of the solution at each time step. The singular values are computed for the density field unfolded along the x_2 direction.

Due to the clustering of the singular values, the figures show the singular values with every second singular value skipped while plotting. The plot on the right in row 2 shows the errors incurred in the computation of the singular values for the different reduction orders. It is observed that the errors in the computation of the singular values reduce as more modes are added to the TDB decomposition. As more modes are added in the system the error from the unresolved modes can be controlled as well.

Fig.(58) shows the error in the solution due to unresolved modes. The error is taken to be the sum of the unresolved singular values for different reduction orders of the DNS solution. As more modes are added to the system the error from the unresolved modes is reduced. This method is efficient in capturing systems where the first few modes capture 99% of the total energy of the system.

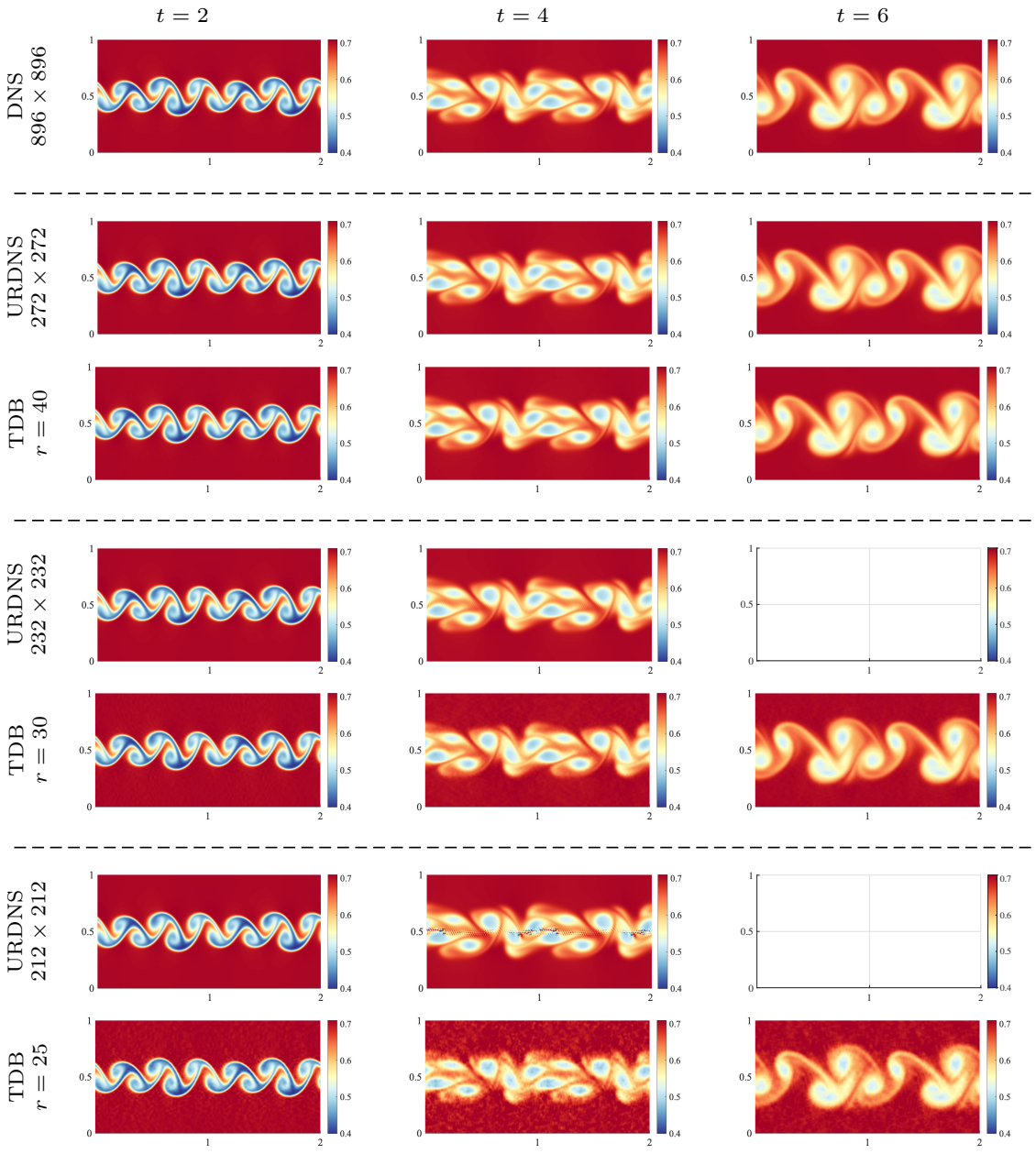

Figure 45: The above figure shows the density flow field at $t = 2, 4$ and 6 for TDB and equivalent URDNS. We observe that for TDB ($r = 40$) and it equivalent URDNS 272 show the flow field matching the DNS 896. However for TDB $r = 30$ and $r = 25$ the equivalent URDNS 212 and 232 show divergence after 4 Time Units. The TDB solution for $r = 25$, also shows error in the capturing the higher modes as can be seen in the solution at $t = 4$. The build up in the error in the URDNS due to aliasing can be seen in the solution of URDNS 212×212 along the $x_2 = 0.5$ center line.

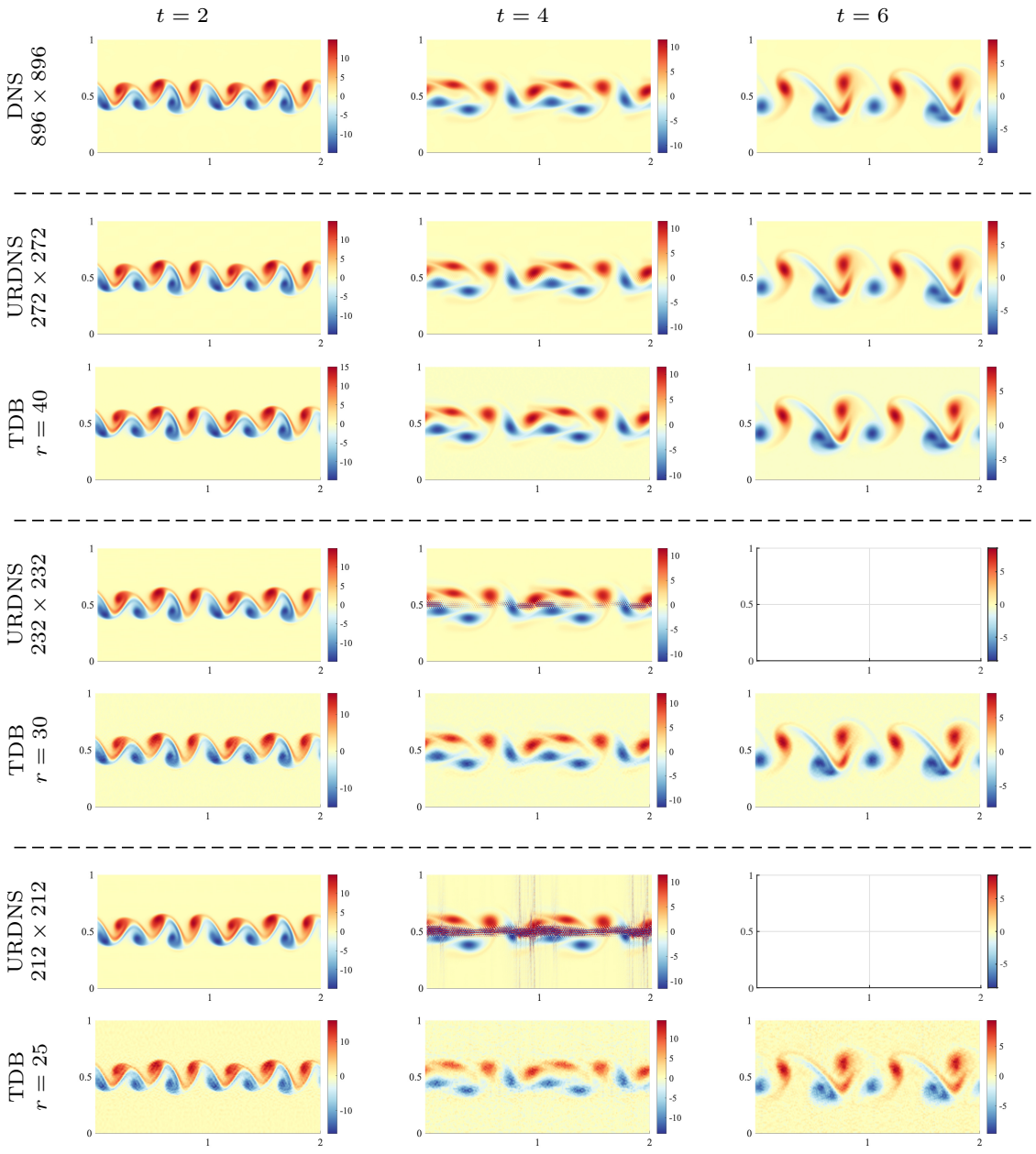

Figure 46: The above figure shows the vorticity flow field at $t = 2, 4$ and 6 for DBO and equivalent URDNS. We observe that for DBO ($r = 40$) and its equivalent URDNS 272 show the flow field matching the DNS 896. However for DBO $r = 30$ and $r = 25$ the equivalent URDNS 212 and 232, show divergence after 4 Time Units. The DBO solution for $r = 25$, also shows error in the capturing the higher modes as can be seen in the solution at $t = 4$. The build up in the error in the URDNS due to aliasing error can be seen in the solution of URDNS 212 along the $x_2 = 0.5$ centerline.

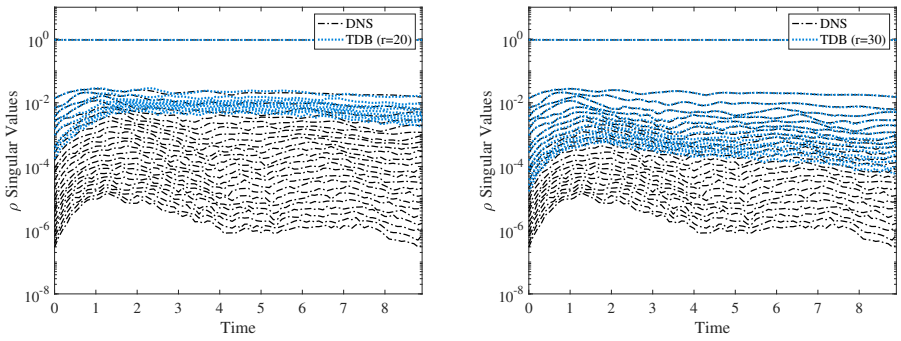

(a) $r = 20$

(b) $r = 30$

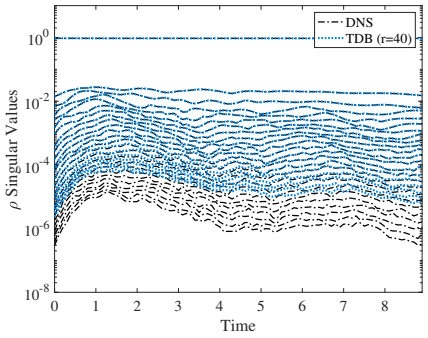

(c) $r = 40$

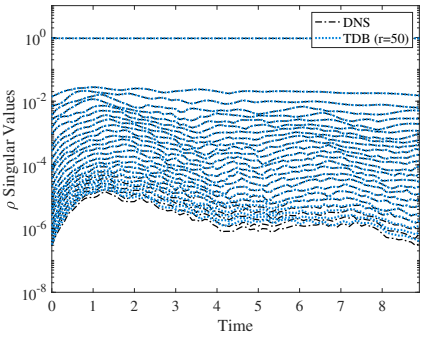

(d) $r = 50$

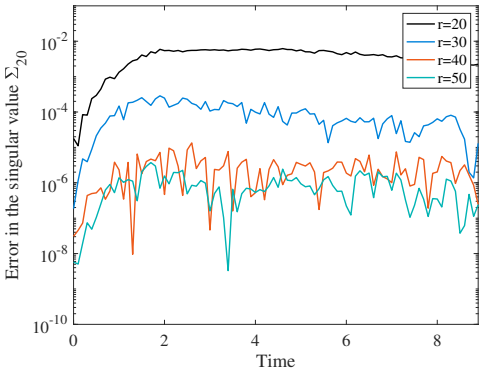

(e) Errors in singular values

Figure 47: The comparison of singular values for density is shown for different reduction orders with the singular values obtained from the instantaneous SVD of the flow-field. *Due to the clustering of the singular values, the figures in row 1 and 2 show the singular values with every second singular value skipped while plotting.* Row 1 and 2 show the comparison between the singular values for $r = 20, 30, 40, 50$. Row 3 depicts the error in the singular value Σ_{20} for different reduction orders. It is observed that for lower reduction orders the accuracy of the the singular value is low. As more modes are added to the system the accuracy of the singular value is improved.

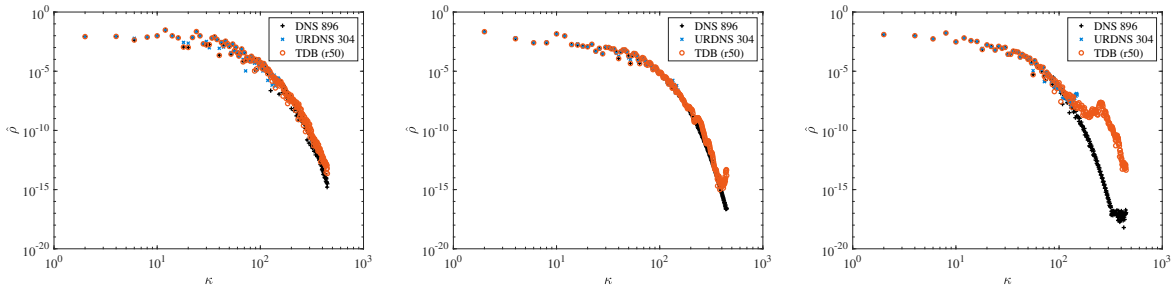

(a) $t = 2$ (b) $t = 4$ (c) $t = 6$

Figure 48: The above figure shows the spectrum for the density at $x_2 = 0.5$ for TDB ($r = 50$) and its equivalent URDNS 304. The spectrum for DNS 896 is plotted for reference. The spectrums are shown for three different time steps: $t = 2, 4$ and 6. It can be observed that while the errors in the TDB can be attributed to the incorrect capturing of the smaller scale structures, the errors in URDNS arise from the aliasing errors due to deficit in the grid resolution. Both the methods capture the large scale structures in the flow properly as can be seen in the spectrum match for wavenumbers $\kappa < 50$ for both URDNS and TDB.

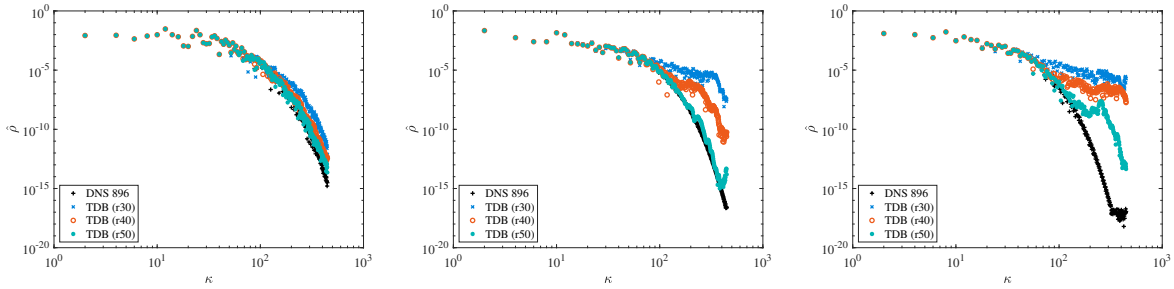

(a) $t = 2$ (b) $t = 4$ (c) $t = 6$

Figure 49: The above figure shows the density spectrum for TDB with different reduction sizes: $r = 30, 40, 50$. The DNS spectrum is also plotted for comparison. The spectrum is shown for three time units: $t = 2, 4, 6$. We observe that the spectrum improves as the reduction size is increased. All the reduction sizes capture the larger scale structures in the flow correctly as seen in the match of the $\kappa < 50$.

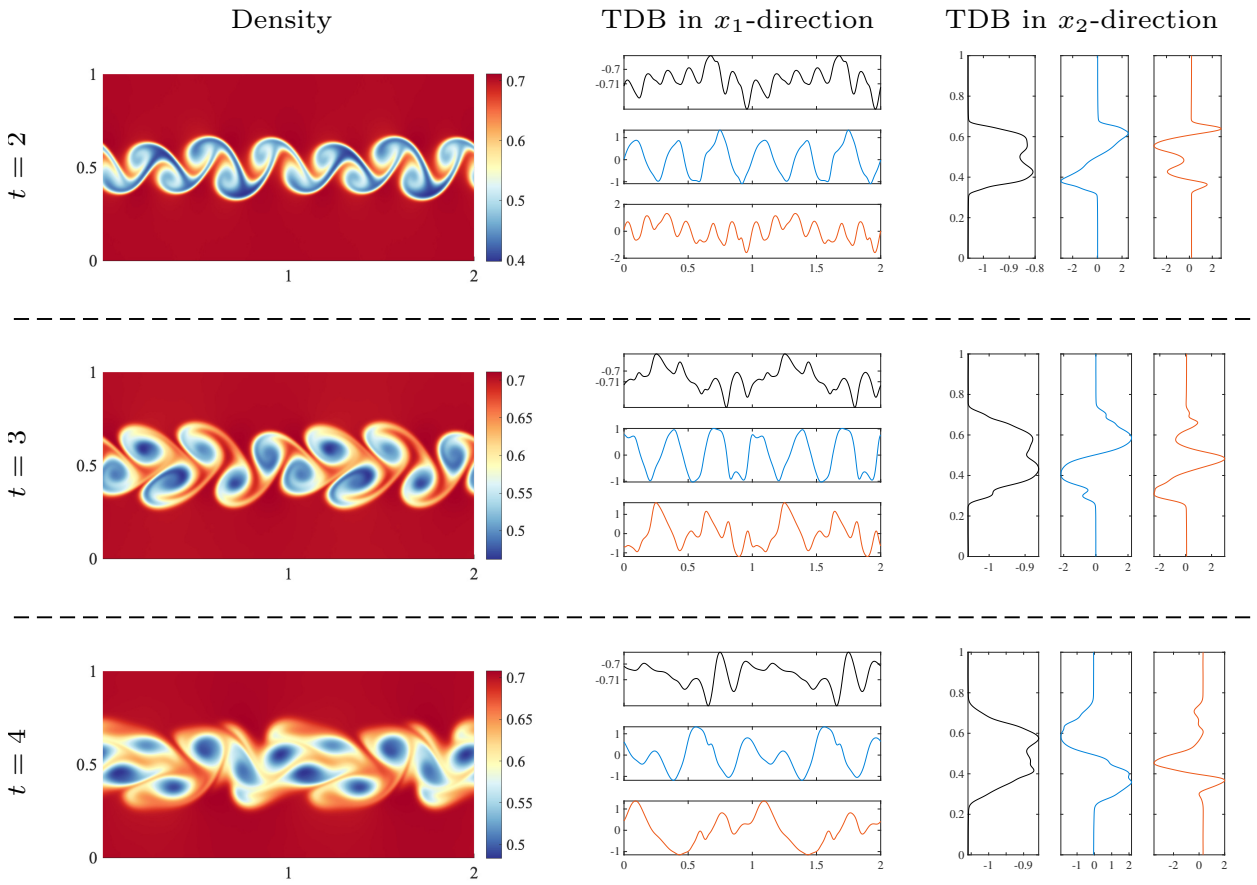

Figure 50: The above figure shows the shape of the first 3 modes at $t = 2, 3$ and 4. The shape of the modes adapts to the evolution of the flow field. For example, we observe the shape of the first mode in x_2-direction changes as the width of the jet increases. This width change in the shape of the jet is reflected in the shape of the first three x_2-modes.

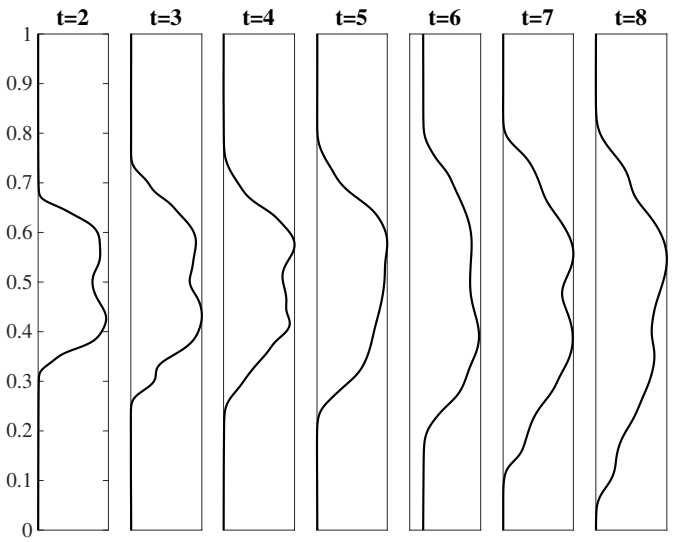

Figure 51: The above figure shows the evolution of the shape of the first x_2-mode according to the evolution of the flow field. The first mode increases in width with the evolution of the jet.

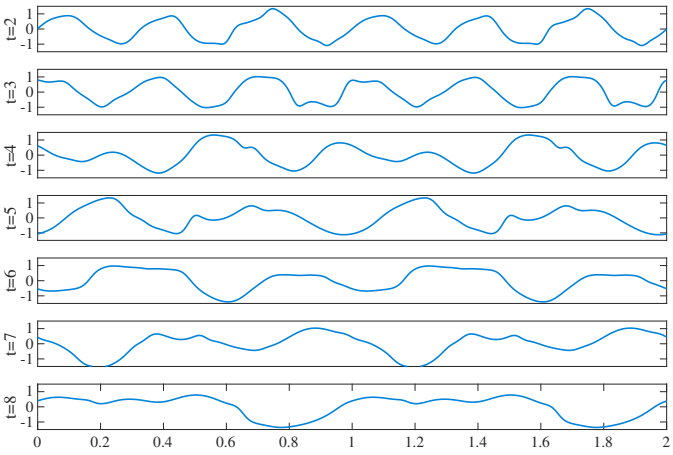

Figure 52: The above figure shows the evolution of the shape of the second x_1-mode according to the evolution of the flow field. As the vortices evolve and merge the seemingly sinusoidal-type structure of the mode is disrupted for $t > 4$.

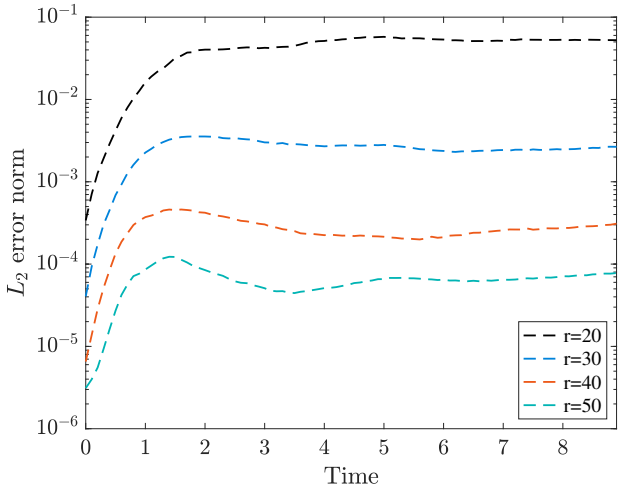

Figure 53: The above figure shows the L_2-error obtained from the DBO flow field and the DNS solution. The time-evolution of error for four different reduction orders i.e., $r = 20, 30, 40, 50$ is plotted. It is observed that as the reduction order i.e., the number of modes are increased the error is reduced.

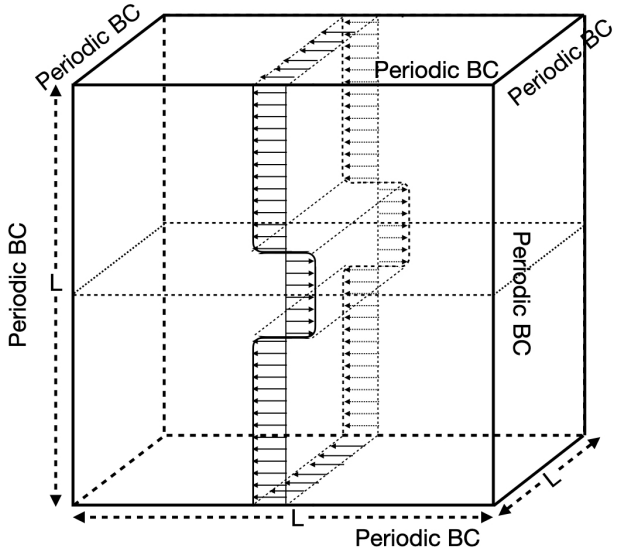

Figure 54: The schematic of the 3D temporally evolving jet is shown in the figure above. The domain is considered periodic in all the three directions.

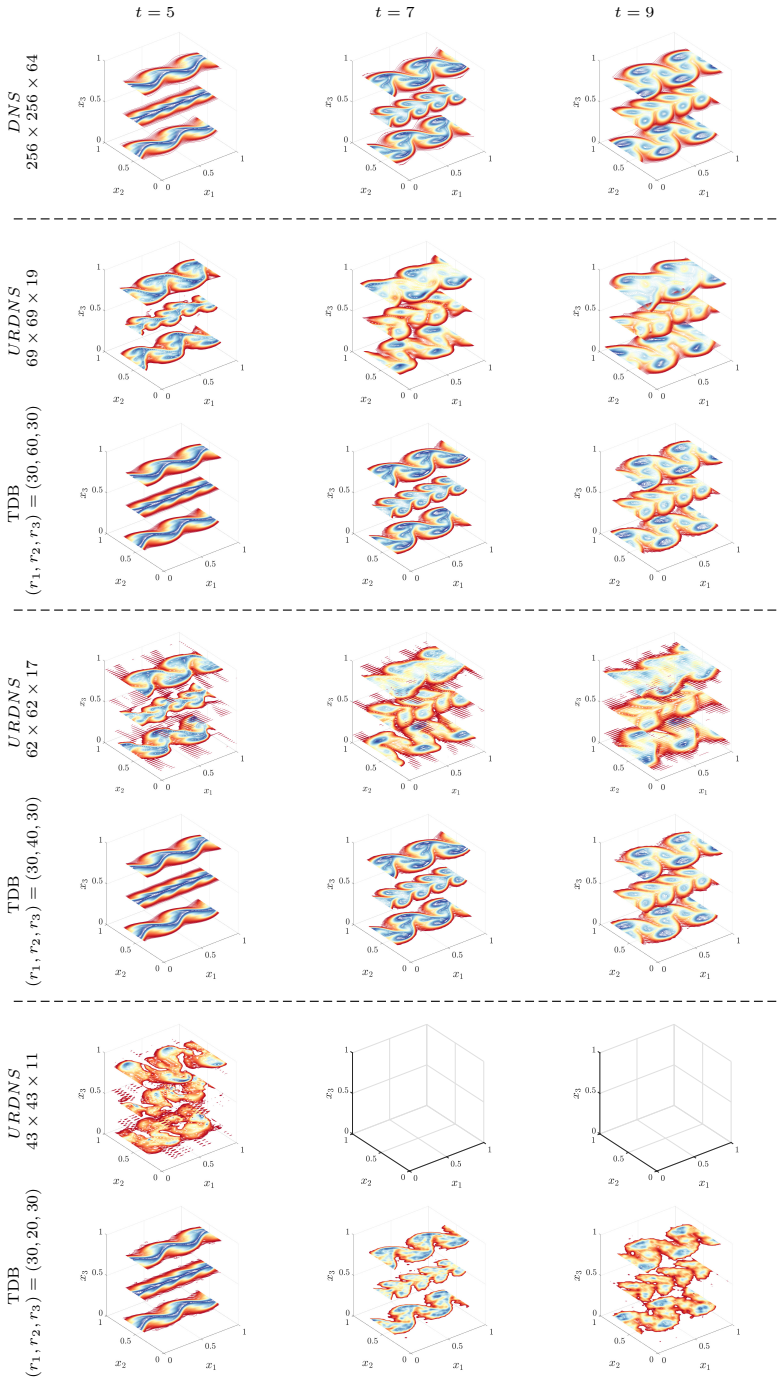

Figure 55: The above figure shows the density flow field at $t = 5, 7$ and 9 and $x_3 = (0.1, 0.5, 0.9)$. The results are shown for DBO simulations for three different reduction orders of r_2 which are $20, 40$ and 60. The top row shows the results for the DNS simulation for the grid size $256 \times 256 \times 64$.We observe that the flow field errors are reduced as the reduction order is increased in the x_2-direction. The under-resolved DNS results are not showed for comparison as all of those results diverge for the given reduction orders.

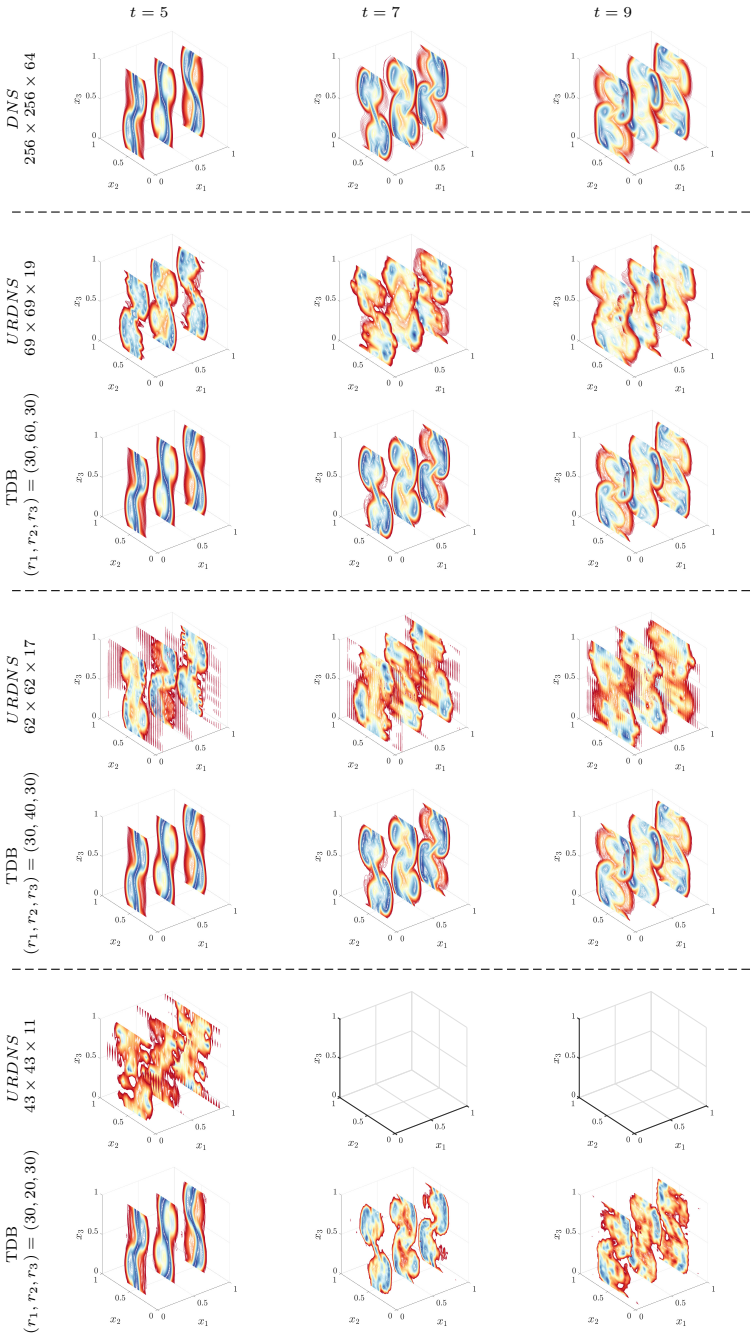

Figure 56: The above figure shows the density flow field at $t = 5, 7$ and 9 and $x_1 = (0.1, 0.5, 0.9)$. The results are shown for DBO simulations for three different reduction orders of r_2 which are $20, 40$ and 60 and their equivalent under-resolved DNS. The top row shows the results for the DNS simulation for the grid size $256 \times 256 \times 64$. We observe that the flow field errors are reduced as the reduction order is increased in the x_2-direction. The under-resolved DNS results are not showed for comparison as all of those results diverge for the given reduction orders.

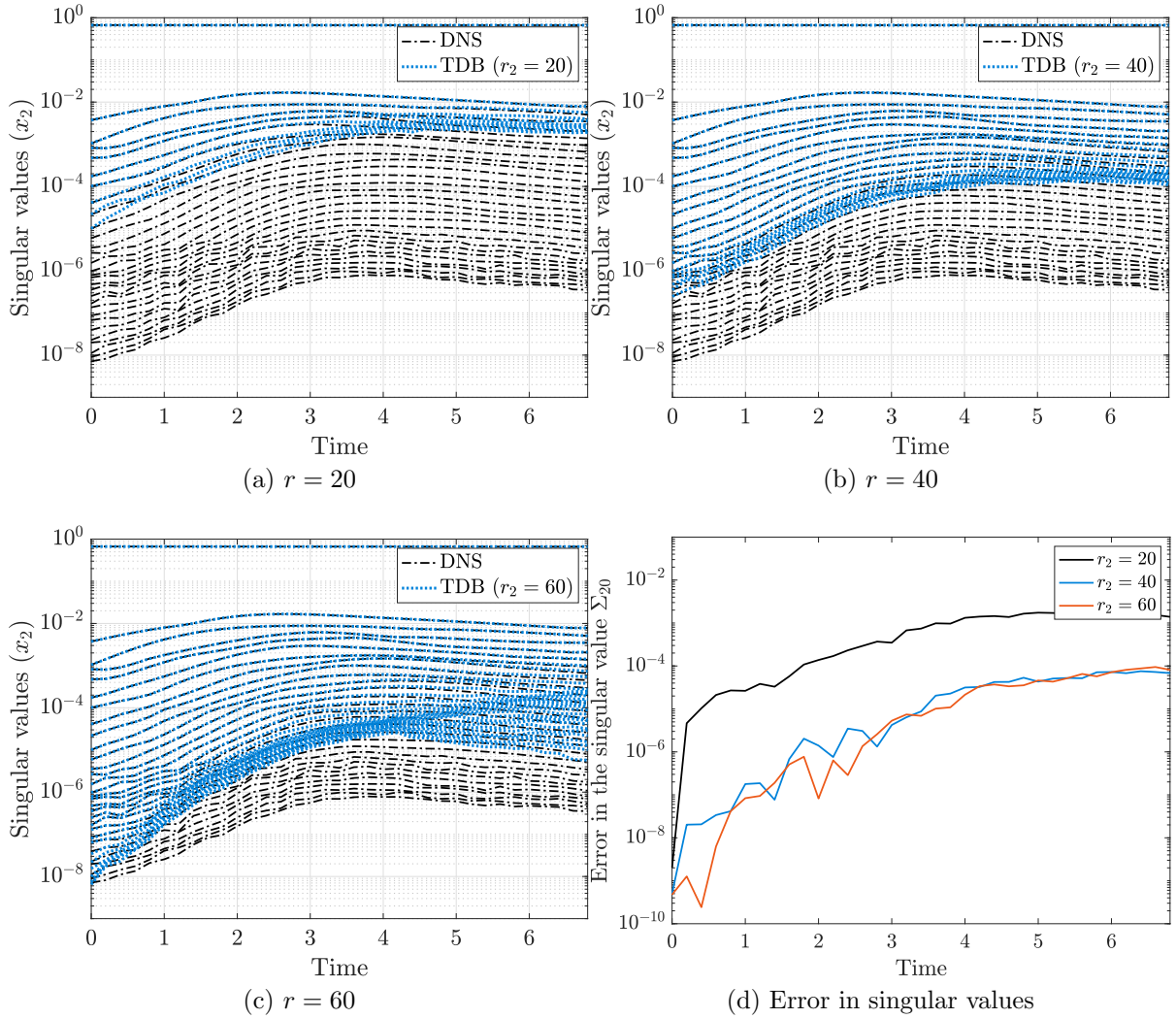

Figure 57: The above figure shows a comparison between the singular values obtained from the time dependent basis and the singular values obtained from instantaneous SVD values of the density flow field. *Due to the clustering of the singular values, the figures show the singular values with every second singular value skipped while plotting.* The values are plotted for three different reduction orders $r_2 = 20, 40, 60$. The accuracy of the singular values in x_2 direction improves as the reduction order is increased

Table 5: The table shows the size of the URDNS grid i.e, N_{URDNS} for different TDB reduction orders (r_1, r_2, r_3).

Reduction order(r_1, r_2, r_3)	$N_{1_{URDNS}}, N_{2_{URDNS}}, N_{3_{URDNS}}$
(30,20,20)	$43 \times 43 \times 11$
(30,40,30)	$62 \times 62 \times 17$
(30,60,30)	$69 \times 69 \times 19$

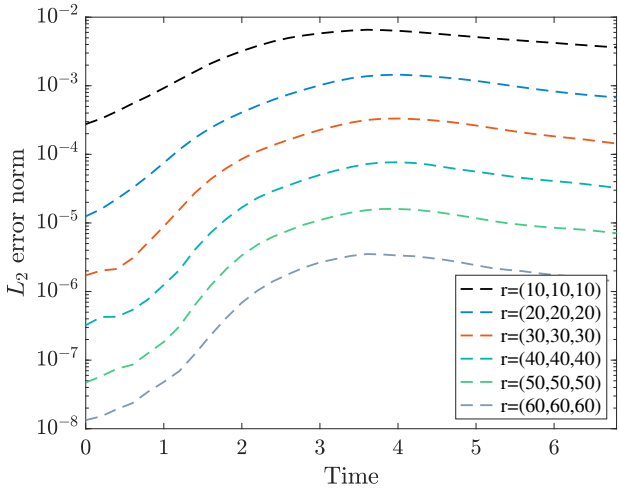

Figure 58: The above figure shows the L_2-error obtained from the DBO flow field and the DNS solution. The figure shows the time-evolution of error for different reduction orders. It is observed that as the reduction order i.e., the number of modes are increased the error is reduced.

6.0 Future Work

6.1 Stochastic Partial Differential Equations

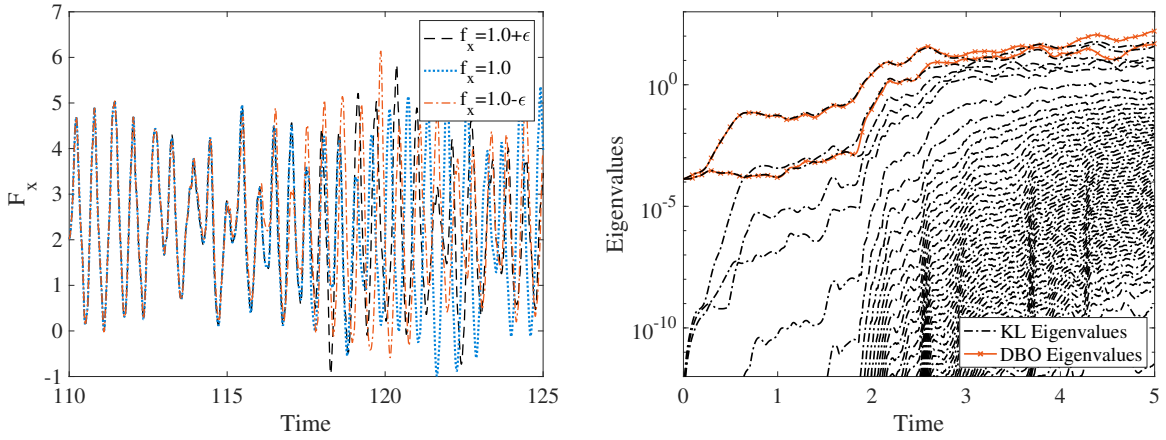

(a) Chaos test

(b) 2 Modes eigenvalue comparison

Figure 59: Dynamically bi-orthonormal decomposition for flow over a bump in a channel in chaotic regime: (a) The growth of the small perturbations in the forcing measured by the horizontal viscous shear force on the walls. The signals are observed to completely diverge after $t = 116$. (b) The growth in the eigenvalues of the DBO system with $r = 2$ and the eigenvalues of the Karhunen-Loéve decomposition.

We would like to show a limitation of the presented method for solving stochastic partial differential equations. In particular we revisit the demonstration case for stochastic Navier-Stokes equation as presented in Section 2.8.5.

We consider the same problem setup as the previous case of Reynolds number 1500 except that the kinematic viscosity is chosen to be $\nu = 0.015$ which changes the Reynolds number to $Re = 5000$. For this Reynolds number the flow is chaotic. To ensure that the flow is chaotic, we solved three deterministic cases by perturbing the horizontal forcing with three values $f_x = 1 - \epsilon, 1$ and $1 + \epsilon$ with $\epsilon = 10^{-3}$. The resulting shear viscous force in the x-direction on the top and bottom walls is plotted in Fig.(59a). It is clear that difference

between the three solutions due to the perturbation grows and after $t > 116$ becomes $\mathcal{O}(1)$ – verifying that the flow is chaotic. We consider DBO reduction with $r = 2$. The eigenvalues of the covariance of the DBO system and those of the KL decomposition are plotted in Fig.(59b). We observe that for the chaotic regime a fast decay of the eigenvalues is not observed, since the randomness in the initial condition quickly propagates on large number of independent dimensions in the phase space of the dynamical system due to strong nonlinear interaction between the modes and fast growth of small perturbations. As a result, the effect of unresolved modes must be accounted for.

6.2 Deterministic Partial Differential Equations

While the methodology shows a lot of promise in improving the computational cost for linear equation, compression ratio for saving data and structure resolving properties of the flow; the method has a major drawback in the initialization of the solution of the modes. Currently, the equations are evolved until a time $t = T_i$ called the initialization time, where we take SVD or HOSVD of the DNS solution to initialize the TDB components. The solution at $t = 0$ for most cases can be written as a single mode and lower modes in the system gain energy during the evolution of the system. Hence, it is difficult to initialize the lower modes of the system at $t = 0$. One solution to this problem is implementing adaptive modes strategy, where the lower modes i.e., $(r+1)^{th}$ mode can be initialized as the last mode i.e., r^{th} mode in the system passes a certain energy threshold. However, it is difficult to determine the initial direction of the mode which is orthogonal to the other modes currently in the system. Using this adaptive strategy can help in minimizing the errors in the solution due to unresolved modes during long term integration.

Another current major drawback of the the method is the computational cost for evaluating the nonlinear equations. We have demonstrated in the previous sections, the computational advantages of using the method for *compressed form* of linear equations as compared with the computational time for DNS solution. However, due to the expansion of the subspace for the nonlinear terms and the inability to obtain a cost effective reduced

order formulation for every nonlinearity withholds us from making the nonlinear equations computationally faster. Future work in this direction would address the computational cost which would make the method applicable to a larger set of problems.

As observed in the case of the temporally evolving jet, the method resolves the larger coherent structures in the flow. As we consider only a limited number of modes in the reduced order model, the smaller modes containing smaller structures in the flow and higher wavenumbers are ignored. It is necessary to consider the dissipative effects of these small scale structures on the time dependent modes and their evolution. Closure modeling studies have been carried out in the context of the POD method [91, 92, 93]. Preservation of the stability of these modes for long time integration and preventing the solution from drifting to erroneous states is necessary to improve the accuracy and efficacy of the TDB method.

7.0 Conclusions

In this work, we have presented a new real-time reduced order modeling methodology called the *dynamically bi-orthonormal* (DBO) decomposition for solving stochastic partial differential equations. The presented method approximates a random field by decomposing it to a set of time-dependent orthonormal spatial basis, a set of time-dependent orthonormal stochastic basis and a low-rank factorization of the covariance matrix. We derived closed form evolution equations for above components of the decomposition as well as the time-dependent mean field.

We show that the presented method is equivalent to the dynamically orthogonal and bi-orthonormal decompositions via an invertible matrix transformation. We derive evolution equations for these transformation matrices. Although DBO is equivalent to both DO and BO decompositions, it exhibits superior numerical performance especially in highly ill-conditioned systems. In both BO and DO decompositions, the condition number of covariance matrix, whether diagonal (BO) or full (DO), is $\lambda_{max}(t)/\lambda_{min}(t)$, where $\lambda_{min}(t)$ and $\lambda_{max}(t)$ are the smallest and largest eigenvalues of the covariance matrix, respectively. However, in the DBO decomposition, a factorization of the covariance matrix ($\Sigma(t)$) is inverted, and $\Sigma(t)$ has the condition number of $\sqrt{\lambda_{max}(t)/\lambda_{min}(t)}$. The improvement in the condition number of the DBO systems compared with BO or DO is important for adaptive reduced order modeling as the newly added or removed mode has very small eigenvalues. The DBO decomposition tolerates significantly smaller eigenvalues compared to BO and DO without degrading the accuracy. Moreover, in comparison with BO, DBO does not become singular in the case of eigenvalue crossing, and in comparison with DO, the DBO stochastic coefficients are orthonormal, resulting in better-conditioned representation of the stochastic subspace compared to that of DO.

We demonstrated the DBO decomposition for several benchmark SPDEs: (i) linear advection equation, (ii) Burgers' equation with manufactured solution, (iii) Burgers' equation with stochastic forcing, (iv) and Burgers' equation with 10-dimensional random initial condition. We also applied DBO to stochastic incompressible Navier-Stokes equation. We com-

pared the performance of DBO against BO and DO. We conclude that for well-conditioned cases, the numerical accuracy of all three decompositions are similar. However, for ill-conditioned systems, where BO and DO either diverge or show poor numerical performance, the DBO decomposition performs well.

We further implement the DBO methodology to solve for stochastic boundary conditions using the variational principle for the DBO decomposition. Minimization of the functional obtained from the variational principle leads to the evolution of the time-dependent DBO basis. The methodology assists in determining the value at a stochastic boundary for the spatial modes. We apply the method to one dimensional linear advection-diffusion equation for three different boundary conditions: (i) Dirichlet boundary (ii) Neumann boundary and (iii) Robin boundary. The error comparison for the method is presented for three methods KL, DBO and DO and three reduction orders. We observe that the DBO method performs better in the absence of unresolved modes of the system or when the order of reduction defines the system exactly. This can be attributed to the better condition number of the Σ matrix or the factorization of the covariance matrix.

The method is also applied to stochastic one dimensional Burgers' equation for stochastic Dirichlet boundary. The results for KL, DO and DBO are presented for three different reduction orders. In this case, due to the error from the unresolved modes being greater than the error in DO from the inversion of the covariance matrix, both the methods show same order of error with respect to the KL solution.

The method is applied to two dimensional linear advection-diffusion problem. We consider two cases for this equation, for the first case the conduction coefficient is kept constant making the equation linear and for the second case, the conduction coefficient has a linear temperature dependence, making the equation weakly nonlinear. The error comparison and the evolution of the modes at the boundary are compared. It is observed that both the DO and DBO methods show similar levels of accuracy.

In the third part of this work, we present a reduced order approach to solving deterministic partial differential equations with time dependent bases. We derived close form evolution equations for the time dependent bases and the core tensor. The presented methodology shows the evolution of the modes according to the evolution of the flow field.

We demonstrate the application of the method for a linear advection diffusion equation. We derive the *compressed form* of equations for the linear equation. The compressed form of equations offer computational advantages as compared to the DNS solution. The computational expense of these two methods is compared and it is observed that the linear equations in the compressed form offered a computational speed of around 16 times for the TDB for a grid size of 256×256 and around 46 times for a grid size of 512×512. While a massive speed up is obtained in computations for linear equations, the nonlinear equations are currently begin solved at the same cost as the DNS equations due to the nonlinearity and increase in the cost of computing nonlinear terms in a low rank form.

We solve the incompressible Navier-Stokes equation in the vorticity streamfunction formulation. Two cases are considered: (i) a vortex dipole with Gaussian vortices of equal strength, (ii) asymmetric vortex dipole where the strenght of one vortex is 1.1 times the strength of the other. The advantages of using time dependent bases are compared with the static basis method i.e., Proper Orthogonal Decomposition (POD). The time dependent basis save the cost of storage of the data for the determination of the static basis obtained through the covariance matrix of the snapshots. Besides, due to the localized nature of vortices the method is unable to extrapolate the results for evolution of the vortices for extended time periods. The method can only predict solutions within the time frame of the snapshots which has been given as an input for construction of the basis.

We further apply the methodology for solving a compressible 2D temporally evolving jet. We investigate how well the evolution and merging of the vortices in the jet flow are captured by the time dependent basis formulation by comparing the results to a fully resolved DNS. Besides, we also show a comparison in the solution obtained from the TDB method with an equivalent under-resolved DNS solution (URDNS). The URDNS is based on the same degrees of freedom as the TDB. The URDNS solution obtained for a low reduction order show divergence after a few time units. The TDB show a good match in resolving larger coherent structures in the flow as observed from the comparison of the spectrum plots with the DNS solution. We also observe the evolution of the modes as the flow field evolves as evident from the increase in the jet width for the x_2 modes.

The methodology is further applied to a 3D temporally evolving jet. A higher compression in the storage cost for saving the flow field at every time step is observed in higher dimensions. We observe better performance of the TDB basis as compared to its equivalent URDNS simulations.

Appendix A : Derivation of the DBO Evolution Equations

A.1 Proof of Theorem(2.4.1)

For the sake of brevity in notation, we denote $\overline{u}(x,t)$ as $\overline{u}$, $u_i(x,t)$ as u_i, $y_i(t;\omega)$ as y_i and $\Sigma_{ij}(t)$ as Σ_{ij}. The complete stochastic field given by $u(x,t;\omega)$, will be denoted as u. To obtain the evolution equations of each of the DBO components, we first substitute the DBO decomposition, given by Eq.(2.3), into a general form of SPDE as given by Eq.(2.2a). This follows:

$$\frac{\partial \overline{u}}{\partial t} + \frac{\partial u_i}{\partial t}\Sigma_{ij}y_j + u_i\frac{d\Sigma_{ij}}{dt}y_j + u_i\Sigma_{ij}\frac{dy_j}{dt} = \mathscr{F}(u) \tag{A.1}$$

We take expectation of the above equation:

$$\frac{\partial \overline{u}}{\partial t} = \mathbb{E}[\mathscr{F}(u)], \tag{A.2}$$

where we have used $\mathbb{E}[y_i] = 0$ and $d\mathbb{E}[y_i]/dt = 0$. The above equation denotes the evolution of the mean field, which is given by the first equation in the theorem i.e, Eq.(2.11a). We proceed further by obtaining a mean subtracted form of the original SPDE, by subtracting the above mean evolution equation from Eq.(A.1). This follows:

$$\frac{\partial u_i}{\partial t}\Sigma_{ij}y_j + u_i\frac{d\Sigma_{ij}}{dt}y_j + u_i\Sigma_{ij}\frac{dy_j}{dt} = \tilde{\mathscr{F}}(u), \tag{A.3}$$

where $\tilde{\mathscr{F}}(u) = \mathscr{F}(u) - \mathbb{E}[\mathscr{F}(u)]$. We then project the mean-subtracted equation onto the stochastic modes y_k,

$$\frac{\partial u_i}{\partial t}\Sigma_{ij}\mathbb{E}[y_jy_k] + u_i\frac{d\Sigma_{ij}}{dt}\mathbb{E}[y_jy_k] + u_i\Sigma_{ij}\mathbb{E}[\frac{dy_j}{dt}y_k] = \mathbb{E}[\tilde{\mathscr{F}}(u)y_k].$$

The stochastic modes are orthonormal i.e., $\mathbb{E}[y_jy_k] = \delta_{jk}$ and dynamically orthogonal i.e., $\mathbb{E}[\frac{dy_j}{dt}y_k] = 0$. Using these two conditions and changing index k to j, the above equation simplifies to:

$$\frac{\partial u_i}{\partial t}\Sigma_{ij} + u_i\frac{d\Sigma_{ij}}{dt} = \mathbb{E}[\tilde{\mathscr{F}}(u)y_j]. \tag{A.4}$$

We now project the above equation onto the spatial modes u_k,

$$\left\langle u_k, \frac{\partial u_i}{\partial t} \right\rangle \Sigma_{ij} + \langle u_k, u_i \rangle \frac{d\Sigma_{ij}}{dt} = \left\langle u_k, \mathbb{E}[\tilde{\mathscr{F}}(u) y_j] \right\rangle.$$

By enforcing the orthonormality property i.e., $\langle u_k, u_i \rangle = \delta_{ki}$ and the dynamical orthogonality property i.e., $\left\langle \frac{\partial u_k}{\partial t}, u_i \right\rangle = 0$ of the spatial basis, we obtain the evolution equation of the Σ_{ij} corresponding to Eq.(2.11b):

$$\frac{d\Sigma_{ij}}{dt} = \left\langle u_i, \mathbb{E}[\tilde{\mathscr{F}}(u) y_j] \right\rangle. \tag{A.5}$$

To obtain the evolution equations for the spatial modes, we substitute Eq.(A.5) into Eq.(A.4) and we then multiply both sides by Σ_{ij}^{-1}. This results in:

$$\frac{\partial u_i}{\partial t} = \left[\mathbb{E}[\tilde{\mathscr{F}}(u) y_j] - u_k \left\langle u_k, \mathbb{E}[\tilde{\mathscr{F}}(u) y_j] \right\rangle \right] \Sigma_{ij}^{-1}.$$

Similarly, to obtain the evolution equation for the stochastic modes, we project Eq.(A.3) onto the spatial modes u_k. This results in:

$$\left\langle u_k, \frac{\partial u_i}{\partial t} \right\rangle \Sigma_{ij} y_j + \langle u_k, u_i \rangle \frac{d\Sigma_{ij}}{dt} y_j + \langle u_k, u_i \rangle \Sigma_{ij} \frac{dy_j}{dt} = \left\langle u_k, \tilde{\mathscr{F}}(u) \right\rangle.$$

Once again we utilize the orthonormality and dynamical orthogonality of the spatial modes and substitute Eq.(A.5) into the above equation. We finally swap the indices j and i to get the form in Eq.(2.11c). The resulting equation is:

$$\frac{dy_i}{dt} = \left[\left\langle u_j, \tilde{\mathscr{F}}(u) \right\rangle - \left\langle u_j, \mathbb{E}[\tilde{\mathscr{F}}(u) y_k] \right\rangle y_k \right] \Sigma_{ji}^{-1}.$$

Since the boundary conditions are deterministic, the boundary conditions for the mean and the spatial modes are given by:

$$\begin{aligned} \mathscr{B}[\overline{u}(x,t)] &= h(x,t), && x \in \partial D, \\ \mathscr{B}[u_i(x,t)] &= 0, && x \in \partial D. \end{aligned}$$

The initial conditions for the mean are given by applying the mean value to the stochastic field at $t = 0$:

$$\overline{u}_0(x, t_0) = \mathbb{E}[u_0(x; \omega)].$$

This completes the proof.

Appendix B : Equivalence of DO and DBO Methods

B.1 Proof of Lemma (2.5.1)

(i) The transformation matrix R_u can be obtained by projecting the equivalence relation $U_{DO} = U_{DBO}R_u$ onto U_{DBO}. This results in:

$$\begin{aligned} U_{DO} &= U_{DBO}R_u, \\ R_u &= \langle U_{DBO}, U_{DO} \rangle , \end{aligned} \tag{B.1}$$

where we have used the orthonormality property of U_{DBO} basis: $\langle U_{DBO}, U_{DBO} \rangle = I$, where I is the identity matrix. Similarly projecting the equivalence relation onto U_{DO} and using the orthonormality property of the U_{DO} basis:$\langle U_{DO}, U_{DO} \rangle = I$ we obtain,

$$\begin{aligned} \langle U_{DO}, U_{DBO} \rangle R_u &= I, \\ R_u^{-1} &= \langle U_{DO}, U_{DBO} \rangle . \end{aligned}$$

It follows from the definition of inner product of quasimatrices i.e., Eq.(2.1), that the transpose of the inner product can be written as $\langle V(x,t), U(x,t) \rangle = \langle U(x,t), V(x,t) \rangle^T$. The above equation can be re-written as the transpose of inner product of quasimatrices in the following form:

$$R_u^{-1} = \langle U_{DBO}, U_{DO} \rangle^T .$$

Now, using the result from Eq.(B.1), the above equation can be written as,

$$\begin{aligned} R_u^{-1} &= R_u^T, \\ R_u^T R_u &= I. \end{aligned}$$

This equation shows that R_u^T is an inverse of R_u, which is a property of orthogonal matrices. Therefore, R_u is an orthogonal matrix.

(ii) Since the two decompositions are equivalent, we have

$$U_{DBO}\Sigma_{DBO}Y_{DBO}^T = U_{DO}Y_{DO}^T.$$

Using the transformation definition $U_{DO} = U_{DBO}R_u$ and $Y_{DO} = Y_{DBO}W_y$, the DO decomposition can be expressed as:

$$U_{DBO}\Sigma_{DBO}Y_{DBO}^T = U_{DBO}R_uW_y^TY_{DBO}^T.$$

Projecting the above equation on the U_{DBO} basis and using the orthonormality property of the DBO basis i.e., $\langle U_{DBO}, U_{DBO}\rangle = I$, we get:

$$\langle U_{DBO}, U_{DBO}\rangle \Sigma_{DBO}Y_{DBO}^T = \langle U_{DBO}, U_{DBO}\rangle R_uW_y^TY_{DBO}^T,$$
$$\Sigma_{DBO}Y_{DBO}^T = R_uW_y^TY_{DBO}^T.$$

We now project the above equation on the stochastic DBO basis, i.e. Y_{DBO}:

$$\Sigma_{DBO}\mathbb{E}[Y_{DBO}^TY_{DBO}] = R_uW_y^T\mathbb{E}[Y_{DBO}^TY_{DBO}].$$

The stochastic basis of DBO are orthonormal i.e., $\mathbb{E}[Y_{DBO}^TY_{DBO}] = I$. We apply this property to the above equation and simplify it further, which results in:

$$\Sigma_{DBO} = R_uW_y^T.$$

Multiplying the above equation by R_u^T from left and using $R_u^T = R_u^{-1}$ and transposing the resulting equation yields:

$$W_y = \Sigma_{DBO}^TR_u.$$

(iii) We now prove that the R_u matrix does not evolve in time. The evolution equation for U_{DO} in a quasimatrix form can be written as:

$$\frac{\partial U_{DO}}{\partial t} = \left[\mathbb{E}[\tilde{\mathscr{F}} Y_{DO}] - U_{DO}\mathbb{E}\left[\left\langle U_{DO}, \tilde{\mathscr{F}}\right\rangle Y_{DO}\right]\right] C_{DO}^{-1}.$$

Substituting the transformation $U_{DO} = U_{DBO}R_u$ and $Y_{DO} = Y_{DBO}W_y$ in the above equation results in:

$$\frac{\partial U_{DBO}}{\partial t}R_u + U_{DBO}\frac{dR_u}{dt} = \left[\mathbb{E}[\tilde{\mathscr{F}} Y_{DBO}] - U_{DBO}R_u R_u^T \mathbb{E}[\left\langle U_{DBO}, \tilde{\mathscr{F}}\right\rangle Y_{DBO}]\right] W_y C_{DO}^{-1}.$$

Projecting the above equation on the U_{DBO} bases, using the dynamically orthogonal condition i.e., $\left\langle \dot{U}_{DBO}, U_{DBO}\right\rangle = 0$, orthonormality property of DBO spatial modes i.e., $\langle U_{DBO}, U_{DBO}\rangle = I$ and orthogonal matrix property i.e., $R_u R_u^T = I$ on the previous equation results in:

$$\frac{dR_u}{dt} = \left[\left\langle U_{DBO}, \mathbb{E}[\tilde{\mathscr{F}} Y_{DBO}]\right\rangle - \mathbb{E}[\left\langle U_{DBO}, \tilde{\mathscr{F}}\right\rangle Y_{DBO}]\right] W_y C_{DO}^{-1}.$$

The expectation operator and the spatial inner product operations commute, which results in:

$$\frac{dR_u}{dt} = 0.$$

This completes the proof.

B.2 Proof of Theorem (2.5.1)

In this section, we prove that the DO and DBO decompositions of SPDE in Eq.(2.2) remain equivalent for all time. We begin with the evolution equations for the stochastic and spatial DO bases in the quasimatrix form:

$$\frac{\partial U_{DO}}{\partial t} = \left[\mathbb{E}[\tilde{\mathscr{F}} Y_{DO}] - U_{DO}\mathbb{E}\left[\left\langle U_{DO}, \tilde{\mathscr{F}}\right\rangle Y_{DO}\right]\right] C_{DO}^{-1}, \tag{B.2a}$$

$$\frac{dY_{DO}}{dt} = \left\langle \tilde{\mathscr{F}}, U_{DO}\right\rangle. \tag{B.2b}$$

We substitute the transformation $U_{DO} = U_{DBO}R_u$ and $Y_{DO} = Y_{DBO}W_y$ in the evolution equation for spatial DO modes i.e., Eq.(B.2a). The equation thus becomes:

$$\frac{\partial U_{DBO}}{\partial t}R_u + U_{DBO}\frac{dR_u}{dt} = \left[\mathbb{E}[\tilde{\mathscr{F}} Y_{DBO}] - U_{DBO}R_u R_u^T\mathbb{E}[\left\langle U_{DBO}, \tilde{\mathscr{F}}\right\rangle Y_{DBO}]\right] W_y C_{DO}^{-1}.$$

Using the results of (i) and (iii) from Lemma (2.5.1), the above equation can be simplified as:

$$\frac{\partial U_{DBO}}{\partial t}R_u = \left[\mathbb{E}[\tilde{\mathscr{F}} Y_{DBO}] - U_{DBO}\mathbb{E}[\left\langle U_{DBO}, \tilde{\mathscr{F}}\right\rangle Y_{DBO}]\right] W_y C_{DO}^{-1}. \tag{B.3}$$

The covariance matrix for DO is defined by the following equation:

$$C_{DO} = \mathbb{E}[Y_{DO}^T Y_{DO}]. \tag{B.4}$$

We can simplify the above equation by using the transformation $Y_{DO} = Y_{DBO}W_y$ and using the orthonormality of the DBO stochastic modes:

$$\begin{aligned} C_{DO} &= \mathbb{E}[Y_{DO}^T Y_{DO}], \\ C_{DO} &= W_y^T\mathbb{E}[Y_{DBO}^T Y_{DBO}]W_y, \\ C_{DO} &= W_y^T W_y. \end{aligned}$$

Thus, C_{DO}^{-1} can be written as $C_{DO}^{-1} = W_y^{-1}W_y^{-T}$. We now simplify the $W_y C_{DO}^{-1}$ which appears in Eq.(B.3) and using inverse of W_y^T from the property (ii) from Lemma (2.5.1).

$$\begin{aligned} W_y C_{DO}^{-1} &= W_y W_y^{-1} W_y^{-T}, \\ &= \Sigma_{DBO}^{-1} R_u. \end{aligned}$$

Multiplying Eq.(B.3) by R_u^T from right and using the value of $W_y C_{DO}^{-1}$ from the above equations and using the property of orthogonal matrix R_u i.e., $R_u^T R_u = I$, the evolution equation simplifies to:

$$\frac{\partial U_{DBO}}{\partial t} = \left[\mathbb{E}[\tilde{\mathscr{F}} Y_{DBO}] - U_{DBO}\mathbb{E}[\left\langle U_{DBO}, \tilde{\mathscr{F}} \right\rangle Y_{DBO}]\right] \Sigma_{DBO}^{-1}.$$

The above equation is the evolution equation of the DBO spatial modes in quasimatrix form. Similarly, substituting the transformations $U_{DO} = U_{DBO} R_u$ and $Y_{DO} = Y_{DBO} W_y$ in the evolution equation for Y_{DO}, i.e. Eq.(B.2b), results in:

$$\frac{dY_{DBO}}{dt} W_y + Y_{DBO} \frac{dW_y}{dt} = \left\langle \tilde{\mathscr{F}}, U_{DBO} \right\rangle R_u. \tag{B.5}$$

From parts (ii) and (iii) of Lemma (2.5.1), we have: $\dfrac{dW_y}{dt} = \dfrac{d\Sigma_{DBO}^T}{dt} R_u$. Using this relation in Eq.(B.5):

$$\begin{aligned}
\frac{dY_{DBO}}{dt} W_y + Y_{DBO} \frac{d\Sigma_{DBO}^T}{dt} R_u &= \left\langle \tilde{\mathscr{F}}, U_{DBO} \right\rangle R_u, \\
\frac{dY_{DBO}}{dt} W_y &= \left[\left\langle \tilde{\mathscr{F}}, U_{DBO} \right\rangle - Y_{DBO}\mathbb{E}\left[Y_{DBO}^T \left\langle \tilde{\mathscr{F}}, U_{DBO} \right\rangle\right]\right] R_u,
\end{aligned}$$

where evolution of Σ_{DBO}^T given by: $\frac{d\Sigma_{DBO}^T}{dt} = \mathbb{E}\left[Y_{DBO}^T \left\langle \tilde{\mathscr{F}}, U_{DBO} \right\rangle\right]$ is substituted in the above equation. Multiplying both sides of the equation by W_y^{-1} from the right and using the result of part (ii) of Lemma (2.5.1), we get:

$$\frac{dY_{DBO}}{dt} = \left[\left\langle \tilde{\mathscr{F}}, U_{DBO} \right\rangle - Y_{DBO}\mathbb{E}\left[Y_{DBO}^T \left\langle \tilde{\mathscr{F}}, U_{DBO} \right\rangle\right]\right] \Sigma_{DBO}^{-T}.$$

The above equation is the evolution equation of the DBO stochastic modes in the quasimatrix form. Thus, we see that the equivalence between the stochastic basis is maintained $\forall t > 0$. This completes the proof.

Appendix C : Equivalence of DBO and BO Methods

C.1 Proof of Lemma (2.5.2)

(i) We begin with the transformation equation for the stochastic modes given by:

$$Y_{DBO} = Y_{BO} R_y.$$

We project the above equation onto the DBO stochastic modes and use the orthonormality property of the DBO modes i.e., $\mathbb{E}[Y_{DBO}^T Y_{DBO}] = I$:

$$Y_{DBO} = Y_{BO} R_y,$$
$$\mathbb{E}[Y_{DBO}^T Y_{DBO}] = \mathbb{E}[Y_{DBO}^T Y_{BO}] R_y,$$

By using the orthonormality of the DBO stochastic coefficients, the above equation is simplified to:

$$R_y^{-1} = \mathbb{E}[Y_{DBO}^T Y_{BO}] \tag{C.1}$$

We also project the transformation equation on the BO stochastic modes and use the orthonormality condition of the BO modes i.e., $\mathbb{E}[Y_{BO}^T Y_{BO}] = I$:

$$Y_{DBO} = Y_{BO} R_y,$$
$$\mathbb{E}[Y_{BO}^T Y_{DBO}] = \mathbb{E}[Y_{BO}^T Y_{BO}] R_y,$$

which results in

$$R_y = \mathbb{E}[Y_{BO}^T Y_{DBO}].$$

Taking transpose of the above equation and using Eq.(C.1):

$$\mathbb{E}[Y_{DBO}^T Y_{BO}] = R_y^T,$$
$$R_y^{-1} = R_y^T,$$
$$R_y R_y^T = I.$$

This equation shows that R_y^T is an inverse of R_y; which is a property of orthogonal matrices. Therefore, R_y is an orthogonal matrix.

(ii) Now, since the two decompositions are equivalent, we have

$$U_{DBO}\Sigma_{DBO}Y_{DBO}^T = U_{BO}Y_{BO}^T.$$

Using the transformation equations i.e., $Y_{DBO} = Y_{BO}R_y$ and $U_{DBO} = U_{BO}W_u$ in the above equation:

$$U_{BO}W_u\Sigma_{DBO}R_y^TY_{BO}^T = U_{BO}Y_{BO}^T.$$

We now project the above equation on the U_{BO} bases and use the BO condition, i.e., $\langle U_{BO}, U_{BO}\rangle = \Lambda$, which results in:

$$\begin{aligned}\langle U_{BO}, U_{BO}\rangle W_u\Sigma_{DBO}R_y^TY_{BO}^T &= \langle U_{BO}, U_{BO}\rangle Y_{BO}^T,\\ \Lambda W_u\Sigma_{DBO}R_y^TY_{BO}^T &= \Lambda Y_{BO}^T,\\ W_u\Sigma_{DBO}R_y^TY_{BO}^T &= Y_{BO}^T.\end{aligned}$$

We now project the above equation onto the stochastic BO bases and use the orthonormality property of the bases:

$$\begin{aligned}W_u\Sigma_{DBO}R_y^T\mathbb{E}[Y_{BO}^TY_{BO}] &= \mathbb{E}[Y_{BO}^TY_{BO}],\\ W_u\Sigma_{DBO}R_y^T &= I,\\ \Sigma_{DBO} &= W_u^{-1}R_y.\end{aligned} \tag{C.2}$$

(iii) We now derive the evolution equation for W_u. We begin by using the transformation relation for the spatial modes given by:

$$U_{DBO} = U_{BO}W_u.$$

We project the above equation onto the DBO spatial modes and use the orthonormality condition of the DBO modes, i.e., $\langle U_{DBO}, U_{DBO}\rangle = I$:

$$\begin{aligned}U_{DBO} &= U_{BO}W_u,\\ \langle U_{DBO}, U_{DBO}\rangle &= \langle U_{DBO}, U_{BO}\rangle W_u,\\ \langle U_{DBO}, U_{BO}\rangle &= W_u^{-1}.\end{aligned} \tag{C.3}$$

We also project the transformation equation onto the BO spatial modes and use the BO condition i.e., $\langle U_{BO}, U_{BO} \rangle = \Lambda$:

$$\begin{aligned} U_{DBO} &= U_{BO} W_u, \\ \langle U_{BO}, U_{DBO} \rangle &= \langle U_{BO}, U_{BO} \rangle W_u, \\ \langle U_{BO}, U_{DBO} \rangle &= \Lambda W_u. \end{aligned}$$

Taking transpose of the above equation and using Eq.(C.3):

$$\begin{aligned} \langle U_{DBO}, U_{BO} \rangle &= W_u^T \Lambda, \\ W_u^{-1} &= W_u^T \Lambda, \\ W_u W_u^T &= \Lambda^{-1}. \end{aligned} \tag{C.4}$$

We now consider the evolution equation of U_{DBO} given by:

$$\frac{\partial U_{DBO}}{\partial t} = \left[\mathbb{E}[\tilde{\mathscr{F}} Y_{DBO}] - U_{DBO} \left\langle U_{DBO}, \mathbb{E}[\tilde{\mathscr{F}} Y_{DBO}] \right\rangle \right] \Sigma_{DBO}^{-1}.$$

Substituting the transformation $Y_{DBO} = Y_{BO} R_y$ and $U_{DBO} = U_{BO} W_u$ in the above equation, we obtain:

$$\frac{\partial U_{BO}}{\partial t} W_u + U_{BO} \frac{dW_u}{dt} = \left[\mathbb{E}[\tilde{\mathscr{F}} Y_{BO}] R_y - U_{BO} W_u W_u^T \left\langle U_{BO}, \mathbb{E}[\tilde{\mathscr{F}} Y_{BO}] \right\rangle R_y \right] \Sigma_{DBO}^{-1}.$$

We now use Eq.(C.2) to obtain Σ_{DBO}^{-1} versus W_u and R_y and use Eq.(C.4) to simplify the above equation further:

$$\frac{\partial U_{BO}}{\partial t} W_u + U_{BO} \frac{dW_u}{dt} = \left[\mathbb{E}[\tilde{\mathscr{F}} Y_{BO}] - U_{BO} \Lambda^{-1} \left\langle U_{BO}, \mathbb{E}[\tilde{\mathscr{F}} Y_{BO}] \right\rangle \right] W_u. \tag{C.5}$$

The evolution equation for U_{BO} is given by:

$$\begin{aligned} \frac{\partial U_{BO}}{\partial t} &= U_{BO} M + \mathbb{E}[\tilde{\mathscr{F}} Y_{BO}], \\ M &= \mathbb{E}[Y_{BO}^T \frac{dY_{BO}}{dt}]. \end{aligned}$$

We further simplify the equation by substituting the evolution equation for U_{BO} in Eq.(C.5):

$$\left[U_{BO}M + \mathbb{E}[\tilde{\mathscr{F}}Y_{BO}]\right] W_u + U_{BO}\frac{dW_u}{dt} = \left[\mathbb{E}[\tilde{\mathscr{F}}Y_{BO}] - U_{BO}\Lambda^{-1}\left\langle U_{BO}, \mathbb{E}[\tilde{\mathscr{F}}Y_{BO}]\right\rangle\right] W_u,$$
$$U_{BO}\frac{dW_u}{dt} = -U_{BO}MW_u - U_{BO}\Lambda^{-1}\left\langle U_{BO}, \mathbb{E}[\tilde{\mathscr{F}}Y_{BO}]\right\rangle W_u.$$

We project the above equation onto the U_{BO} bases and use the BO orthogonality condition of the spatial modes:

$$\Lambda\frac{dW_u}{dt} = -\Lambda\left[M + \Lambda^{-1}\left\langle U_{BO}, \mathbb{E}[\tilde{\mathscr{F}}Y_{BO}]\right\rangle\right] W_u.$$

Denoting $G = \left\langle U_{BO}, \mathbb{E}[\tilde{\mathscr{F}}Y_{BO}]\right\rangle$ according to the notation in reference [3], the evolution equation for W_u becomes:

$$\frac{dW_u}{dt} = -\left[M + \Lambda^{-1}G\right] W_u.$$

(iv) We now derive the evolution equation for R_y. We begin with the evolution equation for Y_{DBO} given by:

$$\frac{dY_{DBO}}{dt} = \left[\left\langle \tilde{\mathscr{F}}, U_{DBO}\right\rangle - Y_{DBO}\mathbb{E}\left[Y_{DBO}^T\left\langle \tilde{\mathscr{F}}, U_{DBO}\right\rangle\right]\right]\Sigma_{DBO}^{-T}.$$

The transformation equations i.e., $Y_{DBO} = Y_{BO}R_y$ and $U_{DBO} = U_{BO}W_u$ are substituted in the above equation. We also use Eq.(C.2) to replace Σ_{DBO}^{-T} versus W_u and R_y. The equation, thus, becomes:

$$\frac{dY_{BO}}{dt}R_y + Y_{BO}\frac{dR_y}{dt} = \left[\left\langle \tilde{\mathscr{F}}, U_{BO}\right\rangle W_u - Y_{BO}R_yR_y^T\mathbb{E}\left[Y_{BO}^T\left\langle \tilde{\mathscr{F}}, U_{BO}\right\rangle W_u\right]\right] W_u^T R_y.$$

Using property of orthogonal of matrix R_y and Eq.(C.4) to simplify the above equation simplifies to:

$$\frac{dY_{BO}}{dt}R_y + Y_{BO}\frac{dR_y}{dt} = \left[\left\langle \tilde{\mathscr{F}}, U_{BO}\right\rangle - Y_{BO}\mathbb{E}\left[Y_{BO}^T\left\langle \tilde{\mathscr{F}}, U_{BO}\right\rangle\right]\right]\Lambda^{-1}R_y. \tag{C.6}$$

On the other hand, the evolution equation for Y_{BO} is given by:

$$\frac{dY_{BO}}{dt} = \left[\left\langle \tilde{\mathscr{F}}, U_{BO} \right\rangle - Y_{BO} S^T\right] \Lambda^{-1},$$
$$S = \left\langle U_{BO}, \frac{\partial U_{BO}}{\partial t} \right\rangle.$$

Substituting the evolution equation for Y_{BO} in Eq.(C.6), results in:

$$\left[\left\langle \tilde{\mathscr{F}}, U_{BO} \right\rangle - Y_{BO} S^T\right] \Lambda^{-1} R_y + Y_{BO} \frac{dR_y}{dt} = \left[\left\langle \tilde{\mathscr{F}}, U_{BO} \right\rangle - Y_{BO} \mathbb{E}\left[Y_{BO}^T \left\langle \tilde{\mathscr{F}}, U_{BO} \right\rangle\right]\right] \Lambda^{-1} R_y,$$
$$-Y_{BO} S^T \Lambda^{-1} R_y + Y_{BO} \frac{dR_y}{dt} = -Y_{BO} \mathbb{E}\left[Y_{BO}^T \left\langle \tilde{\mathscr{F}}, U_{BO} \right\rangle\right] \Lambda^{-1} R_y.$$

Projecting the above equation onto Y_{BO} and using the orthonormality property of the stochastic BO modes, results in:

$$-S^T \Lambda^{-1} R_y + \frac{dR_y}{dt} = -\mathbb{E}\left[Y_{BO}^T \left\langle \tilde{\mathscr{F}}, U_{BO} \right\rangle\right] \Lambda^{-1} R_y.$$

The term $\mathbb{E}\left[Y_{BO}^T \left\langle \tilde{\mathscr{F}}, U_{BO} \right\rangle\right]$ can be expressed as G^T according to the notation in reference [3]. Thus, the evolution equation for R_y can be written as:

$$\frac{dR_y}{dt} = (S^T - G^T) \Lambda^{-1} R_y.$$

This completes the proof.

C.2 Proof of Theorem (2.5.2)

In this theorem, we prove that the equivalence relation is valid for all $t > 0$. The DBO evolution equations in the quasimatrix form are given by:

$$\frac{\partial U_{DBO}}{\partial t} = \left[\mathbb{E}[\tilde{\mathscr{F}} Y_{DBO}] - U_{DBO}\mathbb{E}[\left\langle U_{DBO}\tilde{\mathscr{F}}\right\rangle Y_{DBO}]\right]\Sigma_{DBO}^{-1}, \tag{C.7a}$$

$$\frac{dY_{DBO}}{dt} = \left[\left\langle \tilde{\mathscr{F}}, U_{DBO}\right\rangle - Y_{DBO}\mathbb{E}\left[Y_{DBO}^T\left\langle \tilde{\mathscr{F}}, U_{DBO}\right\rangle\right]\right]\Sigma_{DBO}^{-T}. \tag{C.7b}$$

We plug $U_{DBO} = U_{BO}W_u$ and $Y_{DBO} = Y_{BO}R_y$ into the evolution equation for U_{DBO} i.e., Eq.(C.7a). The equation thus becomes:

$$\frac{\partial U_{BO}}{\partial t}W_u + U_{BO}\frac{dW_u}{dt} = \left[\mathbb{E}[\tilde{\mathscr{F}} Y_{BO}]R_y - U_{BO}W_uW_u^T\left\langle U_{BO}, \mathbb{E}[\tilde{\mathscr{F}} Y_{BO}]\right\rangle R_y\right]\Sigma_{DBO}^{-1}.$$

Using Eq.(C.4) and Eq.(C.2) in the above equation, results in:

$$\frac{\partial U_{BO}}{\partial t}W_u + U_{BO}\frac{dW_u}{dt} = \left[\mathbb{E}[\tilde{\mathscr{F}} Y_{BO}] - U_{BO}\Lambda^{-1}\left\langle U_{BO}, \mathbb{E}[\tilde{\mathscr{F}} Y_{BO}]\right\rangle\right]W_u.$$

Using property (iii) of Lemma (2.5.2) and definition of G, i.e., $G = \left\langle U_{BO}, \mathbb{E}[\tilde{\mathscr{F}} Y_{BO}]\right\rangle$:

$$\begin{aligned}
\frac{\partial U_{BO}}{\partial t}W_u - U_{BO}\left[M + \Lambda^{-1}G\right]W_u &= \left[\mathbb{E}[\tilde{\mathscr{F}} Y_{BO}] - U_{BO}\Lambda^{-1}G\right]W_u,\\
\frac{\partial U_{BO}}{\partial t}W_u &= U_{BO}MW_u + \mathbb{E}[\tilde{\mathscr{F}} Y_{BO}]W_u,\\
\frac{\partial U_{BO}}{\partial t} &= U_{BO}M + \mathbb{E}[\tilde{\mathscr{F}} Y_{BO}].
\end{aligned}$$

The above equation is the evolution equation for U_{BO}. Thus, we see that the equivalence between the spatial bases is maintained $\forall t > 0$. Similarly, we substitute the transformations $U_{DBO} = U_{BO}W_u$ and $Y_{DBO} = Y_{BO}R_y$ into the evolution equation for Y_{DBO} i.e., Eq.(C.7b). The equation thus becomes:

$$\frac{dY_{BO}}{dt}R_y + Y_{BO}\frac{dR_y}{dt} = \left[\left\langle \tilde{\mathscr{F}}, U_{BO}\right\rangle W_u - Y_{BO}R_yR_y^T\mathbb{E}\left[Y_{BO}^T\left\langle \tilde{\mathscr{F}}, U_{BO}\right\rangle W_u\right]\right]\Sigma_{DBO}^{-T}.$$

Using Eq.(C.4) and Eq.(C.2) to simplify the above equation:

$$\frac{dY_{BO}}{dt}R_y + Y_{BO}\frac{dR_y}{dt} = \left[\left\langle \tilde{\mathscr{F}}, U_{BO}\right\rangle - Y_{BO}\mathbb{E}\left[Y_{BO}^T\left\langle \tilde{\mathscr{F}}, U_{BO}\right\rangle\right]\right]\Lambda^{-1}R_y.$$

Using property (iv) of Lemma (2.5.2) and definition of G^T, i.e., $G^T = \mathbb{E}\left[Y_{BO}^T \left\langle \tilde{\mathscr{F}}, U_{BO} \right\rangle\right]$:

$$\frac{dY_{BO}}{dt} R_y + Y_{BO}\left[S^T - G^T\right]\Lambda^{-1} R_y = \left[\left\langle \tilde{\mathscr{F}}, U_{BO} \right\rangle - Y_{BO} G^T\right]\Lambda^{-1} R_y,$$
$$\frac{dY_{BO}}{dt} = \left[\left\langle \tilde{\mathscr{F}}, U_{BO} \right\rangle - Y_{BO} S^T\right]\Lambda^{-1}.$$

The above equation is the evolution equation of the BO stochastic bases in the quasimatrix form. Thus, we see that the equivalence between the stochastic basis is maintained $\forall t > 0$. This completes the proof.

Appendix D : DBO Evolution Equations Using The Variational Principle and The First Order Optimality Conditions

In this section we obtain the closed form evolution equations for DBO using the first order optimality conditions on the functional in the variational principle.

We begin with the functional form of the variational principle. For simplicity of notation we denote $\mathcal{M}(u,x,t)$ as $\mathcal{M}$, $u_i(x,t)$ is denoted as u_i, $y_j(t)$ is denoted as y_j and $\Sigma_{ij}(t)$ is denoted as Σ_{ij}. Here $\mathcal{M}$ is a quasimatrix, $\mathcal{M} \in \mathbb{R}^{\infty \times s}$, where s is the number of discrete sample points in the random space.

$$\mathcal{G}(\dot{U},\dot{\Sigma},\dot{Y}) = \left\| \frac{\partial}{\partial t}(u_i \Sigma_{ij} y_j^T) - \mathcal{M} \right\|_{\mathcal{F}}^2 + \lambda_{1_{ij}} \left(\langle \dot{u}_i, u_j \rangle - \Phi_{ij} \right) + \lambda_{2_{ij}} \left(\mathbb{E}[\dot{y}_i y_j] - \Psi_{ij} \right).$$

The first term in the above equation can be expanded further as:

$$\begin{aligned}
\left\| \frac{\partial}{\partial t}(u_i \Sigma_{ij} y_j^T) - \mathcal{M} \right\|_{\mathcal{F}}^2 &= \langle \dot{u}_i, \dot{u}_m \rangle \Sigma_{ij} \Sigma_{mn} \mathbb{E}[y_j y_n] + \langle u_i, u_m \rangle \dot{\Sigma}_{ij} \dot{\Sigma}_{mn} \mathbb{E}[y_j y_n] \\
&\quad + \langle u_i, u_m \rangle \Sigma_{ij} \Sigma_{mn} \mathbb{E}[\dot{y}_j \dot{y}_n] + 2\langle \dot{u}_i, u_m \rangle \Sigma_{ij} \dot{\Sigma}_{mn} \mathbb{E}[y_j y_n] \\
&\quad + 2\langle u_i, u_m \rangle \dot{\Sigma}_{ij} \Sigma_{mn} \mathbb{E}[y_j \dot{y}_n] + 2\langle \dot{u}_i, u_m \rangle \Sigma_{ij} \Sigma_{mn} \mathbb{E}[y_j \dot{y}_n] \\
&\quad - 2\mathbb{E}[\langle \mathcal{M}, u_i \rangle \dot{y}_j] \Sigma_{ij} - 2\mathbb{E}[\langle \mathcal{M}, \dot{u}_i \rangle y_j] \Sigma_{ij} - 2\mathbb{E}[\langle \mathcal{M}, u_i \rangle y_j] \dot{\Sigma}_{ij} \\
&\quad + \|\mathcal{M}\|_{\mathcal{F}}^2 .
\end{aligned}$$

The first order optimality conditions enforce $\frac{\delta \mathcal{G}}{\delta \dot{u}_k} = 0$, $\frac{\delta \mathcal{G}}{\delta \dot{y}_k} = 0$ and $\frac{\delta \mathcal{G}}{\delta \dot{\Sigma}_{kl}} = 0$, $k,l = 1,\ldots,r$.

1. We take a look at the first optimality condition by taking a derivative of the above functional w.r.t. $\dot{u}_k$:

$$\begin{aligned}
\frac{\delta \mathcal{G}}{\delta \dot{u}_k} &= \lim_{\epsilon \to 0} \frac{\mathcal{G}(\dot{U} + \epsilon \dot{\tilde{U}}, \dot{\Sigma}, \dot{Y}) - \mathcal{G}(\dot{U}, \dot{\Sigma}, \dot{Y})}{\epsilon} \\
&= \quad 2\big\langle \dot{\tilde{u}}_i, \dot{u}_m \big\rangle \Sigma_{ij} \Sigma_{mn} \mathbb{E}[y_j y_n] + 2\big\langle \dot{\tilde{u}}_i, u_m \big\rangle \Sigma_{ij} \dot{\Sigma}_{mn} \mathbb{E}[y_j y_n] \\
&\quad + 2\big\langle \dot{\tilde{u}}_i, u_m \big\rangle \Sigma_{ij} \Sigma_{mn} \mathbb{E}[y_j \dot{y}_n] - 2\mathbb{E}[\big\langle \mathcal{M}, \dot{\tilde{u}}_i \big\rangle y_j] \Sigma_{ij} + \lambda_{1_{ij}} \big\langle \dot{\tilde{u}}_i, u_j \big\rangle \\
&= \quad 2\Big\langle \dot{\tilde{u}}_i, \dot{u}_m \Sigma_{ij} \Sigma_{mn} \mathbb{E}[y_j y_n] + u_m \Sigma_{ij} \dot{\Sigma}_{mn} \mathbb{E}[y_j y_n] + u_m \Sigma_{ij} \Sigma_{mn} \mathbb{E}[y_j \dot{y}_n] \\
&\quad - \mathbb{E}[\mathcal{M} y_j] \Sigma_{ij} + \frac{\lambda_{1_{ij}}}{2} u_j \Big\rangle \\
&= \quad 0
\end{aligned}$$

Since the variation $\dot{\tilde{u}}_i$ is assumed to be arbitrary, the constraint equation is,

$$\Big(\dot{u}_m \Sigma_{ij} \Sigma_{mn} + u_m \Sigma_{ij} \dot{\Sigma}_{mn}\Big) \mathbb{E}[y_j y_n] + u_m \Sigma_{ij} \Sigma_{mn} \mathbb{E}[y_j \dot{y}_n] - \mathbb{E}[\mathcal{M} y_j] \Sigma_{ij} + \frac{\lambda_{1_{ij}}}{2} u_j = 0. \tag{D.1}$$

Projecting the above equation on the u_k and using the orthonormality conditions of the spatial and stochastic modes i.e., $\big\langle u_i, u_j \big\rangle = \delta_{ij}$ and $\mathbb{E}[y_i y_j] = \delta_{ij}$ as well as the dynamic orthogonality constraints of the modes i.e.,$\big\langle \dot{u}_i, u_j \big\rangle = \Phi_{ij}$ and $\mathbb{E}[\dot{y}_i y_j] = \Psi_{ij}$ we obtain the value of the Lagrangian multiplier λ_1:

$$\lambda_{1_{ij}} = 2\Big[\big\langle u_j, \mathbb{E}[\mathcal{M} y_k] \big\rangle - \Phi_{mj} \Sigma_{mk} - \dot{\Sigma}_{jk} - \Psi_{nk} \Sigma_{jn}\Big] \Sigma_{ik}. \tag{D.2}$$

The equation for $\lambda_{1_{ij}}$ obtained in Eq.(D.2) is substituted in Eq.(D.1) to obtain the evolution equation for $\dot{u}_i$. After substitution, the orthonormality condition of the stochastic modes i.e., $\mathbb{E}[y_i y_j] = \delta_{ij}$ and the dynamic orthogonality constraint on the stochastic modes i.e., $\mathbb{E}[\dot{y}_i y_j] = \Psi_{ij}$ are applied to simplify the equation further. Thus, the obtained equation is,

$$\begin{aligned}
&\dot{u}_j \Sigma_{jk} \Sigma_{ik} - \mathbb{E}[\mathcal{M} y_k] \Sigma_{ik} + u_j \big\langle u_j, \mathbb{E}[\mathcal{M} y_k] \big\rangle \Sigma_{ik} - u_m \Phi_{jm} \Sigma_{jk} \Sigma_{ik} \\
&\quad + \Big(u_j \dot{\Sigma}_{jk} \Sigma_{ik} - u_j \dot{\Sigma}_{jk} \Sigma_{ik}\Big) + (u_j \Sigma_{jn} \Psi_{nk} \Sigma_{ik} - u_j \Sigma_{jn} \Psi_{nk} \Sigma_{ik}) = 0.
\end{aligned}$$

The final equation for evolution of the modes is obtained by multiplying $\Sigma_{ik}^{-1}\Sigma_{jk}^{-1}$ on both sides of the equation,

$$\dot{u}_i = \left[\mathbb{E}[\mathcal{M}y_j] - u_k\big\langle u_k, \mathbb{E}[\mathcal{M}y_j]\big\rangle\right]\Sigma_{ij}^{-1} + u_j\Phi_{ij}, \tag{D.3}$$

where $\mathcal{M}$ represents the evolution at the boundary points and the interior points, defined as,

$$\mathcal{M}(u,x,t;\omega) = \begin{cases} \mathcal{N}(u,x,t;\omega) & \text{if } x \in \Omega, \\ \mathcal{B}(u,x,t;\omega) & \text{if } x \in \partial\Omega, \end{cases}$$

2. We take a look at the second optimality condition by taking the derivative of the functional $\mathcal{G}$ w.r.t. $\dot{y}_k$:

$$\begin{aligned}
\frac{\delta\mathcal{G}}{\delta\dot{y}_k} &= \lim_{\epsilon\to 0}\frac{\mathcal{G}(\dot{U},\dot{\Sigma},\dot{Y}+\epsilon\dot{\tilde{Y}}) - \mathcal{G}(\dot{U},\dot{\Sigma},\dot{Y})}{\epsilon} \\
&= \quad 2\big\langle u_i,u_m\big\rangle\Sigma_{ij}\Sigma_{mn}\mathbb{E}[\dot{y}_j\dot{\tilde{y}}_n] + 2\big\langle u_i,u_m\big\rangle\dot{\Sigma}_{ij}\Sigma_{mn}\mathbb{E}[y_j\dot{\tilde{y}}_n] \\
&\quad + 2\big\langle \dot{u}_i,u_m\big\rangle\Sigma_{ij}\Sigma_{mn}\mathbb{E}[y_j\dot{\tilde{y}}_n] - 2\mathbb{E}[\big\langle\mathcal{M},u_i\big\rangle\dot{\tilde{y}}_j]\Sigma_{ij} + \lambda_{2_{jn}}\mathbb{E}[y_j\dot{\tilde{y}}_n] \\
&= \quad 2\mathbb{E}\Bigg[\Bigg(\big\langle u_i,u_m\big\rangle\Sigma_{ij}\Sigma_{mn}\dot{y}_j^T + \big\langle u_i,u_m\big\rangle\dot{\Sigma}_{ij}\Sigma_{mn}y_j^T + \big\langle \dot{u}_i,u_m\big\rangle\Sigma_{ij}\Sigma_{mn}y_j^T \\
&\quad -\Sigma_{in}\big\langle u_i,\mathcal{M}\big\rangle + \frac{\lambda_{2_{jn}}}{2}y_j\Bigg)\dot{\tilde{y}}_n\Bigg].
\end{aligned}$$

Since the variation $\dot{\tilde{y}}_n$ is assumed to be arbitrary, the constraint equation is,

$$\big\langle u_i,u_m\big\rangle\left(\Sigma_{ij}\Sigma_{mn}\dot{y}_j^T + \dot{\Sigma}_{ij}\Sigma_{mn}y_j^T\right) + \big\langle \dot{u}_i,u_m\big\rangle\Sigma_{ij}\Sigma_{mn}y_j^T - \Sigma_{in}\big\langle u_i,\mathcal{M}\big\rangle + \frac{\lambda_{2_{jn}}}{2}y_j^T = 0. \tag{D.4}$$

Projecting the above equation on y_k and using the orthonormality conditions of the spatial and stochastic modes i.e., $\big\langle u_i,u_j\big\rangle = \delta_{ij}$ and $\mathbb{E}[y_iy_j] = \delta_{ij}$ as well as the dynamic orthogonality constraints of the modes i.e.,$\big\langle \dot{u}_i,u_j\big\rangle = \Phi_{ij}$ and $\mathbb{E}[\dot{y}_iy_j] = \Psi_{ij}$ we obtain the value of the Lagrangian multiplier λ_2:

$$\lambda_{2_{jn}} = 2\left[\mathbb{E}[\big\langle\mathcal{M},u_i\big\rangle y_j] - \Psi_{kj}\Sigma_{ik} - \dot{\Sigma}_{ij} - \Phi_{mi}\Sigma_{mj}\right]\Sigma_{in}. \tag{D.5}$$

The value obtained for $\lambda_{2_{jn}}$ in Eq.(D.5) is substituted in Eq.(D.4) to obtain the evolution equation for $\dot{y}_i$. After substitution, the orthonormality condition of the spatial modes

i.e., $\langle u_i, u_j \rangle = \delta_{ij}$ and the dynamic orthogonality constraint of the spatial modes i.e., $\langle \dot{u}_i, u_j \rangle = \Phi_{ij}$ are applied to simplify the equation further. Thus, the obtained equation is,

$$\Sigma_{mn}\Sigma_{mj}\dot{y}_j^T - \Sigma_{mn}\langle u_m, \mathcal{M}\rangle + \Sigma_{mn}\mathbb{E}\left[\langle \mathcal{M}, u_m\rangle y_j\right] y_j^T - \Sigma_{mn}\Sigma_{mj}\Psi_{jk}y_k^T$$
$$+ \left(\dot{\Sigma}_{mj}\Sigma_{mn}y_j^T - \dot{\Sigma}_{mj}\Sigma_{mn}y_j^T\right) + \left(\Sigma_{mn}\Phi_{im}\Sigma_{ij}y_j^T - \Sigma_{mn}\Phi_{im}\Sigma_{ij}y_j^T\right) = 0.$$

The equation is simplified further by multiplying both sides of the above equation with Σ_{mn}^{-1},

$$\Sigma_{mj}\dot{y}_j^T = \langle u_m, \mathcal{M}\rangle - \mathbb{E}[\langle u_m, \mathcal{M}\rangle y_j]y_j^T + \Sigma_{mj}\Psi_{jk}y_k^T.$$

The final equation is obtained by taking the transpose of the above equation and multiplying both sides of the obtained equation with Σ_{jm}^{-1},

$$\dot{y}_i = \left[\langle \mathcal{M}, u_j\rangle - y_k\mathbb{E}[y_k\langle \mathcal{M}, u_j\rangle]\right]\Sigma_{ji}^{-1} + y_j\Psi_{ji}. \tag{D.6}$$

3. We take a look at the third optimality condition by taking the derivative of the functional $\mathcal{G}$ w.r.t. $\dot{\Sigma}_{kl}$

$$\begin{aligned}\frac{\delta\mathcal{G}}{\delta\dot{\Sigma}_{kl}} &= \lim_{\epsilon\to 0}\frac{\mathcal{G}(\dot{U}, \dot{\Sigma} + \epsilon\dot{\tilde{\Sigma}}, \dot{Y}) - \mathcal{G}(\dot{U}, \dot{\Sigma}, \dot{Y})}{\epsilon} \\ &= 2\Big(\langle \dot{u}_i, u_m\rangle\Sigma_{mn}\mathbb{E}[y_j y_n] + \langle u_i, u_m\rangle\dot{\Sigma}_{mn}\mathbb{E}[y_j y_n] \\ &\quad + \langle u_i, u_m\rangle\Sigma_{mn}\mathbb{E}[y_j\dot{y}_n] - \mathbb{E}[\langle \mathcal{M}, u_i\rangle y_j]\Big)\dot{\tilde{\Sigma}}_{ij} \\ &= 0\end{aligned}$$

Since the variation $\dot{\tilde{\Sigma}}_{ij}$ is assumed to be arbitrary the constraint equation is,

$$\langle \dot{u}_i, u_m\rangle\Sigma_{mn}\mathbb{E}[y_j y_n] + \langle u_i, u_m\rangle\dot{\Sigma}_{mn}\mathbb{E}[y_j y_n] + \langle u_i, u_m\rangle\Sigma_{mn}\mathbb{E}[y_j\dot{y}_n] - \mathbb{E}[\langle \mathcal{M}, u_i\rangle y_j] = 0.$$

Using the orthonormality conditions of the spatial and stochastic modes i.e., $\langle u_i, u_j\rangle = \delta_{ij}$ and $\mathbb{E}[y_i y_j] = \delta_{ij}$, as well as the dynamic orthogonality constraints of the modes i.e.,$\langle \dot{u}_i, u_j\rangle = \Phi_{ij}$ and $\mathbb{E}[\dot{y}_i y_j] = \Psi_{ij}$, the equation for the evolution of the $\dot{\Sigma}$ is,

$$\dot{\Sigma}_{ij} = \mathbb{E}[\langle \mathcal{M}, u_i\rangle y_j] - \Phi_{ik}\Sigma_{kj} + \Psi_{jk}\Sigma_{ik}. \tag{D.7}$$

Appendix E : Computational Details- Temporally Evolving Jet

This appendix gives the computational details for the temporally evolving jet problem in Chapter 5.

E.1 2D Temporally Evolving Jet

The primary variables considered here are, density $\rho(x_1, x_2, t)$, velocity vector $\mathbf{v}(\mathbf{x}, t) = [v_1(x_1, x_2, t), v_2(x_1, x_2, t)]$, pressure $p(x_1, x_2, t)$, total energy $E_t(x_1, x_2, t)$ and temperature $T(x_1, x_2, t)$. The equations for the evolution of the variables are given by,

$$\frac{\partial \mathbf{V}}{\partial t} + \frac{\partial \mathbf{E}}{\partial x_1} + \frac{\partial \mathbf{F}}{\partial x_2} = 0, \tag{E.1}$$

where $\mathbf{U}, \mathbf{E}, \mathbf{F}$ are the vectors given by,

$$\mathbf{V} = \begin{bmatrix} \rho \\ \rho v_1 \\ \rho v_2 \\ E_t \end{bmatrix}, \mathbf{E} = \begin{bmatrix} \rho v_1 \\ \rho v_1^2 + p - \tau_{11} \\ \rho v_1 v_2 - \tau_{12} \\ (E_t + p)v_1 - v_1\tau_{11} - v_2\tau_{12} + q_1 \end{bmatrix}, \mathbf{F} = \begin{bmatrix} \rho v_2 \\ \rho v_1 v_2 - \tau_{12} \\ \rho v_2^2 + p - \tau_{22} \\ (E_t + p)v_2 - v_1\tau_{12} - v_2\tau_{22} + q_2 \end{bmatrix}.$$

Here E_t is the total energy per unit volume, which can be written as

$$E_t = \rho \left(e + \frac{v_1^2 + v_2^2}{2} \right). \tag{E.2}$$

where e is the internal energy per unit mass. The components of viscous stress tensor are given by

$$\tau_{ij} = \mu \left[\left(\frac{\partial v_i}{\partial x_j} + \frac{\partial v_j}{\partial x_i} \right) - \frac{2}{3}\delta_{ij} \frac{\partial v_k}{\partial x_k} \right]. \tag{E.3}$$

The heat flux vectors are given by

$$q_i = \frac{\mu}{(\gamma - 1)M_\infty^2 RePr} \frac{\partial T}{\partial x_i},$$

where M_∞ is the free stream Mach number and Re, Pr are the Reynolds number and the Prandtl numbers respectively. The values of these parameters are taken to be, $Re = 8000$, $Pr = 1$, $M_\infty = 0.5$. The pressure and the temperature are obtained from the equations of state,

$$p = (\gamma - 1)\rho e \tag{E.4}$$

$$T = \frac{\gamma M_\infty^2 p}{\rho} \tag{E.5}$$

We take the value of γ to be 1.4. $\rho, \rho v_1, \rho v_2$ and E_t are taken to be independent variables and are expressed in the time dependent basis decomposition. The initial conditions for the mean velocity profile are given by,

$$\bar{v}_1 = \frac{V_{max}}{2}\left(\tanh\left(\frac{x_2 - x_{2_{min}}}{h}\right) - \tanh\left(\frac{x_2 - x_{2_{max}}}{h}\right) - 1\right)$$

$$\bar{v}_2 = 0$$

Here $V_{max} = 1$, $x_{2_{min}}$ and $x_{2_{max}}$ denote the lower and upper boundaries of the jet which are set to 0.45 and 0.55 respectively. h represents the thickness of the jet which for this case is taken to be 1/100. The velocity profile for v_1 is shown in Fig.(44). The jet boundaries are imposed with perturbation to trigger the transition. The perturbations are given by,

$$\tilde{v}_2 = 2\frac{L_{x_1}}{h^2}\left[(x_2 - b)\exp\left(-\frac{(x_2 - b)^2}{h^2}\right) + (x_2 - a)\exp\left(-\frac{(x_2 - a)^2}{h^2}\right)\right]$$
$$\left[\sin(12\pi\frac{x_1}{L_{x_1}}) + \sin(8\pi\frac{x_1}{L_{x_1}}) + \sin(20\pi\frac{x_1}{L_{x_1}})\right],$$

$$\tilde{v}_2 = \pi\left[\exp(-\frac{(x_2 - b)^2}{h^2}) + \exp(-\frac{(x_2 - a)^2}{h^2})\right]\left[12\cos(12\pi\frac{x_1}{L_{x_1}}) + 8\cos(8\pi\frac{x_1}{L_{x_1}}) + 20\cos(20\pi\frac{x_1}{L_{x_1}})\right]$$

$$A = \max(\sqrt{\tilde{v}_1^2 + \tilde{v}_2^2}),$$

$$\delta = \frac{V_{max}}{40A},$$

$$(\tilde{v}_1, \tilde{v}_2) = (\delta\tilde{v}_1, \delta\tilde{v}_2)$$

Here, $L_{x_1} = 2$ and $L_{x_2} = 1$, $a = 0.45$, $b = 0.55$. The initial conditions for the other variables is,

$$
\begin{aligned}
T(t=0) &= \frac{1}{2} + \frac{1}{4}\left(\tanh\left(\frac{x_2 - x_{2_{min}}}{h}\right) - \tanh\left(\frac{x_2 - x_{2_{max}}}{h}\right)\right), \\
p(t=0) &= 1, \\
\rho(t=0) &= \frac{\gamma M_\infty^2 p}{T}, \\
e(t=0) &= \frac{p}{(\gamma-1)\rho}, \\
E(t=0) &= \rho\left(e + \frac{v_1^2 + v_2^2}{2}\right).
\end{aligned}
$$

E.2 3D Temporally Evolving Jet

The primary variables considered here are, density $\rho(x_1, x_2, x_3, t)$, velocity vector $\mathbf{v}(\mathbf{x}, t) = [v_1(x_1, x_2, x_3, t), v_2(x_1, x_2, x_3, t), v_3(x_1, x_2, x_3, t)]$, pressure $p(x_1, x_2, x_3, t)$, total energy $E_t(x_1, x_2, x_3, t)$ and temperature $T(x_1, x_2, x_3, t)$. The equations for the evolution of the primary variables are given by,

$$
\frac{\partial \mathbf{V}}{\partial t} + \frac{\partial \mathbf{E}}{\partial x_1} + \frac{\partial \mathbf{F}}{\partial x_2} + \frac{\partial \mathbf{G}}{\partial x_3} = 0, \tag{E.6}
$$

where $\mathbf{U}, \mathbf{E}, \mathbf{F}, \mathbf{G}$ are the vectors given by

$$
\mathbf{V} = \begin{bmatrix} \rho \\ \rho v_1 \\ \rho v_2 \\ \rho v_3 \\ E_t \end{bmatrix}, \mathbf{E} = \begin{bmatrix} \rho v_1 \\ \rho v_1^2 + p - \tau_{11} \\ \rho v_1 v_2 - \tau_{12} \\ \rho v_1 v_3 - \tau_{13} \\ (E_t + p)v_1 - v_1\tau_{11} - v_2\tau_{12} - v_3\tau_{13} + q_1 \end{bmatrix},
$$

$$
\mathbf{F} = \begin{bmatrix} \rho v_2 \\ \rho v_1 v_2 - \tau_{12} \\ \rho v_2^2 + p - \tau_{22} \\ \rho v_2 v_3 - \tau_{23} \\ (E_t + p)v_2 - v_1\tau_{12} - v_2\tau_{22} - v_3\tau_{23} + q_2 \end{bmatrix}, \mathbf{G} = \begin{bmatrix} \rho v_3 \\ \rho v_1 v_3 - \tau_{13} \\ \rho v_2 v_3 - \tau_{23} \\ \rho v_3^2 + p - \tau_{33} \\ (E_t + p)v_3 - v_1\tau_{13} - v_2\tau_{23} - v_3\tau_{33} + q_3 \end{bmatrix}
$$

Here E_t is the total energy per unit volume, which can be written as

$$E_t = \rho\left(e + \frac{v_1^2 + v_2^2 + v_3^2}{2}\right). \tag{E.7}$$

where e is the internal energy per unit mass. The components of viscous stress tensor are given by

$$\tau_{ij} = \mu\left[\left(\frac{\partial v_i}{\partial x_j} + \frac{\partial v_j}{\partial x_i}\right) - \frac{2}{3}\delta_{ij}\frac{\partial v_k}{\partial x_k}\right]. \tag{E.8}$$

The heat flux vectors are given by

$$q_i = \frac{\mu}{(\gamma-1)M_\infty^2 RePr}\frac{\partial T}{\partial x_i},$$

where M_∞ is the free stream Mach number and Re, Pr are the Reynolds number and the Prandtl number respectively. The values of these parameters is taken to be, $Re = 5000$, $Pr = 1$, $M_\infty = 0.5$. The pressure and the temperature are obtained from the equations of state,

$$p = (\gamma-1)\rho e \tag{E.9}$$

$$T = \frac{\gamma M_\infty^2 p}{\rho} \tag{E.10}$$

We take the value of γ to be 1.4. $\rho, \rho v_1, \rho v_2, \rho v_3$ and E_t are taken to be independent variables and are expressed in the TDB decomposition. The initial conditions for the mean velocity profile are given by,

$$\bar{v}_1 = \frac{V_{max}}{2}\left(\tanh\left(\frac{x_2 - x_{2_{min}}}{h}\right) - \tanh\left(\frac{x_2 - x_{2_{max}}}{h}\right) - 1\right)$$

$$\bar{v}_2 = 0$$

$$\bar{v}_3 = 0$$

Here $V_{max} = 1$, $x_{2_{min}}$ and $x_{2_{max}}$ denote the lower and upper boundaries of the jet which are set to 0.45 and 0.55 respectively. h represents the thickness of the jet which for this case is taken to be 1/200. The mean velocity profile used for initialization is shown in Fig.(54). The

jet boundaries are imposed with perturbation to trigger the transition and the perturbations are given by,

$$\tilde{v}_1 = 2\frac{L_{x_1}}{h^2}\left[(x_2-b)\exp\left(-\frac{(x_2-b)^2}{h^2}\right)+(x_2-a)\exp\left(-\frac{(x_2-a)^2}{h^2}\right)\right]$$
$$\left[\sin(2\pi\frac{x_1}{L_{x_1}})+\sin(4\pi\frac{x_1}{L_{x_1}})+\sin(8\pi\frac{x_1}{L_{x_1}})\right]\left[\sin(2\pi\frac{x_3}{L_{x_3}})+\sin(4\pi\frac{x_3}{L_{x_3}})+\cos(6\pi\frac{x_3}{L_{x_3}})+\cos(8\pi\frac{x_3}{L_{x_3}})\right],$$
$$\tilde{v}_2 = \pi\left[\exp(-\frac{(x_2-b)^2}{h^2})+\exp(-\frac{(x_2-a)^2}{h^2})\right]\left[2\cos(2\pi\frac{x_1}{L_{x_1}})+4\cos(4\pi\frac{x_1}{L_{x_1}})+8\cos(8\pi\frac{x_1}{L_{x_1}})\right]$$
$$\left[\sin(2\pi\frac{x_3}{L_{x_3}})+\sin(4\pi\frac{x_3}{L_{x_3}})+\cos(6\pi\frac{x_3}{L_{x_3}})+\cos(8\pi\frac{x_3}{L_{x_3}})\right],$$
$$\tilde{v}_3 = -\frac{L_{x_1}}{h^2}\left[(x_2-b)\exp\left(-\frac{(x_2-b)^2}{h^2}\right)+(x_2-a)\exp\left(-\frac{(x_2-a)^2}{h^2}\right)\right]$$
$$\left[2\cos(2\pi\frac{x_1}{L_{x_1}})+4\cos(4\pi\frac{x_1}{L_{x_1}})+8\cos(8\pi\frac{x_1}{L_{x_1}})\right]$$
$$\left[-2\cos(2\pi\frac{x_3}{L_{x_3}})-4\cos(4\pi\frac{x_3}{L_{x_3}})+6\sin(6\pi\frac{x_3}{L_{x_3}})+8\sin(8\pi\frac{x_3}{L_{x_3}})\right],$$
$$A = \max(\sqrt{\tilde{v}_1^2+\tilde{v}_2^2+\tilde{v}_3^2}),$$
$$\delta = \frac{V_{max}}{40A},$$
$$\tilde{v}_1 = \delta\tilde{v}_1,$$
$$\tilde{v}_2 = \delta\tilde{v}_2,$$
$$\tilde{v}_3 = \delta\tilde{v}_3.$$

Here, $L_{x_1} = L_{x_2} = L_{x_3} = 1$, $a = 0.45$, $b = 0.55$. The initial conditions for the other variables are,

$$T(t=0) = \frac{1}{2}+\frac{1}{4}\left(\tanh\left(\frac{x_2-x_{2_{min}}}{h}\right)-\tanh\left(\frac{x_2-x_{2_{max}}}{h}\right)\right),$$
$$p(t=0) = 1,$$
$$\rho(t=0) = \frac{\gamma M_\infty^2 p}{T},$$
$$e(t=0) = \frac{p}{(\gamma-1)\rho},$$
$$E(t=0) = \rho\left(e+\frac{v_1^2+v_2^2+v_3^2}{2}\right).$$

Appendix F : Summary of The Reduced Order Modeling Techniques

In this appendix, we discuss the various reduced order techniques discussed in the thesis and present a comprehensive summary and comparison of the relevant methods. The intent of this chapter to provide the reader with a brief essence of the thesis and discuss the important advantages and drawbacks of the different methods in a broader perspective.

F.1 Proper Orthogonal Decomposition (POD)

The proper orthogonal decomposition is a method developed by Lumley [49] in the context of fluid dynamics to obtain 'coherent structures 'from turbulent flow fields. The method has been known by different names in other fields: Principal component analysis (PCA), Hotelling transform, empirical eigenfunction decomposition, Karhunen-Loéve decomposition.

F.1.1 POD Decomposition

We consider a random field $u(\mathbf{x}, t; \omega)$ and subtract the time average of the DNS simulation $\bar{u}(\mathbf{x})$. The mean subtracted value can then be expressed as,

$$u(\mathbf{x}, t; \omega) - \bar{u}(\mathbf{x}) = \sum_i \alpha_i(t; \omega)\Phi_i(\mathbf{x}). \tag{F.1}$$

Here, $\alpha_i(t; \omega)$ denotes the time dependent stochastic coefficients and $\Phi_i(\mathbf{x})$ denote a generalizable basis for the particular flow field. The decomposition thus seeks to obtain a low dimensional *static* basis. The above decomposition performs a separation of variables in stochastic time dependent coefficients and spatial basis. The instantaneous solution is obtained by evolving the coefficients $\alpha_i(t; \omega)$ by performing a Galerkin projection of the original governing equations to the orthonormal spatial basis $u_i(\mathbf{x})$.

F.1.2 Algorithm

The POD algorithm consists of finding out the two components of the decomposition: the static basis $\Phi_i(\mathbf{x})$ and the time dependent coefficients $\alpha_i(t;\omega)$.

F.1.2.1 Compute The Spatial Basis

To compute the spatial basis $\Phi_i(\mathbf{x})$ we take a collection of n snapshots (method of snapshots[94, 21, 22, 23]) of the deterministic DNS solution at different time instants $t = t_1, t_2, ..., t_n$. Thus we obtain a data matrix A of size $N \times n$ where N is the number of grid points at which the solution is evaluated and n is the number of time instants at which the solution is collected such that $n << N$. We compute the eigenvectors of $A^T A$ given by Ψ:

$$A^T A \Psi_j = \lambda_j \Psi_j.$$

The spatial basis are then computed as:

$$\Phi_j = A\Psi_j \frac{1}{\sqrt{\lambda_j}}, \qquad j = 1, 2, ..., r.$$

Here, r is the number of spatial modes considered. The spatial modes obtained using this technique are energetically ranked and rule of thumb is to choose the reduction order such that at least 95% energy of the total energy of the system is captured by r modes.

F.1.2.2 Compute The Time-dependent Coefficients

The obtained spatial modes are orthonormal to each other and thus, using this orthonormality condition we can perform a Galerkin projection on the partial differential equation defining the evolution of the system and obtain the evolution equation for the time-dependent coefficients.

F.1.3 Advantages of the Method

1. Using the method of snapshots described above we can convert a partial differential equation of a large grid size into a reduced order model evaluating only the time dependent coefficients.
2. The POD technique is a widely used technique for data compression, flow reconstruction, design optimization, pattern recognition.
3. The POD modes are computed with L_2 optimality. The POD modes is optimal in terms of minimizing the mean-square error between the signal and the its truncated representation.

F.1.4 Drawbacks

1. The construction of the spatial modes require large memory for storing the data matrix A. This memory requirement is especially significant for larger grid sizes.
2. The POD basis obtained from a particular set of operating conditions e.g., Mach number (Ma), Reynolds number (Re) may or may not be useful when the operating conditions are changed. POD basis are also ineffective in extrapolating solutions of localized flows.
3. The POD modes are arranged in order of significance in terms of energy and not in terms of dynamical importance. The lower energy modes which are ignored in the reduced order model can have significant effects on the solution at later time steps which will lead to loss of accuracy of the solution.
4. The dependence of the solution on the random parameters may significantly vary over time. As POD uses static basis, higher number of modes are required in long time integration to maintain the same level of accuracy which leads to larger computational expense.

F.2 The Need for Time-dependent Basis

The POD technique mentioned in the previous section derives static manifold based on the visualized data from the time snapshots. A major disadvantage of this technique is the inability of the method to predict transient behaviour. A pictorial representation is shown in Fig.(60) which shows a 2D approximation of a 3D Rössler attractor. In the subfigure on the left, the attractor is approximated by 2D static basis derived from POD. We observe that the 2D plane approximates the behavior correctly in the $x - y$ plane. Even though the plane is slightly titled to take into the data points from the transient part, the system will face difficulty in approximating the out-of-plane transient behaviour. The figure on the right shows the same Rössler attractor approximated by time dependent basis. The out-of-plane transient behaviour is captured accurately due to the evolution of the basis as the system evolves.

F.3 Dynamically Orthogonal (DO) Method

The dynamically orthogonal technique is a time-dependent basis technique developed by Sapsis [1, 79] in context of stochastic partial differential equations. The method performs separation of variables similar to the POD technique but not in time.

F.3.1 DO Decomposition

We consider a random field given by $u(\mathbf{x}, t; \omega)$ which can be expressed in DO decomposition as,

$$u(\mathbf{x}, t; \omega) - \bar{u}(\mathbf{x}, t) = \sum_i Y_i(t; \omega) u_i(\mathbf{x}, t), \tag{F.2}$$

where $Y_i(t; \omega)$ are stochastic processes, $u_i(\mathbf{x}, t)$ are the orthonormal spatial basis and the $\bar{u}(\mathbf{x}, t)$ is the expected value of all random samples. In this decomposition, both the $Y_i(t; \omega)$ and $u_i(\mathbf{x}, t)$ evolve in time. The basis thus, adapt to the stochasticity of the flow.

F.3.2 Algorithm

The DO algorithm consists of the initializing the basis at $t = 0$ and evolving the stochastic and spatial basis according to the evolution equations. The evolution equations of DO decomposition are first order optimality conditions of its variational principle. The reader is referred to Table.(1) and [1] for the evolution equations of DO modes.
The evolution of the spatial basis is restricted by the 'dynamically orthogonality'condition given by,

$$\left\langle \frac{\partial u_i(\mathbf{x},t)}{\partial t}, u_j(\mathbf{x},t) \right\rangle = 0.$$

The DO decomposition provides a set of explicit equations for the evolution of the stochastic and spatial modes. The original SPDE is transformed to a r-dimensional stochastic differential equation for $Y_i(t;\omega)$ and $r+1$ deterministic PDEs for $\bar{u}(\mathbf{x},t)$ and $u_i(\mathbf{x},t)$.

F.3.3 Advantages of the Method

1. The original SPDE is transformed into a system of equations for the evolution of the DO modes which evolve according to the evolution of the flow field. This decomposition is effective is capturing in strongly transient and non-stationary response.
2. From the DO representation the first and second order moments i.e., mean and variance are obtained readily.

F.3.4 Drawbacks

1. The inversion of the covariance matrix in the evolution equations leads to inaccuracy in the solution for large condition number (ratio of largest to smallest eigenvalue) of the covariance matrix.

F.4 Bi-Orthogonal (BO) Method

The bi-orthogonal technique [2, 32] is another time-dependent basis technique developed by Cheng et. al. The BO decomposition is similar in form to the DO decomposition however

differs in terms of the conditions imposed on the spatial and stochastic modes. Imposition of these different conditions affects the numerical properties of this method.

F.4.1 BO Decomposition

We consider a random field given by $u(\mathbf{x}, t; \omega)$ which can be expressed in BO decomposition as,

$$u(\mathbf{x}, t; \omega) - \bar{u}(\mathbf{x}, t) = \sum_i Y_i(t; \omega) u_i(\mathbf{x}, t) \tag{F.3}$$

where $Y_i(t; \omega)$ are stochastic processes, $u_i(\mathbf{x}, t)$ are the spatial basis and $\bar{u}(\mathbf{x}, t)$ is the expected value of all random samples.

F.4.2 Algorithm

The BO algorithm consists of the initializing the basis at $t = 0$ and evolving the stochastic and spatial basis according to the evolution equations. The evolution equations of BO decomposition are first order optimality conditions of its variational principle. In case of the BO method, orthonormality of the stochastic modes and orthogonality of the spatial modes is imposed. The constraints imposed on BO modes are *static*. The reader is referred to Table.(1) and [2, 32] for the evolution equations of BO modes.

F.4.3 Advantages of the Method

1. The BO method is more stable than the DO method for higher modes in non-linear problems.
2. A low dimensional structure is computed on-the-fly at every time instant.

F.4.4 Drawbacks

1. Due to constraints imposed on the method and the corresponding evolution equations obtained, the method diverges when two eigenvalues are very close to each other or when two eigenvalues cross each other.

2. If the system is strongly transient and nonlinear a low reduction order might not be effective in capturing the solution accurately. An increasing number of modes are needed as time evolves to keep the error to a minimum.

F.5 Dynamically Bi-Orthonormal (DBO) Method

The dynamically bi-orthonormal technique was developed [46] to overcome some of the limitations associated with the DO and BO method. The method adds an additional factor of covariance matrix to the decomposition which helps in improving the numerical properties of the time dependent basis technique.

F.5.1 DBO Decomposition

We consider a random field given by $u(\mathbf{x}, t; \omega)$ which can be expressed in DBO decomposition as,

$$u(\mathbf{x}, t; \omega) - \bar{u}(\mathbf{x}, t) = \sum_j \sum_i u_i(\mathbf{x}, t)\Sigma_{ij}(t)Y_j(t; \omega) \tag{F.4}$$

where $Y_i(t; \omega)$ are stochastic processes, $u_i(\mathbf{x}, t)$ are the spatial basis, $\Sigma_{ij}(t)$ is the factor of the covariance matrix and $\bar{u}(\mathbf{x}, t)$ is the expected value of all random samples.

F.5.2 Algorithm

The DBO algorithm consists of the initializing the basis at $t = 0$ and evolving the stochastic basis, spatial basis and $\Sigma(t)$ according to the evolution equations. The evolution equations of DBO decomposition are first order optimality conditions of its variational principle. In this method the dynamically orthogonality condition and orthonormality condition is imposed on both the stochastic and spatial modes. The reader is referred to Table.(1) and [46] for the evolution equations of DBO modes.

A pictorial representation of the conditions imposed on the stochastic modes and spatial modes are shown in Fig.(61). The figure on the left shows the spatial modes $u_i(\mathbf{x}, t)$. We can see that all three methods impose the orthogonality conditions on the spatial modes.

However, the DO and DBO methods impose orthonormality condition which means that the inner product of the modes can be written as,

$$\langle u_i(\mathbf{x}, t), u_j(\mathbf{x}, t)\rangle = \delta_{ij}.$$

The BO modes on the other hand are scaled according to the eigenvalues associated with the modes. Similarly, the stochastic modes are represented on the subfigure on the right. In this case, the BO and DBO methods impose the orthonormality condition such that,

$$\mathbb{E}[y_i(t;\omega)y_j(t;\omega)] = \delta_{ij}.$$

The DO modes on the other hand impose neither the orthonormality condition nor the orthogonality condition thus, the modes can be highly correlated.

F.5.3 Advantages of the Method

1. Due to the low condition number of the inversion of the factor of covariance matrix, the method preserves accuracy in large scales of separation between singular values where the DO and BO would be inaccurate.

F.5.4 Drawbacks

1. The three time dependent basis methods discussed before are ineffective in flow regime where the growth of eigenvalues is swift and small perturbations lead to propagation of uncertainty in large number of independent directions. To preserve accuracy in such cases, the reduction order i.e., the number of modes needs to be increased. However, this can lead to an increase in the computational expense.
2. In case of turbulent flows, lower energy modes which are discarded at an initial time can have significant impact on the flow dynamics at a later stage. Closure models are needed to take into account the effect of these unresolved modes.

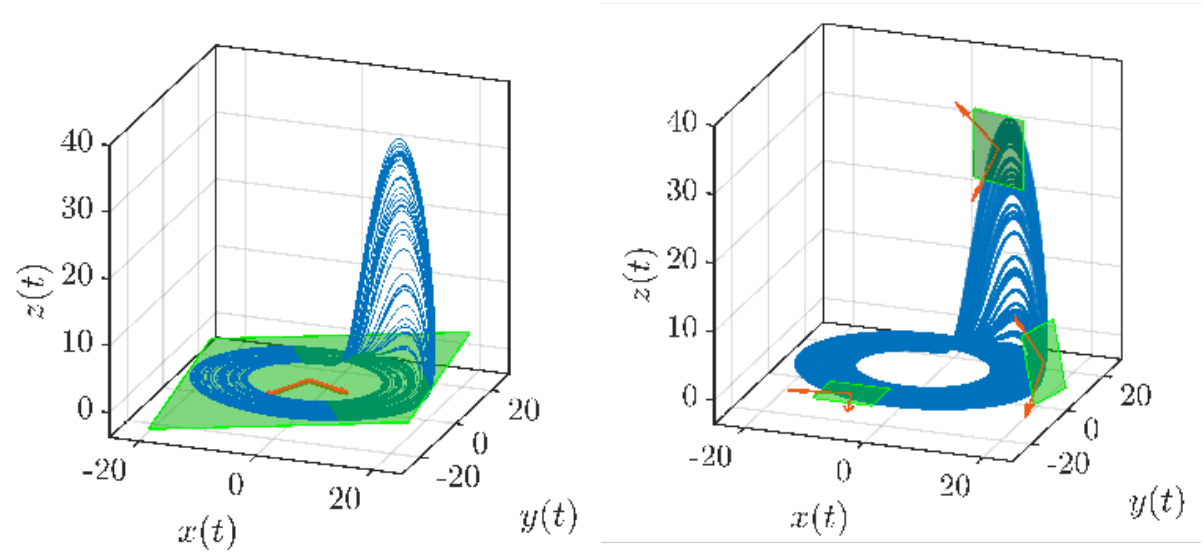

(a) Static basis

(b) Time dependent basis

Figure 60: The above figure shows the 3D Rössler attractor approximated by a 2D basis. In the figure on the left the attractor is approximated by a 2D static basis derived from POD. The figure on the right approximates the attractor using the time-dependent basis. The basis adapt according to the trajectory of the system at every time instant.

Image courtesy: Michael Donello, Hessam Babaee: "Real-Time Reduced Order Modeling Using Time Dependent Subspaces", 72nd Annual Meeting of the APS Division of Fluid Dynamics, Volume 64, Number 13

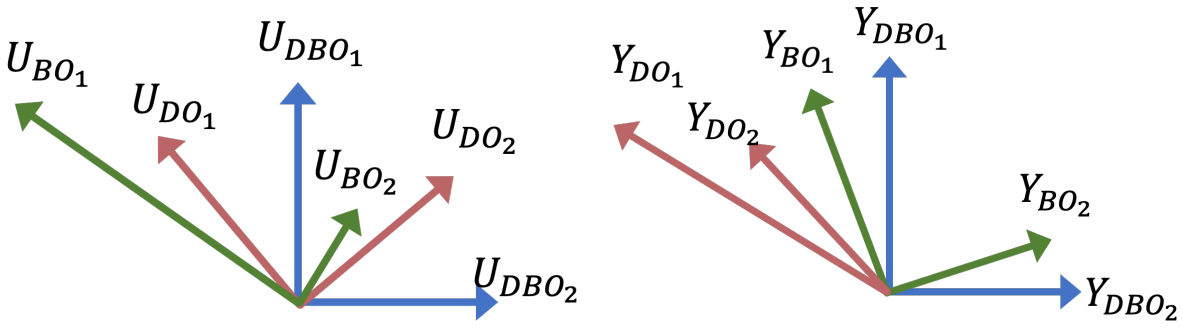

(a) Spatial basis

(b) Stochastic basis

Figure 61: The above figure shows a comparison between the spatial and stochastic modes associated with the DO, BO and the DBO method. The scaling and the orthonormality/orthogonality conditions imposed on these modes are pictorially represented in the figure. DO modes are shown in *red*, BO modes are shown in *green* and DBO modes are depicted in *blue*.

Bibliography

[1] T. P. Sapsis and P. F. Lermusiaux, "Dynamically orthogonal field equations for continuous stochastic dynamical systems," *Physica D: Nonlinear Phenomena*, vol. 238, no. 23-24, pp. 2347–2360, 2009.

[2] M. Cheng, T. Y. Hou, and Z. Zhang, "A dynamically bi-orthogonal method for time-dependent stochastic partial differential equations I: Derivation and algorithms," *Journal of Computational Physics*, vol. 242, pp. 843–868, 2013.

[3] M. Choi, T. P. Sapsis, and G. E. Karniadakis, "On the equivalence of dynamically orthogonal and bi-orthogonal methods: Theory and numerical simulations," *Journal of Computational Physics*, vol. 270, pp. 1–20, 2014.

[4] "A multifaceted mathematical approach for complex systems," *Report of the DOE Workshop on Mathematics for the Analysis, Simulation, and Optimization of Complex Systems*, 2011.

[5] M. B. Giles, "Multilevel Monte Carlo path simulation," *Operations Research*, vol. 56, no. 3, pp. 607–617, 2008.

[6] A. Barth, C. Schwab, and N. Zollinger, "Multi-level Monte Carlo Finite Element method for elliptic PDEs with stochastic coefficients," *Numerische Mathematik*, vol. 119, no. 1, pp. 123–161, 2011.

[7] F. Y. Kuo, C. Schwab, and I. H. Sloan, "Quasi-Monte Carlo finite element methods for a class of elliptic partial differential equations with random coefficients," *SIAM Journal on Numerical Analysis*, vol. 50, no. 6, pp. 3351–3374, 2012.

[8] R. G. Ghanem and P. D. Spanos, *Stochastic finite elements: A spectral approach*. Courier Corporation, 2003.

[9] X. Wan and G. E. Karniadakis, "Multi-element generalized polynomial chaos for arbitrary probability measures," *SIAM Journal on Scientific Computing*, vol. 28, no. 3, pp. 901–928, 2006.

[10] D. Xiu and J. S. Hesthaven, "High-order collocation methods for differential equations with random inputs," *SIAM Journal on Scientific Computing*, vol. 27, no. 3, pp. 1118–1139, 2005.

[11] D. Xiu and G. E. Karniadakis, "The Wiener-Askey polynomial chaos for stochastic differential equations," *SIAM Journal on Scientific Computing*, vol. 24, no. 2, pp. 619–644, 2002.

[12] J. Foo and G. E. Karniadakis, "Multi-element probabilistic collocation method in high dimensions," *Journal of Computational Physics*, vol. 229, no. 5, pp. 1536–1557, 2010.

[13] J. Foo, X. Wan, and G. E. Karniadakis, "The multi-element probabilistic collocation method (ME-PCM): Error analysis and applications," *Journal of Computational Physics*, vol. 227, no. 22, pp. 9572–9595, 2008.

[14] I. Babuška, F. Nobile, and R. Tempone, "A stochastic collocation method for elliptic partial differential equations with random input data," *SIAM Journal on Numerical Analysis*, vol. 45, no. 3, pp. 1005–1034, 2007.

[15] B. Ganapathysubramanian and N. Zabaras, "Sparse grid collocation schemes for stochastic natural convection problems," *Journal of Computational Physics*, vol. 225, no. 1, pp. 652–685, 2007.

[16] X. Yang, M. Choi, G. Lin, and G. E. Karniadakis, "Adaptive ANOVA decomposition of stochastic incompressible and compressible flows," *Journal of Computational Physics*, vol. 231, no. 4, pp. 1587–1614, 2012.

[17] H. Babaee, X. Wan, and S. Acharya, "Effect of uncertainty in blowing ratio on film cooling effectiveness," *Journal of Heat Transfer*, vol. 136, no. 3, 2014.

[18] D. Zhang, H. Babaee, and G. E. Karniadakis, "Stochastic domain decomposition via moment minimization," *SIAM Journal on Scientific Computing*, vol. 40, no. 4, pp. A2152–A2173, 2018.

[19] X. Wan and G. E. Karniadakis, "Long-term behavior of polynomial chaos in stochastic flow simulations," *Computer Methods in Applied Mechanics and Engineering*, vol. 195, no. 41-43, pp. 5582–5596, 2006.

[20] M. Branicki and A. J. Majda, "Fundamental limitations of polynomial chaos for uncertainty quantification in systems with intermittent instabilities," *Communications in Mathematical Sciences*, vol. 11, no. 1, pp. 55–103, 2013.

[21] L. Sirovich, "Turbulence and the dynamics of coherent structures. I. coherent structures," *Quarterly of applied mathematics*, vol. 45, no. 3, pp. 561–571, 1987.

[22] L. Sirovich, "Turbulence and the dynamics of coherent structures. ii. symmetries and transformations," *Quarterly of Applied mathematics*, vol. 45, no. 3, pp. 573–582, 1987.

[23] L. Sirovich, "Turbulence and the dynamics of coherent structures. iii. dynamics and scaling," *Quarterly of Applied mathematics*, vol. 45, no. 3, pp. 583–590, 1987.

[24] P. J. Schmid, "Dynamic mode decomposition of numerical and experimental data," *Journal of fluid mechanics*, vol. 656, pp. 5–28, 2010.

[25] L. Alvergue, H. Babaee, G. Gu, and S. Acharya, "Feedback stabilization of a reduced-order model of a jet in crossflow," *AIAA Journal*, vol. 53, pp. 2472–2481, 2016/02/17 2015.

[26] C. Rowley, I. Mezić, S. Bagheri, P. Schlatter, and D. Henningson, "Reduced-order models for flow control: balanced models and koopman modes," in *Seventh IUTAM Symposium on Laminar-Turbulent Transition*, pp. 43–50, Springer, 2010.

[27] J. N. Kutz, S. L. Brunton, B. W. Brunton, and J. L. Proctor, *Dynamic mode decomposition: data-driven modeling of complex systems*. SIAM, 2016.

[28] B. R. Noack, "From snapshots to modal expansions –bridging low residuals and pure frequencies," vol. 802, pp. 1–4, 2016.

[29] B. Peherstorfer, K. Willcox, and M. Gunzburger, "Survey of multifidelity methods in uncertainty propagation, inference, and optimization," *SIAM Review*, vol. 60, pp. 550–591, 2019/04/26 2018.

[30] P. Perdikaris, D. Venturi, J. O. Royset, and G. E. Karniadakis, "Multi-fidelity modelling via recursive co-kriging and gaussian–markov random fields," 2015.

[31] H. Babaee, P. Perdikaris, C. Chryssostomidis, and G. E. Karniadakis, "Multi-fidelity modelling of mixed convection based on experimental correlations and numerical simulations," *Journal of Fluid Mechanics*, vol. 809, pp. 895–917, 12 2016.

[32] M. Cheng, T. Y. Hou, and Z. Zhang, "A dynamically bi-orthogonal method for time-dependent stochastic partial differential equations II: Adaptivity and generalizations," *Journal of Computational Physics*, vol. 242, pp. 753–776, 2013.

[33] H. Babaee, "An observation-driven time-dependent basis for a reduced description of transient stochastic systems," *Proceedings of the Royal Society A*, vol. 475, no. 2231, p. 20190506, 2019.

[34] E. Musharbash, F. Nobile, and T. Zhou, "Error analysis of the dynamically orthogonal approximation of time dependent random pdes," *SIAM Journal on Scientific Computing*, vol. 37, pp. A776–A810, 2018/01/17 2015.

[35] M. H. Beck, A. Jäckle, G. A. Worth, and H.-D. Meyer, "The multiconfiguration time-dependent Hartree (MCTDH) method: a highly efficient algorithm for propagating wavepackets," *Physics reports*, vol. 324, no. 1, pp. 1–105, 2000.

[36] C. Bardos, F. Golse, A. D. Gottlieb, and N. J. Mauser, "Mean field dynamics of fermions and the time-dependent Hartree–Fock equation," *Journal de mathématiques pures et appliquées*, vol. 82, no. 6, pp. 665–683, 2003.

[37] O. Koch and C. Lubich, "Dynamical low-rank approximation," *SIAM Journal on Matrix Analysis and Applications*, vol. 29, no. 2, pp. 434–454, 2007.

[38] H. Babaee, M. Farazmand, G. Haller, and T. P. Sapsis, "Reduced-order description of transient instabilities and computation of finite-time lyapunov exponents," *Chaos: An Interdisciplinary Journal of Nonlinear Science*, vol. 27, no. 6, p. 063103, 2017.

[39] H. Babaee and T. Sapsis, "A minimization principle for the description of modes associated with finite-time instabilities," *Proceedings of the Royal Society A: Mathematical, Physical and Engineering Sciences*, vol. 472, no. 2186, p. 20150779, 2016.

[40] H. Babaee, M. Choi, T. P. Sapsis, and G. E. Karniadakis, "A robust bi-orthogonal/dynamically-orthogonal method using the covariance pseudo-inverse with application to stochastic flow problems," *Journal of Computational Physics*, vol. 344, pp. 303–319, 2017.

[41] Z. Battles and L. N. Trefethen, "An extension of MATLAB to continuous functions and operators," *SIAM Journal on Scientific Computing*, vol. 25, no. 5, pp. 1743–1770, 2004.

[42] E. Musharbash and F. Nobile, "Dual dynamically orthogonal approximation of incompressible navier stokes equations with random boundary conditions," *Journal of Computational Physics*, vol. 354, pp. 135–162, 2018.

[43] H. Babaee, "A scalable observation-driven time-dependent basis for a reduced description of transient systems," 2019.

[44] M. Choi, T. P. Sapsis, and G. E. Karniadakis, "A convergence study for spdes using combined polynomial chaos and dynamically-orthogonal schemes," *Journal of Computational Physics*, vol. 245, pp. 281–301, 2013.

[45] E. Musharbash and F. Nobile, "Dual dynamically orthogonal approximation of incompressible Navier Stokes equations with random boundary conditions," *Journal of Computational Physics*, vol. 354, pp. 135–162, 2018.

[46] P. Patil and H. Babaee, "Real-time reduced-order modeling of stochastic partial differential equations via time-dependent subspaces," *Journal of Computational Physics*, p. 109511, 2020.

[47] D. Ramezanian, A. G. Nouri, and H. Babaee, "On-the-fly reduced order modeling of passive and reactive species via time-dependent manifolds," *Computer Methods in Applied Mechanics and Engineering*, vol. 382, p. 113882, 2021.

[48] X. Wan and G. E. Karniadakis, "An adaptive multi-element generalized polynomial chaos method for stochastic differential equations," *Journal of Computational Physics*, vol. 209, no. 2, pp. 617–642, 2005.

[49] G. Berkooz, P. Holmes, and J. L. Lumley, "The proper orthogonal decomposition in the analysis of turbulent flows," *Annual review of fluid mechanics*, vol. 25, no. 1, pp. 539–575, 1993.

[50] P. Holmes, J. L. Lumley, G. Berkooz, and C. W. Rowley, *Turbulence, coherent structures, dynamical systems and symmetry*. Cambridge university press, 2012.

[51] A. Liakopoulos, P. Blythe, and H. Gunes, "A reduced dynamical model of convective flows in tall laterally heated cavities," *Proceedings of the Royal Society of Lon-*

don. Series A: Mathematical, Physical and Engineering Sciences, vol. 453, no. 1958, pp. 663–672, 1997.

[52] D. Rempfer, "On low-dimensional galerkin models for fluid flow," *Theoretical and Computational Fluid Dynamics*, vol. 14, no. 2, pp. 75–88, 2000.

[53] S. Y. Shvartsman and I. Kevrekidis, "Low-dimensional approximation and control of periodic solutions in spatially extended systems," *Physical Review E*, vol. 58, no. 1, p. 361, 1998.

[54] A. Deane, I. Kevrekidis, G. E. Karniadakis, and S. Orszag, "Low-dimensional models for complex geometry flows: application to grooved channels and circular cylinders," *Physics of Fluids A: Fluid Dynamics*, vol. 3, no. 10, pp. 2337–2354, 1991.

[55] P. Benner, S. Gugercin, and K. Willcox, "A survey of projection-based model reduction methods for parametric dynamical systems," *SIAM review*, vol. 57, no. 4, pp. 483–531, 2015.

[56] K. Carlberg, M. Barone, and H. Antil, "Galerkin v. least-squares petrov–galerkin projection in nonlinear model reduction," *Journal of Computational Physics*, vol. 330, pp. 693–734, 2017.

[57] K. Carlberg, C. Farhat, J. Cortial, and D. Amsallem, "The gnat method for nonlinear model reduction: effective implementation and application to computational fluid dynamics and turbulent flows," *Journal of Computational Physics*, vol. 242, pp. 623–647, 2013.

[58] S. Chaturantabut and D. C. Sorensen, "Nonlinear model reduction via discrete empirical interpolation," *SIAM Journal on Scientific Computing*, vol. 32, no. 5, pp. 2737–2764, 2010.

[59] C. W. Rowley, I. Mezić, S. Bagheri, P. Schlatter, and D. S. Henningson, "Spectral analysis of nonlinear flows," *Journal of fluid mechanics*, vol. 641, pp. 115–127, 2009.

[60] I. Mezić, "Analysis of fluid flows via spectral properties of the koopman operator," *Annual Review of Fluid Mechanics*, vol. 45, pp. 357–378, 2013.

[61] S. Bagheri, "Koopman-mode decomposition of the cylinder wake," *Journal of Fluid Mechanics*, vol. 726, pp. 596–623, 2013.

[62] M. Budišić, R. Mohr, and I. Mezić, "Applied koopmanism," *Chaos: An Interdisciplinary Journal of Nonlinear Science*, vol. 22, no. 4, p. 047510, 2012.

[63] M. Raissi, P. Perdikaris, and G. E. Karniadakis, "Physics-informed neural networks: A deep learning framework for solving forward and inverse problems involving nonlinear partial differential equations," *Journal of Computational physics*, vol. 378, pp. 686–707, 2019.

[64] M. Raissi, A. Yazdani, and G. E. Karniadakis, "Hidden fluid mechanics: Learning velocity and pressure fields from flow visualizations," *Science*, vol. 367, no. 6481, pp. 1026–1030, 2020.

[65] G. E. Karniadakis, I. G. Kevrekidis, L. Lu, P. Perdikaris, S. Wang, and L. Yang, "Physics-informed machine learning," *Nature Reviews Physics*, vol. 3, no. 6, pp. 422–440, 2021.

[66] L. Lu, P. Jin, G. Pang, Z. Zhang, and G. E. Karniadakis, "Learning nonlinear operators via deeponet based on the universal approximation theorem of operators," *Nature Machine Intelligence*, vol. 3, no. 3, pp. 218–229, 2021.

[67] L. Lu, P. Jin, and G. E. Karniadakis, "Deeponet: Learning nonlinear operators for identifying differential equations based on the universal approximation theorem of operators," *arXiv preprint arXiv:1910.03193*, 2019.

[68] J. Sirignano and K. Spiliopoulos, "Dgm: A deep learning algorithm for solving partial differential equations," *Journal of computational physics*, vol. 375, pp. 1339–1364, 2018.

[69] M. Milano and P. Koumoutsakos, "Neural network modeling for near wall turbulent flow," *Journal of Computational Physics*, vol. 182, no. 1, pp. 1–26, 2002.

[70] K. Lee and K. T. Carlberg, "Model reduction of dynamical systems on nonlinear manifolds using deep convolutional autoencoders," *Journal of Computational Physics*, vol. 404, p. 108973, 2020.

[71] R. Fu, D. Xiao, I. Navon, and C. Wang, "A data driven reduced order model of fluid flow by auto-encoder and self-attention deep learning methods," *arXiv preprint arXiv:2109.02126*, 2021.

[72] T. R. Phillips, C. E. Heaney, P. N. Smith, and C. C. Pain, "An autoencoder-based reduced-order model for eigenvalue problems with application to neutron diffusion," *International Journal for Numerical Methods in Engineering*, vol. 122, no. 15, pp. 3780–3811, 2021.

[73] S. E. Otto and C. W. Rowley, "Linearly recurrent autoencoder networks for learning dynamics," *SIAM Journal on Applied Dynamical Systems*, vol. 18, no. 1, pp. 558–593, 2019.

[74] P. Baldi and K. Hornik, "Neural networks and principal component analysis: Learning from examples without local minima," *Neural networks*, vol. 2, no. 1, pp. 53–58, 1989.

[75] N. Watters, D. Zoran, T. Weber, P. Battaglia, R. Pascanu, and A. Tacchetti, "Visual interaction networks: Learning a physics simulator from video," *Advances in neural information processing systems*, vol. 30, 2017.

[76] C. Lu, B. Jayaraman, J. Whitman, and G. Chowdhary, "Sparse convolution-based markov models for nonlinear fluid flows," *arXiv preprint arXiv:1803.08222*, 2018.

[77] S. C. Puligilla and B. Jayaraman, "Deep multilayer convolution frameworks for data-driven learning of fluid flow dynamics," in *2018 Fluid Dynamics Conference*, p. 3091, 2018.

[78] S. Wiewel, M. Becher, and N. Thuerey, "Latent space physics: Towards learning the temporal evolution of fluid flow," in *Computer graphics forum*, vol. 38, pp. 71–82, Wiley Online Library, 2019.

[79] T. P. Sapsis, *Dynamically orthogonal field equations for stochastic fluid flows and particle dynamics*. PhD thesis, Massachusetts Institute of Technology, 2011.

[80] O. Koch and C. Lubich, "Dynamical tensor approximation," *SIAM Journal on Matrix Analysis and Applications*, vol. 31, no. 5, pp. 2360–2375, 2010.

[81] P. Patil and H. Babaee, "Reduced order modeling with time-dependent bases for pdes with stochastic boundary conditions," *arXiv preprint arXiv:2112.14326*, 2021.

[82] H. Babaee, M. Farazmand, T. Sapsis, and G. Haller, "Computing finite-time lyapunov exponents with optimally time dependent reduction," in *APS Division of Fluid Dynamics Meeting Abstracts*, pp. L8–003, 2016.

[83] A. Blanchard, S. Mowlavi, and T. P. Sapsis, "Control of linear instabilities by dynamically consistent order reduction on optimally time-dependent modes," *Nonlinear Dynamics*, vol. 95, no. 4, pp. 2745–2764, 2019.

[84] T. P. Sapsis, "New perspectives for the prediction and statistical quantification of extreme events in high-dimensional dynamical systems," *Philosophical Transactions of the Royal Society A: Mathematical, Physical and Engineering Sciences*, vol. 376, no. 2127, p. 20170133, 2018.

[85] M. Donello, M. Carpenter, and H. Babaee, "Computing sensitivities in evolutionary systems: A real-time reduced order modeling strategy," *arXiv preprint arXiv:2012.14028*, 2020.

[86] A. Nouri, H. Babaee, P. Givi, H. Chelliah, and D. Livescu, "Skeletal model reduction with forced optimally time dependent modes," *arXiv preprint arXiv:2103.09101*, 2021.

[87] S. Z. Ashtiani, M. R. Malik, and H. Babaee, "Scalable in situ compression of transient simulation data using time-dependent bases," *arXiv preprint arXiv:2201.06958*, 2022.

[88] Y. Du and T. A. Zaki, "Evolutional deep neural network," *Physical Review E*, vol. 104, no. 4, p. 045303, 2021.

[89] J. Bruna, B. Peherstorfer, and E. Vanden-Eijnden, "Neural galerkin scheme with active learning for high-dimensional evolution equations," *arXiv preprint arXiv:2203.01360*, 2022.

[90] W. Anderson and M. Farazmand, "Evolution of nonlinear reduced-order solutions for pdes with conserved quantities," *SIAM Journal on Scientific Computing*, vol. 44, no. 1, pp. A176–A197, 2022.

[91] Z. Wang, I. Akhtar, J. Borggaard, and T. Iliescu, "Proper orthogonal decomposition closure models for turbulent flows: a numerical comparison," *Computer Methods in Applied Mechanics and Engineering*, vol. 237, pp. 10–26, 2012.

[92] S. Sirisup and G. E. Karniadakis, "A spectral viscosity method for correcting the long-term behavior of pod models," *Journal of Computational Physics*, vol. 194, no. 1, pp. 92–116, 2004.

[93] O. San and T. Iliescu, "Proper orthogonal decomposition closure models for fluid flows: Burgers equation," *arXiv preprint arXiv:1308.3276*, 2013.

[94] L. Sirovich, "Turbulence and the dynamics of coherent structures. part i: Coherent structures," *Quarterly of applied mathematics*, vol. 45, no. 3, pp. 561–571, 1987.